

Novel dopants for n-type doping of electron transport materials: cationic dyes and their bases

Dissertation

zur Erlangung des akademischen Grades

Doctor rerum naturalium
(Dr. rer. nat.)

vorgelegt

der Fakultät Mathematik und Naturwissenschaften
der Technischen Universität Dresden

von

Dipl.-Chem. Fenghong Li

geboren am 10.9.1969 in Changchun, P.R. China

January 2005

Gutachter: Prof. Dr. Karl Leo

Gutachter: Prof. Dr. Josef Salbeck

Gutachter: Prof. Dr. Horst Hartmann

Eingereicht am: 02.02.05

Tag der Verteidigung: 28.04.05

Publications

Articles

1. Leuco crystal violet as a dopant for n-doping of organic thin films of fullerene C₆₀
F. Li, A. Werner, M. Pfeiffer, K. Leo, X. Liu.
J. Phys. Chem. B **108**, 17076 (2004).
2. N-type doping of organic thin films using cationic dyes
A. Werner, F. Li, K. Harada, M. Pfeiffer, T. Fritz, K. Leo, S. Machill.
Adv. Func. Mater. **14**, 255 (2004).
3. Organic p-i-n solar cells
B. Maennig, J. Drechsel, D. Gebeyehu, P. Simon, F. Kozlowski, A. Werner, F. Li, S. Grundmann, S. Sonntag, M. Koch, K. Leo, M. Pfeiffer, H. Hoppe, D. Meissner, N. S. Sariciftci, I. Riedel, V. Dyakonov, J. Parisi.
Appl. Phys. A **79**, 1 (2004).
4. Pyronin B as a donor for n-type doping of organic thin films
A. Werner, F. Li, K. Harada, M. Pfeiffer, T. Fritz, K. Leo.
Appl. Phys. Lett. **82**, 4495 (2003).

Conference reports

1. N-type doping of organic electron transport materials for solar cells
F. Li, A. Werner, K. Harada, B. Maennig, J. Drechsel, K. Leo, M. Pfeiffer.
Proceedings of the International Society for Optical Engineering (SPIE), Bellingham, **5464**, 364 (2004).
2. Leuco bases as dopants for n-type doping of organic thin films
F. Li, A. Werner, M. Pfeiffer, K. Leo.
Frühjahrstagung der Deutschen Physikalischen Gesellschaft, Regensburg, 2004.
In: Verhandl. DPG (IV) 39 (2004), 546.
3. Pyronin B as a donor for n-type doping of organic thin films
F. Li, A. Werner, K. Harada, B. Maennig, J. Drechsel, K. Leo, M. Pfeiffer.

7th European conference on molecular electronics. Avignon, 2003. In: Book of Abstracts, 192.

4. Pyronin B as a donor for n-type doping of organic thin films
F. Li, A. Werner, K. Harada, B. Maennig, J. Drechsel, K. Leo, M. Pfeiffer.
Frühjahrstagung der Deutschen Physikalischen Gesellschaft, Dresden, 2003.
In: Verhandl. DPG (IV) 38 (2003), 206.

Patent

1. Dotierte organische Halbleitermaterialien sowie Verfahren zu deren Herstellung
(in English: Doped organic semiconductor materials and methods for their
fabrication)
Ansgar Werner, Fenghong Li, Martin Pfeiffer
DE 10338406.5.

Contents

1	Introduction	1
2	Theoretical background	5
2.1	Electronic properties of organic semiconductors	5
2.2	Generation of charge carriers - the doping process	10
2.3	Charge carrier transfer in organic semiconductors	12
2.3.1	Band transport in organic crystals	13
2.3.2	Hopping transport in disordered organic semiconductors	14
3	Materials and Experiments	23
3.1	Materials	23
3.1.1	Matrices: C ₆₀ , F ₁₆ ZnPc and NTCDA	23
3.1.2	Dopants	28
3.2	Purification of materials	33
3.3	Experimental methods	35
3.3.1	Field effect experiments	35
3.3.2	Thermopower experiments	36
3.3.3	FTIR spectroscopy	37
3.4	Sample preparation and measurements	38
4	Cationic dyes as dopants for n-type doping of organic electron transport materials	41
4.1	Electrical properties of n-type organic thin films using cationic dyes as dopants	41
4.2	Mass spectroscopy	45
4.3	Optical spectroscopy	47
4.3.1	Pure evaporated CV in solid thin film	47
4.3.2	Mixed films of TCNQ and CV	49
4.3.3	Mixed films of NTCDA and pyronin B	51
4.4	Conclusions	53
5	Leuco crystal violet as a dopant for n-type doping of organic thin films of fullerene C₆₀	55
5.1	Electrical properties of C ₆₀ doped with LCV	55

5.2	Optical spectroscopy	57
5.2.1	Pure LCV in solid thin film	57
5.2.2	Mixed films of TCNQ:LCV	59
5.2.3	Mixed films of C ₆₀ :LCV	61
5.3	Electrochemistry of LCV and CV	66
5.4	Mechanism of photoinduced electron transfer from LCV to C ₆₀	68
5.5	Conclusions	68
6	Acridine orange base as a dopant for n-type doping of organic thin films of fullerene C₆₀	71
6.1	Electrical properties of thin films of C ₆₀ doped with acridine orange base	71
6.1.1	Conductivity	71
6.1.2	Field effect study of C ₆₀ thin films doped with AOB	76
6.1.3	Thermopower study of C ₆₀ thin films doped with AOB [170]	81
6.2	Mass spectroscopy	85
6.3	Optical spectroscopy of mixed films of C ₆₀ :AOB	86
6.3.1	NIR absorption spectrum of C ₆₀ :AOB	86
6.3.2	FTIR spectroscopy of mixed thin film of C ₆₀ :AOB	87
6.4	Electrochemistry of AO and AOB	88
6.5	Conclusions	91
7	Summary and outlook	93
7.1	Summary	93
7.2	Outlook	94
	References	97
	List of symbols and abbreviations	105
	Acknowledgements	107

Chapter 1

Introduction

The development of organic materials and devices with application in light emission, light energy conversion and thin film electronics has received considerable attention over the past years [1, 2, 3]. The most advanced organic electronic systems already in commercial production are highly efficient, very bright and colorful thin displays based on organic light-emitting devices [4] (OLEDs). Significant progress is also being made in the realization of thin-film transistors [5, 6] (TFTs) and thin-film organic photovoltaic cells [7, 8, 9, 10] for low-cost solar energy generation. Common to all these devices are organic semiconductor thin film architectures.

Organic semiconductors have unique physical properties [2], which offer many advantages over inorganic semiconductors: (i) The extremely high absorption coefficients of some dyes in the visible range offer the possibility to prepare very thin photodetectors and photovoltaic cells [11]. (ii) Due to thin layers, the requirements on chemical and structural perfection are reduced since the excitation energy does not have to travel long distances. (iii) Many fluorescent dyes emit strongly red shifted to their absorption. Thus, there are almost no reabsorption losses in OLEDs [12], which, together with the low indices of refraction, circumvents the key problems of inorganic LED. (iv) Since organic semiconductors consist of molecular structures with saturated electron systems, the number of intrinsic defects in disordered systems is much lower than in inorganic amorphous semiconductors, where a large number of dangling bonds exist. (v) There is a nearly unlimited number of chemical compounds available, and it is possible to tailor materials.

The history of silicon technology showed that controlled doping was a key step for the realization of effective, stable and reproducible devices. When the conduction type was no longer determined by impurities but could be controlled by doping, the breakthrough of classical microelectronics became possible. Unlike inorganic semiconductors, organic dyes are up to now usually prepared in a nominally undoped

form. However, controlled and stable doping is desirable in many organic-based devices as well. If we succeed in shifting the Fermi level towards the transport states, this could reduce ohmic losses, ease carrier injection from contacts and increase the built-in potential of Schottky- or pn-junctions.

In previous studies of p-doping [13, 14, 15], it has been shown that electron transfer from the matrix to the dopant molecules leads to an increased number of mobile holes, thus increasing the conductivity. The Fermi level shifts towards the transport states with increasing dopant concentration, as shown by Seebeck measurements. Finally, doping leads to very thin (<5 nm) space charge layers at contacts associated with efficient injection. Consequently, hole transport layers doped with strong organic acceptor molecules, and alkali metal doped electron transport layers incorporated in an optimized OLED drastically improve the performance in terms of operation voltage and efficiency [16, 17]. More recently, our group has also shown that doped transport layers allow to realize efficient inverted OLEDs needed for OLEDs on opaque substrates [18, 19].

Up till now, n-type doping of electron transport layers in OLEDs has only been carried out using alkali metals like Li or Cs [16, 20, 21]. In contrast to molecular doping, where dopant concentrations of a few percent are sufficient, alkali metal (Li or Cs) levels up to 1:1 (matrix molecule/dopant atom) are needed in order to obtain a strong doping effect. However, such a high doping ratio strongly alters not only the conductivity, but also the matrix properties. Furthermore, the small metal ions can diffuse in the device during growth and operation [21]. This compromises the stability of device. In order to reduce diffusion, organic donors would be preferable as dopants.

Unfortunately, an organic donor which can be used for the typically employed electron transport materials has not been available yet. Having a lowest unoccupied molecular orbital (LUMO) of about 3 eV, these electron transport materials are only weak electron acceptors. This imposes requirements on the position of the highest occupied molecular orbital (HOMO) of the donor, which are difficult to meet. In fact, the strong electron donor bis (ethylenedithio)-tetrathiafulvalene (BEDT-TTF) has been reported [22] to form deep donor states in 1,4,2,8-naphthalene tetracarboxylic dianhydride (NTCDA). The oxidation potential of BEDT-TTF is 0.48 V vs. SCE (Saturated Calomel Electrode) [23], the reduction potential of NTCDA is -0.29 V vs. SCE [24]. However, the reduction potential of tris (8-hydroxy-quinolinato)-aluminium (Alq_3) is even lower, namely -1.8 V vs. SCE [25]. Organic donors with much lower oxidation potential would be needed in order to dope electron transport materials like Alq_3 used in OLEDs. However, such donor compounds are not easily

synthesized and handled due to their high reactivity. Hence, alternative concepts are needed.

Gregg et al. [26] described a spatially and temporally stable n-type doping with a zwitterionic dopant molecule that is a reduced derivative of the host molecule PPEEB, a liquid crystal perylene diimide. A superlinearly increase with increasing dopant concentration has been observed in the conductivity of the doped PPEEB films.

Recently, Werner performed initial work about cationic dyes as dopants for n-doping of organic thin films [27]. We presented a new approach to circumvent the stability problems of strong donor molecules [27, 28, 29, 30]. In this approach, the volatile donor was created in situ from a stable precursor compound. We regard cationic dyes suitable for our investigation because these molecules already consist of an organic cation and an (often inorganic) counter ion. The closed shell cations are attractive for n-type doping because the corresponding neutral radicals have strong donor character. It is our intention to separate the cationic structure from the compound and to use it as a dopant. We used the dye pyronin B chloride as a model compound for the class of xanthene dyes because of its less complicated molecular structure, which facilitates conclusions concerning the doping mechanisms. A detailed conductivity and field effect study of NTCDA doped with pyronin B has been performed to compare with BEDT-TTF as a electron donor [28, 29]. The results showed a strong increase in n-type conductivity. Conductivities up to 2×10^{-4} S/cm were obtained, which is two orders of magnitude higher than obtained using BEDT-TTF as a dopant [22]. Combined FTIR, UV/VIS/NIR and mass spectroscopic measurements suggested the formation of leuco pyronin B during sublimation of pyronin B chloride, and a subsequent charge transfer between dopant and matrix providing free electrons, which increased the n-type conductivity. The method has already been successfully applied for solar cells where materials with lower lying LUMO are used for electron transport. Already at a doping level of 0.2%, the conductivity is well above 10^{-5} S/cm, which is high enough to achieve negligible ohmic losses in a 50 nm thick electron transport layer of an organic solar cell [31, 32].

Based on the successful investigation of pyronin B [27, 28, 29], we extend the doping technique from xanthene cationic dyes (pyronin B and Rhodamine B) to triphenylmethane cationic dyes (malachite green and crystal violet) and then even to acridine dyes (acridine orange). N-type doping of various organic electron transport materials for solar cell applications has been studied in detail using various cationic dyes as dopants. The availability of the leuco base of cationic dyes, such as leuco crystal violet and leuco malachite green allows to test directly the proposed

role of the leuco base as an intermediate in the course of n-type doping. Then, we further extend our work to use acridine orange base as a dopant for organic thin films. A strong doping effect has been observed in fullerene C₆₀, Perfluorinated hexadecafluorophthalocyaninatozinc (II)(F₁₆ ZnPc) and NTCDA using the base forms of cationic dyes as dopants. By now, cationic dyes and their bases have not given rise to a significant n-type doping effect for electron transport materials used in OLEDs. The electron transport materials such as Alq₃ or 3-(4-Biphenyl)-4-phenyl-5-tert-butylphenyl-1,2,4-triazole (Bphen) require dopants with even lower oxidation potential. Currently, our group is trying to use metal complexes with very low ionization potential as dopants for the electron transport materials in OLEDs [33].

This thesis is organized as follows: In Chapter 2, electronic properties, doping processes and conduction mechanisms in organic semiconductors are summarized. After an overview of materials, experimental details and methods applied in the study (Chapter 3), the main part of this work is described in Chapter 4, 5 and 6. Chapter 4 presents xanthene and triphenylmethane cationic dyes as dopants for n-type doping of organic electron transport materials with low-lying LUMO. Chapter 5 is concerned with the leuco bases of the above cationic dyes as dopants for n-type doping of organic electron transport materials. Here, we use leuco crystal violet and fullerene C₆₀ as models of the leuco base and electron transport materials with low lying LUMO to study the doping mechanism. In Chapter 6, we discuss acridine orange base as a dopant for n-type doping for organic semiconductors.

Chapter 2

Theoretical background

2.1 Electronic properties of organic semiconductors

Generally, the carbon-carbon bonds in the organic molecules are either described as σ - or π -bonds. The σ -bonds arise from electrons which are localized between the two carbon atoms. Responsible for the chemical bonding of these materials are mainly the σ -bonds, which determine the direction of the bonding of the carbon atoms and thus the mechanical properties. The σ -bonds are stronger than the π -bonds.

The electronic structure of organic semiconductors is derived from the versatile properties of the carbon atom. A carbon atom possesses four valence electrons. The energy position of the $2p$ -electrons is close to the energy position of the $2s$ -electrons. The energetic configuration allows different kinds of hybridization of the valence electrons (see Figure 2.1). The sp -hybridization consists of two σ -orbitals aligned at one axis and two π -orbitals perpendicular to the σ -bonds. The sp^3 -hybridization is found in diamond, where all valence electrons are hybridized in four tetragonally arranged σ -bonds. In the sp^2 -hybridization, three σ -bonds are arranged in one plane with one π -orbital perpendicular to it. This configuration is characteristic for graphite and the π -conjugated organic semiconductors. The semiconducting properties of π -conjugated organic materials result from the unhybridized p_z -orbitals, which point perpendicular to the σ -bonds. These orbitals overlap and form additional, but weak π -bonds as shown in Figure 2.2. In conjugated π -electron systems, the corresponding electronic states are delocalized over the molecule. The energy gap between π - and π^* -orbital is small because the p_z -orbital overlap is weak.

Organic semiconductors are in general characterized by an energy gap (band gap) between the highest occupied molecular orbital (HOMO) and the lowest unoccupied molecular orbital (LUMO). The HOMO corresponds to bonding π -orbitals and the

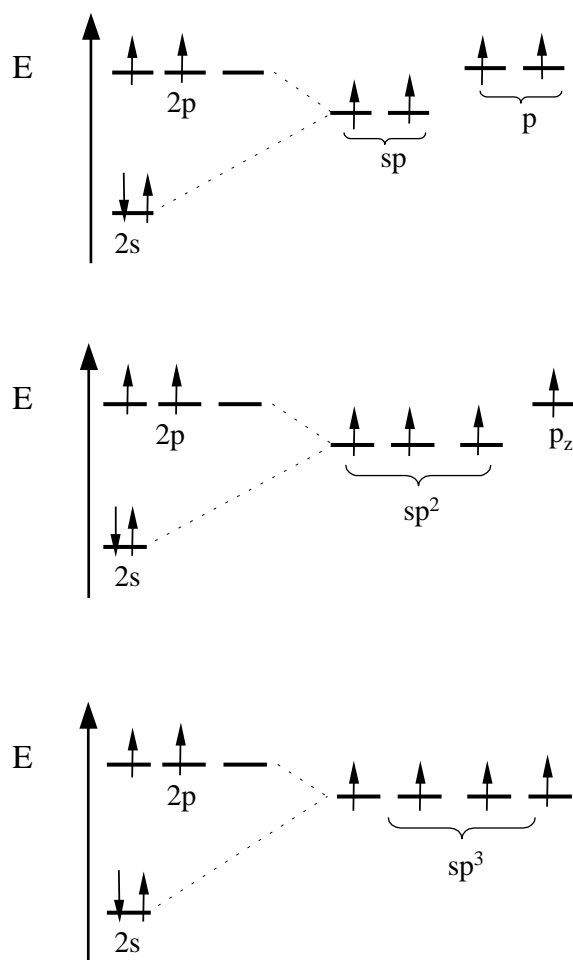


Figure 2.1: Three kinds of hybridization of valence electrons of carbon

LUMO to antibonding π^* -orbitals. The energetic positions of HOMO and LUMO are related to the measured ionization potential (IP) and electron affinity (EA) of the free molecule in the gas phase, respectively. However, the molecule will relax after removal or addition of an electron. The relaxation of the electrons is included in the so called vertical values for IP and EA while the adiabatic values include also the relaxation of the nuclei.

In solids of organic semiconductors, molecules are kept together mainly by the weak van der Waals interaction so that the intermolecular separations are large compared to the separation between atoms or ions of inorganic lattices. Consequently, there is only a weak overlap of the molecular orbitals and intermolecular electron exchange is small. Therefore, the conditions for dark and photoelectric conductance are unfavorable compared to inorganic solids, even though the electrons within the individual molecules are often completely delocalized.

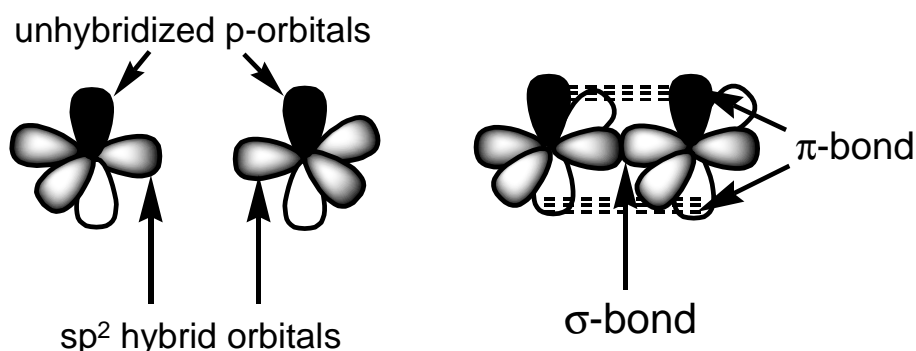


Figure 2.2: Formation of a double bond between two carbon atoms in sp^2 hybridization

Because organic molecules form molecular crystals by means of weak intermolecular interaction forces (van der Waals forces), molecules retain their individuality and only slight changes in the electron structure of molecules occur upon formation of the solid phase. Such an electronic structure determines the basic features of optical and electronic properties of molecular crystals, as well as the peculiarities of the energy structure of neutral and ionized states. The optical spectra of isolated molecules and molecular crystals are often rather similar. The crystal spectrum may completely retain the spectral feature of individual molecules, including their electronic-vibrational structure [34]. On the other hand, certain new optical and electronic properties appear in the solid state, due to collective molecular interactions.

It is essential to combine molecular and solid state aspects in the treatment of optical and electronic properties of molecular crystals. Energy structure and electronic properties of molecular crystals are determined both by crystalline and molecular structure. Thus, for instance, a detectable electrical conductivity and photosensitivity can be found mainly in molecular crystals containing molecules with polyconjugated bond systems, such as aromatic hydrocarbons and conjugated heterocyclic compounds. These molecules contain delocalized, conjugated π -electron systems, as well as heteroatoms with lone pairs of n electrons. It is just the π and n electrons, which are the potential sources of free charge carriers formed through action of light, temperature, doping or injection from contacts. Owing to their specific electronic properties, a large series of molecular crystals consisting of conjugated organic molecules have been named organic semiconductors.

The weak coupling in molecular crystals leads to strong localization of excess charge carriers. Under such pronounced localization, other types of interaction between charge carriers and the lattice become relevant, e.g. electronic polarization of sur-

rounding polarizable molecules. Electronic polarization of the crystal by a quasi-localized charge carrier, i.e., its interaction with valence π and σ electrons of surrounding molecules, determines the self-energy of the given charge carrier, and consequently, the position of its conductivity level in the energy diagram of ionized states of the crystal. The essence of the electronic polarization is that during the localization time of the charge carrier on a definite molecule, i.e., during the hopping time τ_h (Typical hopping times in organic crystals are in the order of 10^{-12} to 10^{-14} s.), a localized charge carrier manages to polarize the electron orbitals, mainly the highly polarizable π orbital, of surrounding neutral molecules in the crystal.

Figure 2.3 summarizes the various types of relaxation processes, relaxation time scales and relaxation energies of charge carriers in anthracene-type crystals [34].

1. The electronic polarization relaxation time ($\tau_e = 10^{-16}$ - 10^{-15} S, see figure 2.3 (a)) is extremely small compared to the hopping time τ_h , i.e., $\tau_h \gg \tau_e$. This means that quasi-localized charge carriers jump from one molecular site to another surrounded by a polarization cloud. Polarization is therefore the dominant, primary-order type of interaction of an excess charge carrier with the surrounding molecular lattice, having a typical energy of 1.5 - 2.0 eV. Consequently, electronic polarization is the most important factor determining the charge carrier's self-energy and, correspondingly, the position of electronic conduction states in the energy diagram of the crystal.

2. A special feature of molecular crystals is the intramolecular vibronic relaxation. The equilibrium configuration of the nuclei in the molecule is changed upon ionization since an additional electron on a molecule changes the binding forces between the different atoms in the molecule. The intramolecular vibronic relaxation time ($\tau_v = 10^{-14}$ - 10^{-13} S, see Figure 2.3 (b)) is of the same order as the hopping time τ_h , i.e., $\tau_v \sim \tau_h$, so that the vibronic relaxation is typically not complete when a charge carrier moves through a crystal. However, it may be complete in disordered materials where carriers move more slowly.

3. For anthracene-type crystals, the lattice relaxation time ($\tau_l = 10^{-12}$ - 10^{-11} S, see Figure 2.3 (c)) is usually greater than the typical hopping time τ_h , i.e., $\tau_l \gg \tau_h$. The interaction energy is in the order of 30 meV. The molecules around the ion change their positions due to the changed spatial extension of the orbitals. This is an interaction between a charge carrier and a lattice phonon, i.e., electron-phonon interaction. The quasi-particle formed is called as a polaron.

In brief, (i) electronic polarization happens much faster than the typical charge transport and carriers move therefore always together with an electronic polarization cloud. (ii) Vibronic relaxation and lattice relaxation happen on a similar time scales as typical charge transport in organic materials. The relaxation can thus be complete

(adiabatic transport) or incomplete (non-adiabatic transport). (iii) In disordered materials, transport is so slow that all three relaxation processes can be assumed to take place completely.

All relaxation processes energetically stabilize charge carriers and thus reduce the band gap. They either lead to hopping transport or to band-conduction with a reduced bandwidth [35].

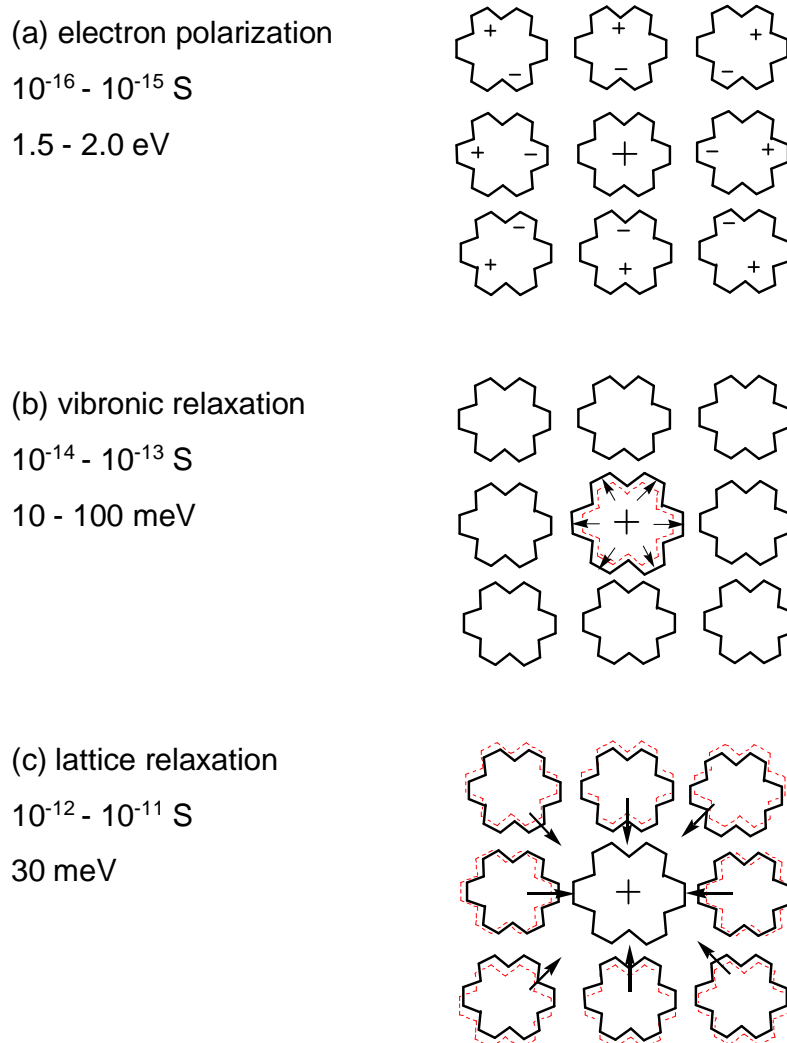


Figure 2.3: Series of relaxation processes together with relaxation time and relaxation energies of a charge carrier in an anthracene-type crystal (values for anthracene, taken from [34]). The red dashed lines in (b) and (c) symbolized the size and the position of the molecules before the relaxation processes.

2.2 Generation of charge carriers - the doping process

Charge carriers can be injected from electrodes, excited with light and induced by electric fields (field effect) as non-equilibrium carriers. Equilibrium charge carriers are generated in intrinsic semiconductors by thermal activation of an electron from the valence band to the conduction band, and then by the separation of the resulting electron and hole. In extrinsic semiconductors, equilibrium charge carriers can be generated by doping. In this section, we discuss n-type doping of organic semiconductors with electron donor-type dopants and their impact on the electron density.

Figure 2.4 shows the mechanism of n-type doping of organic semiconductors. For n-type doping, the matrix is an electron acceptor and the dopant is an electron donor. This process can be expressed as a redox reaction between donor and acceptor by electron transfer from the HOMO of a dopant to the LUMO of a matrix molecule.

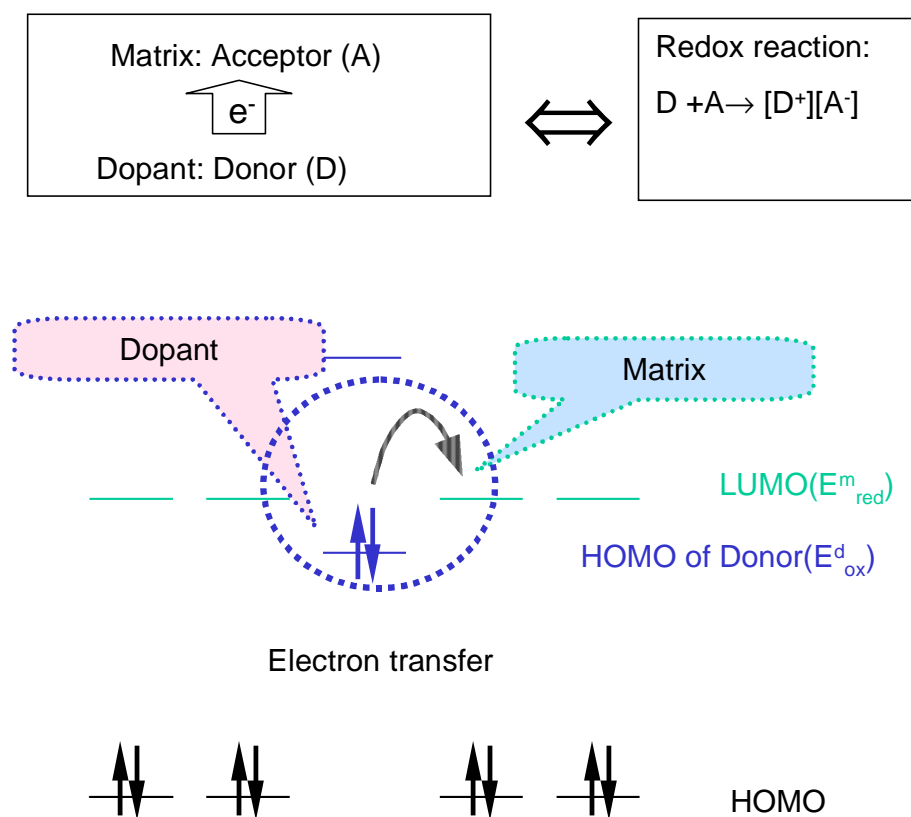
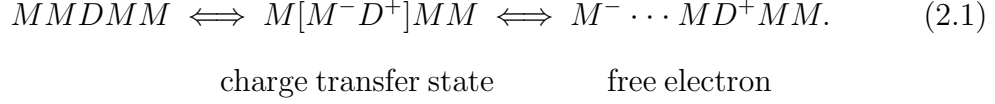


Figure 2.4: Mechanism of n-type doping of organic semiconductors

In the terms of chemistry, n-type doping of a matrix molecule M by a dopant molecule D can be described as follows:



A charge transfer state can be formed when one electron is transferred from the donor to the acceptor which is one of the nearest neighbors of the donor. This intermediate state needs to be dissociated to create a free electron. The final state is assumed to be unbound. The matrix molecule which carries the negative charge is so far away from the ionized donor that it does not feel the Coulomb interaction. Thus free electrons separated from the donor are generated. The free electrons become mobile by hopping in the organic semiconductors and the density of M^- can be associated with the electron density n_e . The energetic difference ΔE between the initial and final state is determined by the solid state electron affinity of the matrix molecule ($EA_{M,M}$) and the ionization potential of the donor in the matrix M ($IP_{D,M}$) as

$$\Delta E = EA_{M,M} - IP_{D,M}. \quad (2.2)$$

When the charge carriers are introduced via donors or acceptors in an extrinsic semiconductor, the dopants form deep or shallow states in the energetic gap between the valence band and the conduction band. In this section, deep donor and shallow donor states will be discussed (Figure 2.5). Deep and shallow acceptor states have been described by Pfeiffer [35].

Deep donor states exist if the donors are only partially ionized at a certain temperature. The Fermi energy E_F is higher than the donor state E_D , i.e., lies between the HOMO of the dopant E_D and the LUMO of the matrix E_C .

$$E_F(T) = \frac{E_C + E_D}{2} + \frac{k_B T}{2} \ln N_D/N_M. \quad (2.3)$$

Here the electron density is given as [29, 36]

$$n(T) = \sqrt{N_M N_D} \exp\left(-\frac{E_C - E_D}{2k_B T}\right), \quad (2.4)$$

N_X is the density of molecule X, k_B the Boltzmann constant. The electron density $n(T)$ is thermally activated by an activation energy $E_n = \frac{E_C - E_D}{2}$.

Shallow donor states are formed if all donors are ionized. The electron density is equal to the dopant density. It is not thermally activated, proportional to the doping ratio, and independent of the temperature. The conductivity only shows the

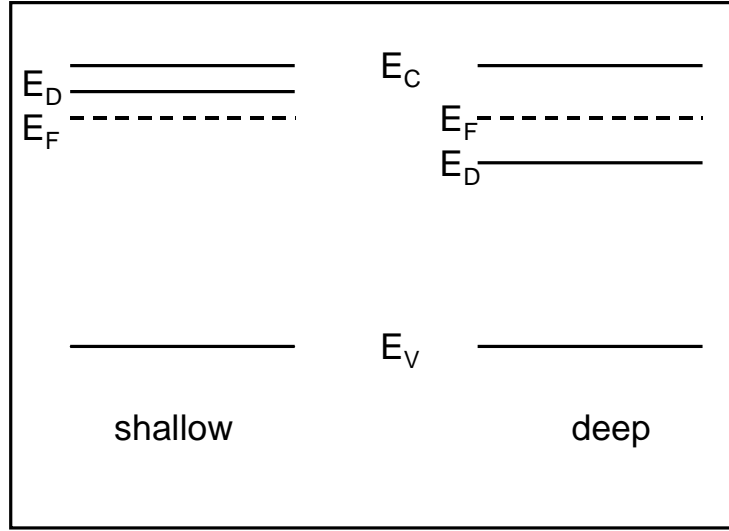


Figure 2.5: The situation of shallow and deep dopants or traps: E_C is the conduction band edge, E_V the valence band edge, E_F the Fermi level and E_D the level of the dopant or trap.

temperature dependence of the mobility. The Fermi level is below the level of the donor. It shifts downwards linearly into the gap with increasing temperature:

$$E_F(T) = E_C + k_B T \ln N_D/N_M. \quad (2.5)$$

2.3 Charge carrier transfer in organic semiconductors

Electronic transport is described by the (local) electric field-induced directional velocity component, $\langle \nu \rangle$, of the mobile charge carriers which is associated with a current density j

$$j = e \cdot n \cdot \langle \nu \rangle, \quad (2.6)$$

where e is the electronic charge unit and n the local charge carrier density. The latter can be altered, in principle, by doping, injection, or photo-generation. The relation between $\langle \nu \rangle$ and the applied electric field E is usually linear for not too high fields (reflecting Ohm's law):

$$\langle \nu \rangle = \mu \cdot E, \quad (2.7)$$

and it is obvious that μ , the charge carrier mobility, is the fundamental (intrinsic) electronic transport quantity that is specific for a given semiconductor material.

A number of experimental methods yield mobility data (either in a straightforward manner or more indirectly). These methods are [37]:

Electric transport methods:

- (a) the time-of-flight (TOF) method [38, 39];
- (b) the xerographic discharge method [40];
- (c) the equilibrium charge carrier extraction method [41, 42];
- (d) drift current methods under limited range conditions [43, 44, 45];
- (e) the space-charge-limited-current (SCLC) method, see e.g. [46];
- (f) the conductivity/concentration (s/n) method [47, 48];
- (g) the field effect transistor (FET) method [49, 50];
- (h) the surface acousto-electric travelling wave (SAW) method, see e.g. [39, 51].

Magnetic interaction methods:

- (1) Hall effect;
- (2) magneto-resistance;
- (3) cyclotron resonance.

TOF and FET are the methods most commonly used to measure the mobility in organic semiconductors.

There are two general types of carrier motion in solids: band model and hopping model. The hopping model emphasizes the molecular character of conduction states, while the band model emphasizes the collective character of conduction states. Both approaches are actually complementary and may be valid, each in its own temperature or charge carrier energy range. As a result of weak intermolecular interaction forces, the band model is suitable for organic molecular crystals only at low temperature and the hopping model is applicable to the room temperature transport of organic thin films.

2.3.1 Band transport in organic crystals

At low temperature, coherent band-like transport of delocalized carriers becomes the prevalent transport mechanism in single crystals of pentacene, tetracene, and other acenes. Very high mobility values have been measured using TOF experiments (up to $400 \text{ cm}^2/\text{Vs}$ for holes in a single crystals of naphthalene at 4.2 K) [52, 53]. In 1974, Burland observed cyclotron resonance of holes in high quality single crystal of anthracene at 2K, the first time such an observation was made in a wide band gap molecular crystal [54, 55]. From the reported values by Burland [55], Dimitrakopoulos and Malenfant determined a hole mobility between 11200 and 64000 cm^2/Vs using the formula: $\mu = (em^*)\tau$, where e is the elementary charge, m^* the effective mass of holes, and τ the hole scattering time [56].

Karl [37] has shown that intrinsic charge carrier transport in some sufficiently pure and perfect low molecular weight organic crystals can safely be described within the framework of coherent Bloch-type band states as long as temperature is sufficiently low. Upon increasing the temperature, increased phonon scattering slows down band transport, the local polarization interactions increase and, hence, the effective mass grows, in conjunction with band narrowing. The charge carriers get increasingly dressed with a polarization cloud leading to successively slower polaron-band conduction. Finally a second, parallel transport channel, thermally activated polaron-hopping transport, is more efficient and takes over. For crystallographic directions with especially weak π -electronic interactions as well as for crystal structures with specific intermolecular interactions (molecular sandwich pairs), electronic transport, however, can be governed by polaron-hopping in a wide temperature range. Orientational molecular disorder in an otherwise perfect crystal lattice fully suppresses band transport.

2.3.2 Hopping transport in disordered organic semiconductors

For disordered organic molecular thin films prepared by physical vapor deposition, the energy distribution of HOMO and LUMO levels of the molecules can be well approximated by a Gaussian-like distribution [57]. The electronic transport in such a system is hopping transport between strongly localized states. Many hopping transport concepts from amorphous inorganic materials can be adapted to organic systems [58, 59, 60]. However, the Gaussian shaped density of states (DOS) and the weak interaction between the molecules leads to some peculiarities in organic systems. A large number of theoretical investigations concerning charge transfer in amorphous organic systems utilizing the Gaussian approach have been published and considerable progress in the analytical description of the problem has been made [61, 62, 63, 64]. An important simplification of the complex hopping transport mechanism was the introduction of the transport energy concept, which had already been developed to describe hopping transport in an exponential band tail of amorphous inorganic semiconductors [65]. This concept allows the complex hopping mechanism in the band tails to be interpreted in terms of a multiple-trapping-and-release model, where the transport energy plays the role similar to the mobility edge in amorphous inorganic semiconductors. This concept was successfully adapted to a Gaussian shaped DOS of amorphous organic systems [58]. However, the Fermi level, a common parameter in the inorganic semiconductor physics, does not appear in many hopping models for transport under thermal equilibrium because the uti-

lization of the Boltzmann approximation in most of the calculations restricts the models to low carrier densities [66, 67].

Vissenberg and Matters [68] presented a percolation model to describe field effect mobility in amorphous organic transistors by taking the Fermi distribution into account. This allows the description of higher carrier densities. Furthermore, Maennig et al. used the percolation approach to explain experimental data on doped organic semiconductors self-consistently [13].

One can use percolation theory regarding the system as a random resistor network (Miller-Abrahams network) [60] to determine the conductivity. The classical percolation problem considers the current flow through *bonds* connecting *sites* in a network. The conductance between the sites m and m' is given by

$$Z_{m,m'}^{-1} = Z_0^{-1} \exp(-2\alpha|\vec{R}_m - \vec{R}_{m'}|) \times \exp\left(-\frac{|E_m - E_F| + |E_{m'} - E_F| + |E_{m'} - E_m|}{2K_B T}\right). \quad (2.8)$$

Here, Z_0^{-1} is a prefactor, α^{-1} the Bohr radius of the localized wave functions, which are assumed to be s -like. \vec{R}_m denotes the position of the m th site, and E_m is the energy of the charge carriers at site m . The first term of the exponential describes the tunnelling between the sites m and m' with spatial distance of $|\vec{R}_m - \vec{R}_{m'}|$ and the second a thermal activation term (Boltzmann term).

The model assumes the following exponential distribution for the density of localized states $g(E)$ in the gap (for electrons in the conduction states):

$$g(E) = \frac{N_t}{k_B T_0} \exp\left(\frac{E}{k_B T_0}\right) \quad (-\infty < E \leq 0). \quad (2.9)$$

Here, N_t is the number of states per unit volume and T_0 describes the width of the exponential distribution. Vissenberg and Matters point out that they do not expect the results to be qualitatively different for a different choice of $g(E)$, as long as $g(E)$ increases strongly with E . The following equation for the conductivity was obtained:

$$\sigma(\delta, T) = \sigma_0 \left[\frac{\pi \delta N_t (T_0/T)^{-3}}{(2\alpha)^3 B_C \Gamma(1 - T_0/T) \Gamma(1 + T_0/T)} \right]^{T_0/T}. \quad (2.10)$$

Here, δ is the fraction of occupied states, i.e., δN_t is the density of charge carriers. B_C is the critical number of bonds per site ($B_C = 2.8$ for a three-dimensional amorphous system) and $\Gamma(z) = \int_0^\infty \exp(-y) y^{z-1} dy$.

Applying percolation theory, it is possible to calculate the conductivity σ as a function of temperature and doping level [13]:

$$\begin{aligned} \sigma &\propto N_D^{T_0/(T_0+T)} && \text{deep donor states} \\ \sigma &\propto N_D^{T_0/T} && \text{shallow donor states} \end{aligned}$$

For the discussion here, the dependence on the doping level is important ($T < T_0$). At a given temperature, the conductivity σ increases superlinearly with the dopant concentration N_D for shallow donor states and sublinearly for deep states. Furthermore, it was pointed out that σ exhibits an Arrhenius-like temperature dependence over a wide temperature range. In fact, hopping in an exponential distribution can be effectively described in terms of activation from the Fermi energy to the transport energy, which optimizes the hopping rates for charge carriers situated below the transport level independent of their initial position [69, 70]. From the model, an equation for the field effect mobility was derived for the case of shallow dopant states [13].

Recently, novel models to provide some insight into hopping transport in the doped disordered organic semiconductors are proposed.

Arkhipov et al. [71, 72] suggest an analytic model of the equilibrium hopping transport in a doped disordered organic semiconductor. The model is based on the effective transport energy concept. It is shown that doping strongly increases the conductivity even if an energetically disordered hopping system is actually doped with deep electron or hole traps, which can explain why unintentional and/or accidental doping is typical in such materials.

Equilibrated carriers mostly occupy site in the deep tail of the DOS while carrier hopping has to occur mostly via much shallower states that belong to the effective transport level [65]. Filling deep states by charge carriers raises the carrier energy distribution but affects the effective transport energy much more weakly [72]. Therefore, increasing charge carrier density will strongly increase the mobility at low to moderate doping levels. At high doping levels, the Fermi level moves toward the center of the DOS distribution and further increase of the dopant concentration will lead to decreasing carrier mobility.

Since the HOMO in most organic solids is deep and the gap separating LUMO and HOMO states is broad, energies of donor and acceptor molecules are normally well below the LUMO and above the HOMO, respectively. Therefore, a double peak Gaussian DOS distribution should be a realistic model for the transport state and donor state [71]:

$$g(E) = \frac{N_i}{\sqrt{2\pi}\sigma_i} \exp\left(-\frac{E^2}{2\sigma_i^2}\right) + \frac{N_d}{\sqrt{2\pi}\sigma_d} \exp\left(-\frac{(E + E_d)^2}{2\sigma_d^2}\right), \quad (2.11)$$

where N_i and N_d are the total densities of intrinsic states and dopants, σ_i and σ_d the Gaussian widths of the intrinsic and dopant DOS distributions, and E_d is the energy shift between these distributions.

The equilibrium distribution of charge carriers, $\rho_{eq}(E)$, is governed by the Fermi-Dirac distribution $f_{eq}(E)$,

$$\rho_{eq}(E) = g(E)f_{eq}(E) = \frac{g(E)}{1 + \exp[(E - E_F)/kT]}, \quad (2.12)$$

with the Fermi energy E_F determined by the condition that the total density of charge carrier must be equal to the density of dopants N_d as

$$N_d = \int_{-\infty}^{\infty} dE \rho_{eq}(E) = \int_{-\infty}^{\infty} \frac{dE g(E)}{1 + \exp[(E - E_F)/kT]}. \quad (2.13)$$

The concept of variable-range hopping suggests that the rate-limiting step in charge transport is jumps of equilibrated carriers, occupying deeper states, to shallower sites that play a role of transport states. According to the Miller-Abrahams equation [73], the carrier jump rate strongly decreases both with increasing distance and energy difference between starting and target sites. A combination of the distance and energy difference that provides the highest jump rate is determined by the temperature, the carrier localization radius $1/\gamma$, and the shape of the DOS distribution. Both analytic considerations and Monte-Carlo simulations have shown that a carrier will most probably jump from a currently occupied state to a hopping site that belongs to the so-called effective transport level of the energy E_{tr} . If a DOS distribution is partially filled with carriers, the equation for the effective transport energy reads [72]

$$\int_{-\infty}^{E_{tr}} dE \frac{g(E)(E_{tr} - E)^3}{1 + \exp[-(E - E_F)/kT]} = \frac{6}{\pi}(\gamma kT)^3. \quad (2.14)$$

Figure 2.6 (from [71]) shows the temperature dependence of the effective transport energy in a doped hopping system as function of the dopant concentration. At higher temperatures, E_{tr} remains almost unaffected by doping. With decreasing temperature, the effective transport level goes down and approaches the Fermi energy. Since the latter depends upon the concentration of dopants, the low-temperature value of the effective transport energy is also sensitive to doping. Once the effective transport energy is found, the average hopping rate $\langle \nu \rangle$ can be readily calculated as

$$\langle \nu \rangle = \frac{\nu_0}{N_d} \int_{-\infty}^{E_{tr}} dE \rho_{eq}(E) \exp\left(-\frac{E_{tr} - E}{kT}\right), \quad (2.15)$$

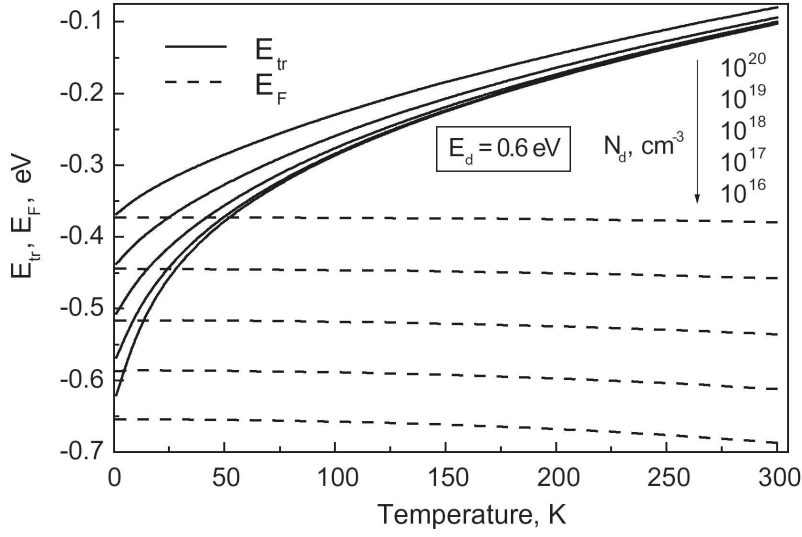


Figure 2.6: Temperature dependence of the effective transport energy and the Fermi energy in a doped disordered hopping system (graph taken from Arkhipov et al. [71]). The following set of material parameters has been used for the calculation: $N_i = 10^{21} \text{ cm}^{-3}$, $\sigma_i = \sigma_d = 0.15 \text{ eV}$, $\gamma = 2.7 \text{ nm}^{-1}$, $\nu_0 = 10^{12} \text{ s}^{-1}$.

where ν_0 is the attempt-to-jump frequency. The occurrence of the effective transport energy virtually reduces the variable-range hopping to the much simpler trap-controlled transport with a broad distribution of localized states.

The weak field equilibrium mobility μ can be estimated from the Einstein relation as $\mu = eD/kT$, with e being the elementary charge and D the diffusion coefficient which is evaluated as $\langle \nu \rangle > \gamma_j^2$. The typical jump distance γ_j is calculated as

$$\gamma_j = \left[\int_{-\infty}^{E_{tr}} dE g(E) \right]^{-1/3}. \quad (2.16)$$

Accordingly, the effective mobility of all carriers is given by

$$\mu = \frac{e\nu_0}{kTN_d} \left[\int_{-\infty}^{E_{tr}} dE g(E) \right]^{-2/3} \times \int_{-\infty}^{E_{tr}} \frac{dE g(E)}{1 + \exp[(E - E_F)/kT]} \exp\left(\frac{E - E_{tr}}{kT}\right). \quad (2.17)$$

Shen et al. [74] interpreted their experimental results (see Figure 2.7) of a molecularly dispersed polymer (MDP) PC(polycarbonate):TMTPD(N,N,N',N'-tetra-p-toly-4-4'-biphenyldiamine) doped with TMTPD⁺:SbF₆⁻ in terms of broadening of the transport manifold due to enhanced disorder caused by the dopants.

Introduction of dipoles in an MDP is known to broaden the HOMO manifold [75]. They have applied the theory of Ambegaokar et al. [76] for calculating the conduc-

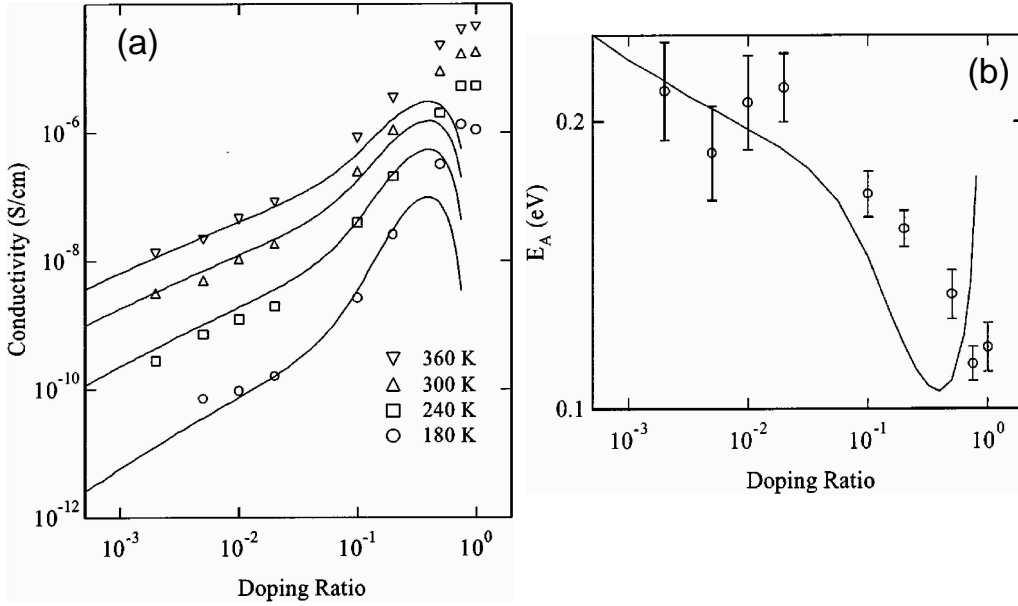


Figure 2.7: TMTPD doped with $\text{TMTPD}^+:\text{SbF}_6^-$ dispersed in polycarbonate taken from Shen et al. [74]. (a) Conductivity (at various temperatures) as a function of the doping ratio. The lines are fits to Eq. 2.18. (b) Activation energy extracted from Arrhenius fits of the experimental data (circles) and the calculated values of conductivity (line) as a function of the doping ratio.

tivity in the presence of strong spatial and energetic disorder. The conductivity σ is estimated by the critical conductance

$$\sigma = ep_0\mu_0e^{-(E_C-E_F)/kT}, \quad (2.18)$$

where μ_0 is a prefactor mobility, p_0 is the number density of hopping sites which is equal to $6.7 \times 10^{20} \text{ cm}^{-3}$ and E_C is the critical energy. E_C determines the half width $\delta_C = E_C - E_F$ of an energetic window in the DOS, centered around the Fermi energy. δ_C provides the minimum fraction η of nearest neighbor connections required for a percolating network of the highest conductances

$$\eta = \int_{-\delta_C}^{\delta_C} \text{DOS}(E - E_F) dE. \quad (2.19)$$

At the same time, Shen et al. [74] limited the application of the model to the regime of low doping.

The solid curves in Figure 2.7 (a) were generated from a four-parameter fit to Equation 2.18, up to a maximum concentration $x \cong 0.2$ (hole density $1.3 \times 10^{20} \text{ cm}^{-3}$). The percolation fraction was taken to be $\eta = 0.25$. The model gives a reasonably

good account of conductivity versus doping ratio in this range, describing the transition between the low and the high doping regimes, while at the same time giving a dependence on temperature which is in agreement with the experiment. The predicted activation energy, superimposed with the experimental data in Figure 2.7 (b), also shows a transition between the two doping regimes. The values of the four fit parameters are $\mu_0 = 0.87 \times 10^{-6} \text{ cm}^2/\text{Vs}$, the intrinsic width of Gaussian DOS $\sigma_0 = 0.086 \text{ eV}$, the dipole moment of the $\text{TMTPD}^+:\text{SbF}_6^-$ complex $P = 28\text{D}$, the Coulomb trap energy $\Delta = 0.36 \text{ eV}$.

Close examination of the fits shows that the increase in dipolar disorder with doping is the primary reason for the transition from the low to the high doping regime, which is manifested by the abrupt reduction of the E_a , as well as the superlinear increase of the conductivity. The resulting broadening of the manifolds of complex and uncomplex TMTPD molecules increases the density of states in the neighborhood of the Fermi energy, which decrease δ_C . This implies an increase in the number of isoenergetic sites which participate in conduction, increasing the critical conductance while simultaneously decreasing activation energy.

Gregg et al. [26, 77, 78] proposed a model that accounts for the predominant influence of electrostatic forces in doped organic semiconductors with low-dielectric constants ϵ . The self-consistent model considers doped organic semiconductors in which the equilibrium free carrier density, n_f , is a small fraction of the total charge density. Here a superlinear increase of conductivity with doping density is universal, n_f increases with applied electric field, and the carrier mobility is field dependent regardless of crystallinity.

They investigated a large number of PPEEB films with dopant concentration from 10^{16} to 10^{19} cm^{-3} (see Figure 2.8). The conductivity of these doped films increased superlinearly with increasing dopant concentration. This superlinear increase has been observed in all quantitative studies of doping in monomeric and polymeric excitonic semiconductors (XSCs) [13, 26, 27, 74, 79, 80]. A simple model based on the factors contained in r can explain the apparent universality of this superlinear increase in conductivity with doping density in XSCs. r is defined as:

$$r = \frac{r_c}{r_B} \approx \left(\frac{q^2}{4\pi n^2 \epsilon_0 k_B r_0 m_e} \right) \left(\frac{m_{eff}}{\epsilon^2 T} \right), \quad (2.20)$$

$r > 1$: Excitonic semiconductor, XSC

$r < 1$: Conventional semiconductor, CSC

where r_c is the critical distance between the two charges, r_B is Bohr radii of carriers, q is the electronic charge, n is the quantum number of the orbital, ϵ_0 is the permittivity

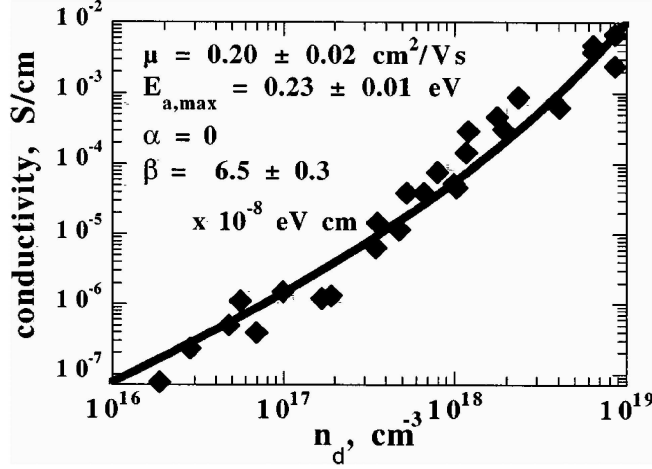


Figure 2.8: Experimental conductivity of PPEEB films (at a field $F = 0.9 \text{ V}/\mu\text{m}$) vs. dopant concentration; data from Gregg et al. [26] and fit to Eq. (2.21).

of free space, r_0 is the first Bohr radius of an electron in a hydrogen atom, m_e is the mass of a free electron in a vacuum, and m_{eff} is the effective mass of the electron in the semiconductor.

The low dielectric constant and the small Bohr radii that are characteristic of XSCs typically result in an $E_{a,max}$ (the maximum activation energy at very dilute dopant concentration) of hundreds of meV. Therefore, E_a is expected to control n_f in XSCs even at room temperature. This fact can explain much of the electrical behavior of XSCs. Gregg attributes the superlinear increase in conductivity with n_d in the PPEEB films to the increasing polarizability of the film caused by the addition of dopant cations with their highly polarizable electrons (most of which are in electrostatically bound but delocalized states), as described by Equation (2.21)

$$\sigma = q\mu_n n_d \exp\left(\frac{-E_{a,max} + \beta n_d^{1/3}}{k_B T}\right), \quad (2.21)$$

where $E_a = E_{a,max} - \beta n_d^{1/3}$ and β is a fitting parameter of order $q^2/4\pi\epsilon\epsilon_0$. The increase in σ above the expected linear increase with n_d is assumed as a function of the distance between bound carriers, $(n_d - n_f)^{1/3} \approx n_d^{1/3}$, rather than the distance between free carriers, $n_f^{1/3}$. This occurs because the high value of $E_{a,max}$, 0.23 eV, ensures that n_f is only a small fraction of n_d at room temperature. However, it remains unclear within Gregg's model why E_a should change with $n_d^{1/3}$. It means that Gregg assumes a kind of Coulomb interaction term, here, while in reality, we are rather dealing with dipole-dipole interaction.

Being based wholly on considerations of electrostatics and the spatial extent of the

carrier wave functions, this explanation may be generalized to other doped XSCs despite differences in chemical structure, purity, and crystallinity. The observed superlinear increase in conductivity with doping density is expected to be, and apparently is, a universal attribute of excitonic semiconductors [13, 26, 74, 79, 80, 81, 82, 83, 84, 85, 86] including inorganic SCs at low T [87, 88, 89, 90]. One consequence of $r > 1$ is that it may be impossible to produce shallow (i.e., mostly ionized) dopants in XSCs at room temperature, independent of the chemistry or redox potentials of the dopant and host.

From all the work presented above, it is apparent that band transport is applicable to extremely high quality, ultra pure single crystals of organic semiconductors and hopping transport is applicable to disordered organic semiconductors, where carrier transport takes place by hopping between localized states and carriers are scattered at every step. Hopping is assisted by phonons and the mobility increases with temperature, although typically it remains very low ($\mu \ll 1 \text{ cm}^2/\text{Vs}$). The boundary between band transport and hopping transport is defined by materials having room temperature (RT) mobilities of the order of $1 \text{ cm}^2/\text{Vs}$ [91, 92]. Thin films of highly ordered organic semiconductors, such as pentacene, have RT mobility in this intermediate range [92, 93, 94]. In some cases, a temperature independent mobility has been observed [46], even in polycrystalline thin films of pentacene [92]. This observation was used to argue that a simple thermally activated hopping mechanism can be excluded as a transport mechanism in high-quality polycrystalline thin films of pentacene, despite of the fact that in some samples containing a large concentration of traps related to structural defects and chemical impurities, the mobility increases with temperature [92]. Trapping at the grain boundaries in polycrystalline films of pentacene and the dependence of trap concentration on the film deposition conditions have been suggested as the main cause of the observed variability of the temperature dependence of mobility [56].

Recently, Kumashiro et al. [95] demonstrated an unusual temperature dependence of electron mobility for C_{60} and Azafullerene (C_{59}N)₂ in thin film field effect transistors. The mobilities monotonously increased in the low temperature range with temperature and then reached a plateau and finally decreased again. It is obvious that a simple hopping model can not explain these phenomena.

Chapter 3

Materials and Experiments

In this chapter, all materials including matrices and dopants used in this study are reviewed (Section 1). After the description of purification of materials (Section 2), main experimental methods are shown in Section 3. Finally, Section 4 presents sample preparation and measurements.

3.1 Materials

3.1.1 Matrices: C_{60} , $F_{16}ZnPc$ and NTCDA

3.1.1.1 C_{60}

Topologically, the C_{60} molecule is a truncated icosahedron (which consists of 12 pentagons and 20 hexagons) with a carbon atom at each of the identical vertices, C=C double bonds along the lines separating hexagons, C-C single bonds along the hexagon-pentagon boundaries, as shown in Figure 3.1. Together with the other members of the fullerene family (C_{70} , C_{76} , ..., bucky-onions, carbon nanotubes, etc.), it represents the purest form of carbon known, not presenting any dangling bonds for interaction with the surroundings, unlike graphite and diamond, the other known forms of carbon. The diameter of the molecule, measured through the carbon nuclei, is about 7 Å. With 120 symmetry operations, the truncated icosahedron is the one closest to spherical of all regular polyhedra. Pure C_{60} crystallizes in an fcc (face-centered cubic) close-packed structure, as one would expect from nearly spherical molecules, only weakly bound by van der Waals forces. Indeed, above about 250 K, the molecules rotate freely [96] and the lattice truly has an fcc symmetry on timescales larger than the typical rotation period, which is in the picosecond range [97]. Below 250 K, most rotational degrees of freedom freeze out and the total symmetry is lowered to simple cubic. In this phase, the molecules are still able

to flip between two stable positions, but below 90 K this also stops [98]. In most studies, the lowered symmetry (the so-called merohedral order) is neglected, but it may be important for some of the more subtle effects. Figure 3.2 shows the energy levels of an isolated C_{60} molecule, obtained from Hückel calculations [99], where the labels indicate the symmetry of the orbital and the number of dashes the degeneracy. In the neutral state, the h_u and t_{1u} levels in the center are the Highest Occupied Molecular Orbital (HOMO) and Lowest Unoccupied Molecular Orbital (LUMO), respectively. Even if the molecule is not neutral, these labels are often retained. The $g_g + h_g$ level is usually called the HOMO-1 level. The t_{1u} LUMO is antibonding with respect to 6:6 bonds and bonding with respect to 5:6 bonds (see Figure 3.2). Since, electronically, the neutral C_{60} molecule is a closed-shell system, and the interactions between the C_{60} molecules are small, solid C_{60} is a band insulator with a band gap of about 2.3 eV [101].

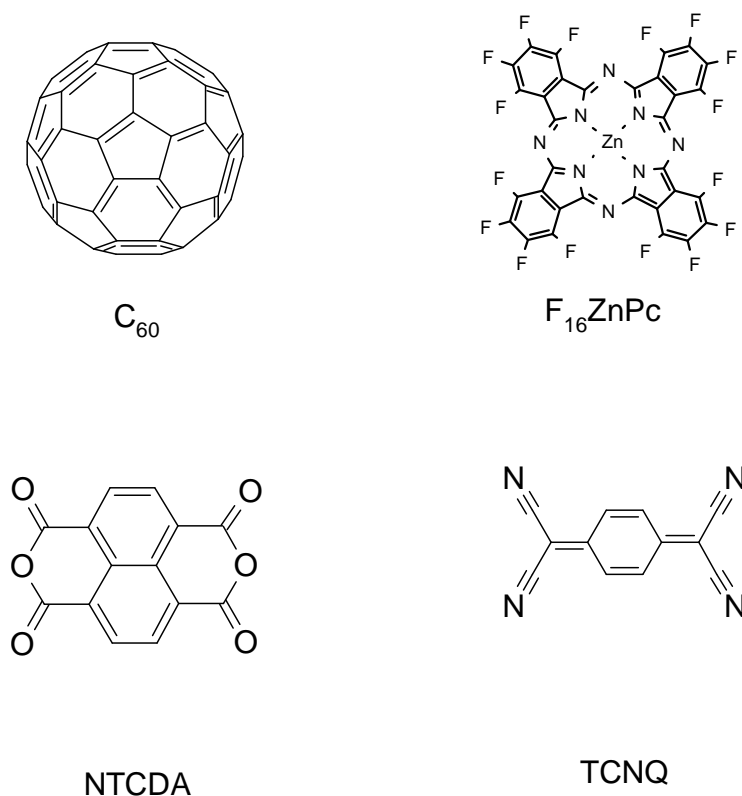


Figure 3.1: Chemical structures of the electron acceptors used in this study.

Because of the large diameter of the C_{60} molecules, the interstitial cavities are large enough to accommodate several species of atoms without destroying the basic C_{60} lattice. In a fcc lattice, there are three interstitial cavities per primitive unit cell, one with octahedral symmetry and two with tetrahedral symmetry, making it possible to

form compounds of the general form $A_1B_2C_{60}$, with A and B metal atoms. The terms intercalation and doping are frequently used to describe the process of filling the interstitial cavities, although both are somewhat inappropriate because of not merely introducing impurities, but forming truly ionic compounds with distinct crystal structures. Many metal- C_{60} compounds have been produced, but most emphasis has always been placed on alkali (and to a lesser degree on alkaline-earth) compounds, since these seem to have the most interesting physical properties. Whether a certain compound will form is determined for a large part by the size of the atom or ion relative to the size of the interstitial cavities. The nearest-neighbor distance in pristine C_{60} is 10 Å. If the molecules are regarded as hard spheres, it is easy to figure out that the radii of the octahedral and tetrahedral cavities are 2.1 Å and 1.1 Å, respectively [102].

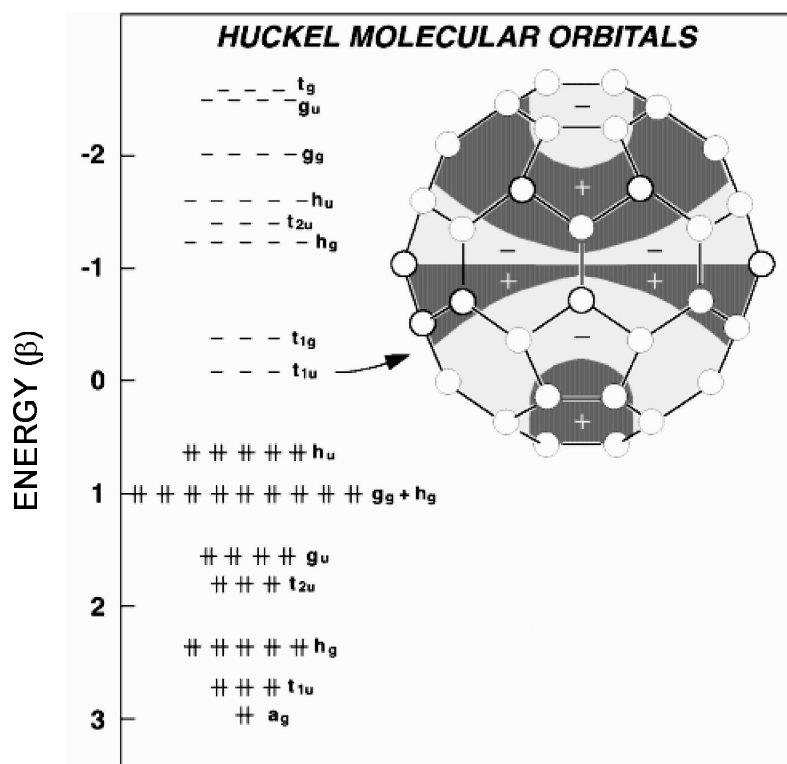


Figure 3.2: Hückel energy level diagram of C_{60} together with one component of the triply degenerate t_{1u} set of molecular orbitals which become populated on alkali-metal doping (taken from R. C. Haddon [99]). Nodes appear mostly on the 6:6 ring juncture bonds indicating predominant antibonding character. By contrast, this orbital is predominantly bonding at the 5:6 ring juncture bonds [100].

The intriguing features of the C_{60} molecule which are also at the heart of many of its interesting properties are its high symmetry, the curvature of its carbon surface,

its relatively large size, and its hollow core.

There are 4×60 valence electrons in the C_{60} molecule, of which 3×60 are involved in typical covalent bonding between the atoms of the molecule. The remaining 60 electrons are mainly of atomic $2p_z$ character. The curvature of the C_{60} surface causes a hybridization of the atomic $2s$ and $2p$ levels into the π and σ orbitals which have hybridization between planar (sp^2) and tetrahedral (sp^3). The electrons in the σ orbitals participate in the C-C covalent bonding, while the π orbitals protrude from the C_{60} surface with asymmetric lobes outside and inside the carbon framework. This hybridization causes the high electron affinity of ~ 2.7 eV in the gas phase [99]. Another consequence of this hybridization is that the tendency for chemical bonding differs for the inside and outside of the molecule. Like other aromatic hydrocarbons, such as benzene, these π orbitals interact to form highly delocalized molecular orbitals which make up the highest energy manifold of occupied molecular electronic states. The large number of such electrons suggests that the spectrum of these molecular orbitals could be very complex; however, the high degree of symmetry greatly simplifies the situation. The interesting electronic properties of an object are mainly derived from its highest filled and lowest unfilled levels. For a molecule, these are known as the HOMO and LUMO. Using the appropriate π atomic orbital basis, the spectrum in the HOMO-LUMO region is well described by the Hückel theory of molecular orbitals, which is essentially a tight-binding model for the π electrons. From this theory, the HOMO is fivefold degenerate ($\times 2$ for the electron spin), the LUMO is threefold degenerate. The symmetries of the HOMO and LUMO may also be found in this theory. The HOMO has h_u symmetry while the LUMO has t_{1u} symmetry (which has 5 nodal lines on the molecule surface). For more details, see [99, 103, 104].

High symmetry also simplifies the molecular vibrational spectrum. Free C_{60} has $3 \times 60 - 6 = 174$ degrees of freedom¹, but there are only 46 distinct vibrational modes (10 Raman active, 4 IR active) [100].

For the negatively charged C_{60} , with a partially filled LUMO, the situation above is complicated by the possibility of a Jahn-Teller distortion. In such a situation, the degeneracy of the t_{1u} level is lifted by a static distortion of the molecule, which amounts to a lowering of the symmetry from pure I_h . Such a distortion is driven by the gain in electronic energy which may outweigh the elastic energy cost of the distortion.

¹There are 3 degrees of freedom for each atom of the molecule, from which we subtract 6: 3 for overall rigid center of mass motion and 3 for rigid rotations. In the solid, these 6 degrees of freedom correspond to the intermolecular vibrational modes and the rotational vibrational modes [105].

The electron-accepting ability of C_{60} is its most characteristic property. It is capable of accepting at least 6 electrons upon reduction because its LUMO is energetically low lying and triply degenerate. When electrochemistry (cyclic voltammetry) was carried out under vacuum using the mixed solvent system acetonitrile-toluene (1:5) at low temperature (-10°C), the potentials measured ($E_{1/2}$) were -0.57 , -0.96 , -1.46 , -1.94 , -2.44 and -2.85 V vs. SCE [106]². The HOMO and LUMO energies of solid C_{60} are about -6.1 eV and -3.7 eV as determined by UPS [108] and estimated by the HOMO-LUMO gap from optical absorption spectrum, respectively [109]. C_{60} is usually an electron acceptor in interpenetrated networks and an electron transport material in solar cells. Its field effect mobility is 8.0×10^{-2} cm^2/Vs in ultra high vacuum (below 10^{-8} Torr) at room temperature [110]. For the field effect measurements, thin films were deposited on the bottom contact field effect transistors (FETs) with chromium and gold pads as source and drain electrodes on SiO_2 , and n-type doped silicon as a gate electrode. Recent experiments have further raised this value to 0.5 cm^2/Vs by organic molecular beam deposition on a bottom contact FET in which p-type silicon was used as a back gate electrode with top SiO_2 as a insulating layer, and Ti/Au and Cr/Au as drain and source electrodes, respectively [111].

C_{60} can be made by arc vaporization of carbon electrodes in a low pressure helium environment [112]. From the remnant soot of such a process, C_{60} can be extracted by dissolution in an organic solvent such as toluene or decalin, and purified by liquid chromatography. To get very pure C_{60} , one can sublime previously purified C_{60} in vacuum at high temperatures (about 500°C).

C_{60} (99.9% or higher), purchased from MER, Tucson, was produced by chromatography and sublimed to remove traces of solvent and other contaminants. The product is a black crystalline powder with powder density of about 0.8 g/cm^3 .

3.1.1.2 $F_{16}\text{ZnPc}$

Perfluorinated 1,2,3,4,8,9,10,11,15,16,17,18,22,23,24,25- hexadecafluorophthalocyaninatozinc (II) ($F_{16}\text{ZnPc}$, see Figure 3.1) tends to behave as an n-type semiconductor with strong electron-withdrawing F atoms and extended π systems, and is used as an electron transport material in organic electronic devices. In field effect transistors, it was found to function as a air-stable n-channel semiconductor with a maximum electron field effect mobility of 0.03 cm^2/Vs [113]. It has a reduction potential of -0.6

²Conversion to SCE has been carried out in this work using: [107]
0 V vs. NHE (Normal Hydrogen Electrode) = -0.241 V vs. SCE
0 V vs. Fc/Fc^+ (Ferrocene/Ferrocenium) = 0.414 V vs. SCE

V vs. SCE [114]. A HOMO energy of -6.9 eV is determined by Hel UPS spectrum in vacuum. A LUMO energy of -5.2 eV is estimated from the HOMO-LUMO gap from optical absorption spectrum. [115]. $F_{16}ZnPc$, purchased from Aldrich (Steinheim, Germany), was purified at least twice by gradient sublimation before use.

3.1.1.3 NTCDA

1,4,5,8-naphthalene-tetracarboxylic-dianhydride (NTCDA, see Figure 3.1) shows n-type conduction in the nominally undoped state. A Field effect mobility of $1 \sim 3 \times 10^{-3} \text{ cm}^2/\text{Vs}$ was obtained for NTCDA-based FETs deposited at a substrate temperature of 55°C for a $12 \mu\text{m}$ channel length device [116]. It is possible to increase the n-type conductivity using an ordinary donor type impurity. The reduction potential of NTCDA has been measured as -0.28 V vs. SCE [117]. Its HOMO and LUMO are about -8 eV and -4.7 eV, respectively [36]. Evaporation of NTCDA onto glass substrates kept at room temperature leads to polycrystalline films. The crystal structure of evaporated NTCDA solids is monoclinic ($a = 7.867 \text{ \AA}$, $b = 5.305 \text{ \AA}$, $c = 12.574 \text{ \AA}$, $\beta = 72.73^\circ$) with two molecules in the unit cell [118]. NTCDA (Aldrich) was purified twice by gradient sublimation before use. Freshly purified materials have a conductivity of about 10^{-10} S/cm . For materials stored longer period in air, the conductivity increases up to 10^{-8} S/cm .

3.1.1.4 TCNQ

7,7,8,8-tetracyanoquinodimethane (TCNQ, see Figure 3.1) is a strong electron acceptor with redox potential of 0.22 V vs. SCE [119] and has a solid-state electron affinity of about 4.5 eV, determined by means of electrochemistry [120]. Many charge transfer complexes with electron donors have been investigated. TCNQ (Aldrich) was purified once by gradient sublimation before use.

3.1.2 Dopants

3.1.2.1 Cationic dyes: crystal violet, malachite green, pyronin B and acridine orange

Crystal violet (CV) and malachite green (MG) (Figure 3.3) are the most important members in the class of triphenylmethane dyes.

The formula weight of $MG(C_{23}H_{25}N_2Cl)$ is 365. In water solution, the long wavelength band absorbs at $\lambda_{max} = 621 \text{ nm}$ and short absorption band at $\lambda_{max} = 427.5 \text{ nm}$ which provides a yellow component to the color (see Figure 3.4). Hence, the green color of the dye is seen.

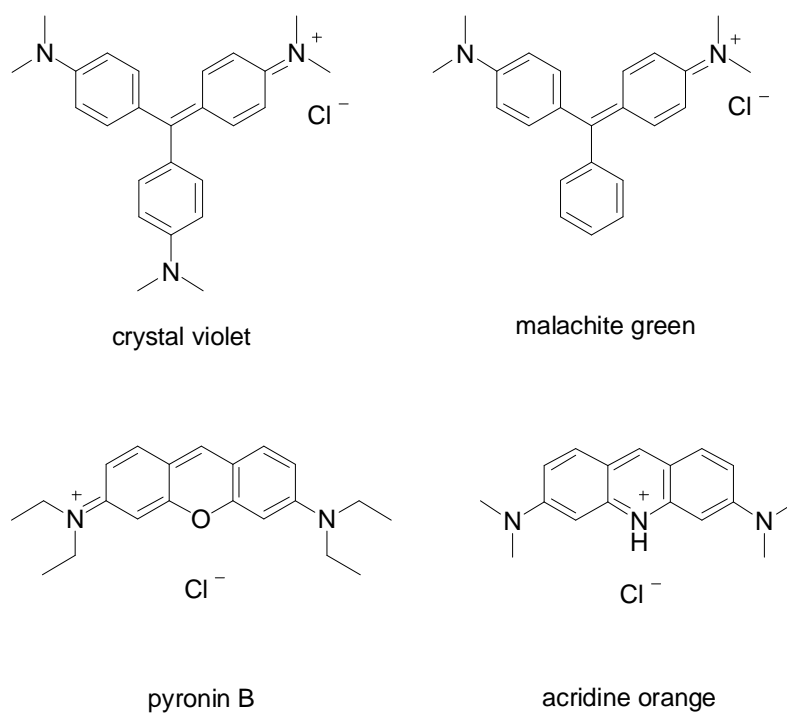


Figure 3.3: Molecular structures of the used cationic dyes

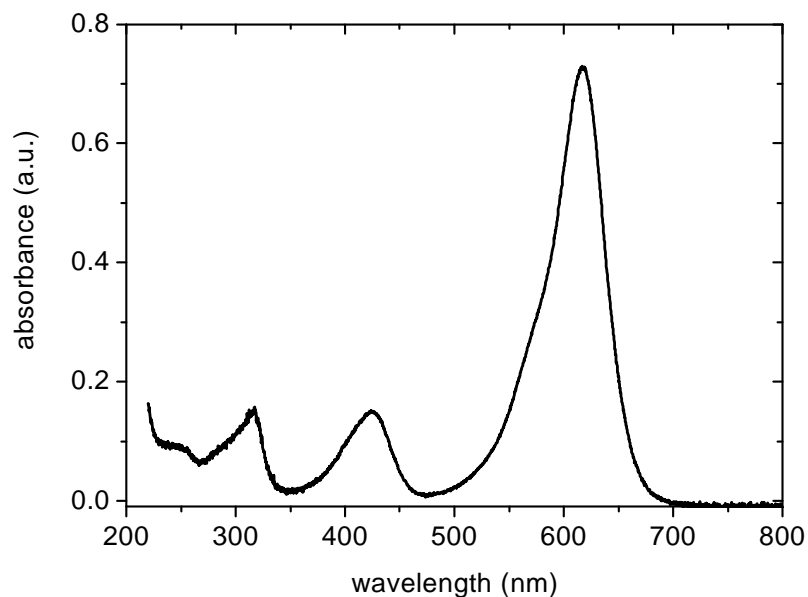


Figure 3.4: UV/VIS absorption spectrum of malachite green in water

Crystal violet ($C_{25}H_{30}N_3Cl$, MW: 407.96) has one more electron-donating amino group $-NR_2$ than malachite green in its molecular structure. Thus, we regard it as one of the key dopants in our study. In methanol, CV only exhibits one absorption

band ($\lambda_{max} = 589 \text{ nm}$) in the visible region of the spectrum (see Figure 3.5). It has a first reduction potential of -0.79 V vs. SCE [121].

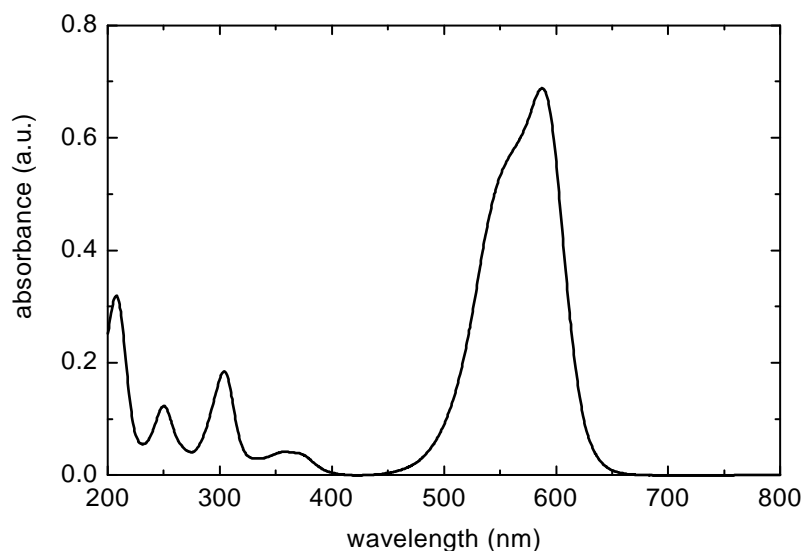


Figure 3.5: UV/VIS absorption spectrum of crystal violet in the methanol solution

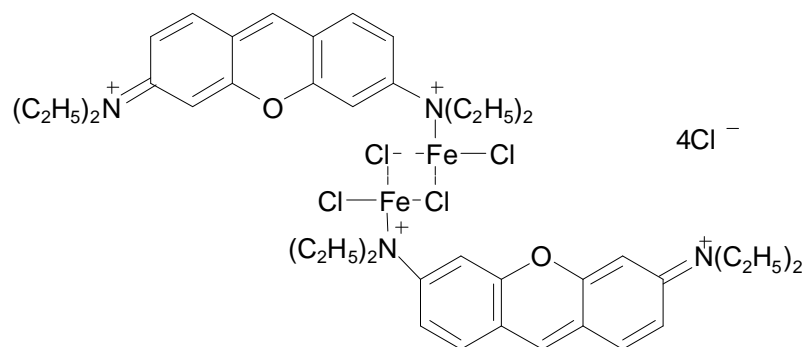


Figure 3.6: Structural formula of commercial pyronin B

The empirical formula of pyronin B (see Figure 3.3) is $\text{C}_{21}\text{H}_{27}\text{N}_2\text{OCl}$ (MW: 358.92). However, normally it is supplied as a complex with FeCl_3 , as shown in Figure 3.6. The reduction potential of pyronin Y, the tetramethyl pyronine, was reported as -0.69 V vs. SCE [122]. Since it is rather similar in molecular structure to pyronin B, the reduction potential of pyronin B should have approximately this value. Acridine orange (AO, see Figure 3.3) is a key member of acridine dyes and has the lowest reduction potential, -1.16 V vs. SCE, in the study of Chan et al [122]. It could thus provide a more powerful dopant than pyronin B. Its empirical formula is $\text{C}_{17}\text{H}_{20}\text{N}_3\text{Cl}$ (MW: 301.828). Commercial AO is a complex with ZnCl_2 ($\text{C}_{17}\text{H}_{19}\text{N}_3$

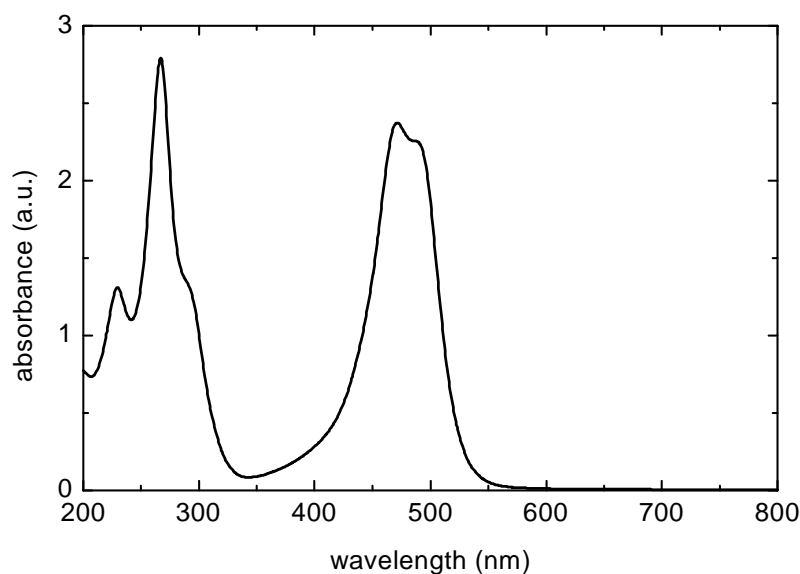


Figure 3.7: UV/VIS absorption spectrum of acridine orange in water

· HCl · 0.5ZnCl₂, MW: 369.96) and red-brown powder. Its UV/VIS absorption spectrum in water is shown in Figure 3.7.

Crystal violet (dye content > 88%), acridine orange (dye content > 55%) and pyronin B (dye content > 30%) from Acros (Geel, Belgium) were used as delivered.

3.1.2.2 Leuco bases: leuco crystal violet (LCV) and leuco malachite green (LMG)

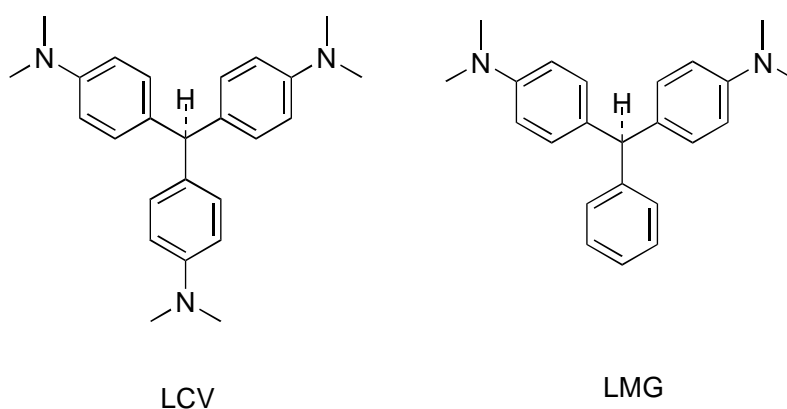


Figure 3.8: Molecular structures of LCV and LMG

LCV (4,4',4''-Methyldynetris(N,N-dimethylaniline)) and LMG (4,4'-benzylidenebis(N,N-dimethylaniline)) (see Figure 3.8) are the leuco bases of CV and MG, respectively. Commercial LCV and LMG are crystalline white powders. In this thesis, LCV is

regarded as a representative of leuco bases of cationic dyes to study n-type doping effect in organic semiconductors because it is a stronger electron donor than LMG. LCV ($C_{25}H_{31}N_3$, MW: 373.54) has an oxidation potential of 0.7 V *vs.* SCE [123]. It is photo-ionized easily in air. LCV (purity > 99%) was used as delivered from Aldrich (Steinheim, Germany) in the study. Figure 3.9 shows the electronic absorption spectra of LCV in DMSO and ethanol.

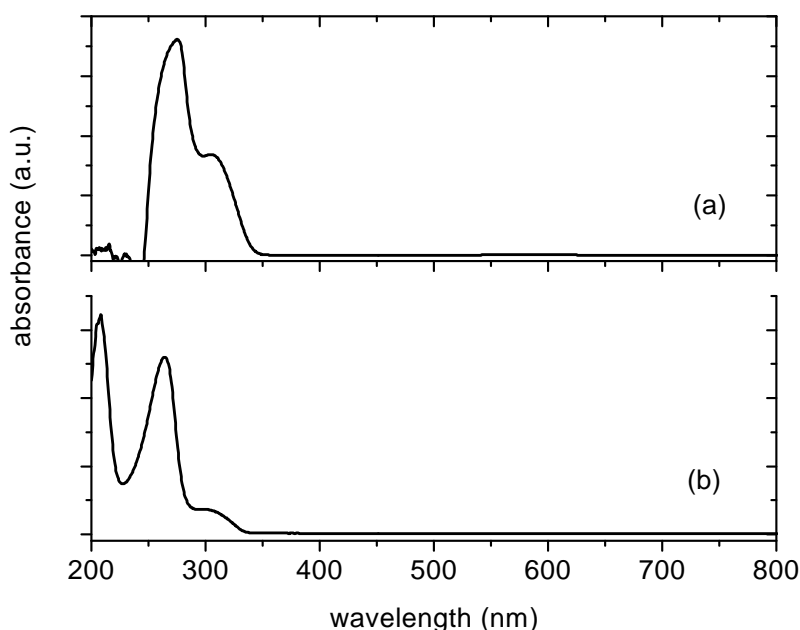


Figure 3.9: UV/VIS absorption spectra of LCV in (a) Dimethyl sulfoxide (DMSO) and (b) ethanol solution.

3.1.2.3 Acridine orange base (AOB)

AOB (see Figure 3.10) is a famous biologic and fluorescent dye ($C_{17}H_{19}N_3$, MW: 265.35). It was purchased from Aldrich (Steinheim, Germany) with purity of about 75% and was purified once by gradient sublimation before use. Its UV-VIS absorption spectrum is shown in Figure 3.11.

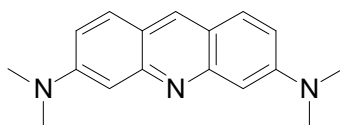


Figure 3.10: Molecular structure of acridine orange base

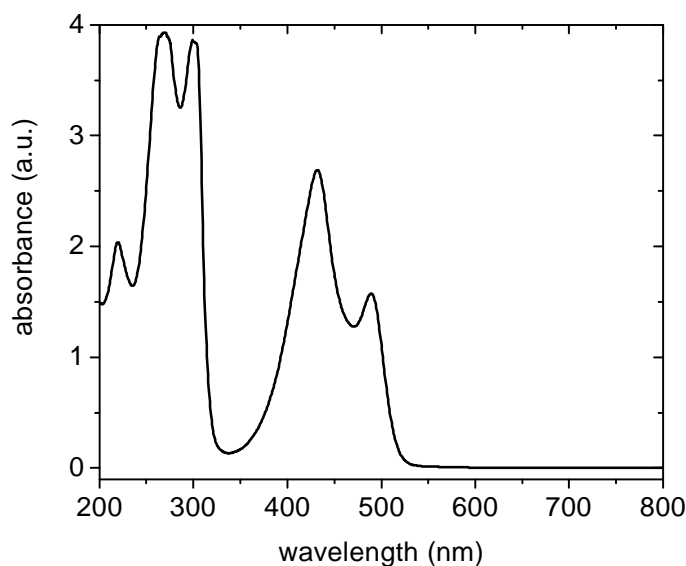


Figure 3.11: UV/VIS absorption spectrum of acridine orange base in the methanol

3.2 Purification of materials

The purity of the matrix materials is essential for assuring that the the doping of thin film is controlled. A low and constant concentration of impurities is needed to get reproducible results. The influence of the unintentional doping can be estimated from the conductivity, but this is not a unambiguous method. Purification may decrease the conductivity due to the reduction of a dopant density, or it reduces the density of traps, which increase the conductivity. Thus, the conductivity can only be used to compare the samples of one single series. For a quantitative evaluation of the impurity density, the measurement of the field effect is necessary. With both an efficient purification method and a successfully sensitive control, highly purified materials can be obtained [124].

The matrix materials used here have been purified by gradient sublimation in high vacuum at least twice before use. The sublimation setup consists of a furnace with three heaters and a quartz glass tube inside. There are 12 separable rings in the quartz glass tube. The tube is evacuated to high vacuum. A temperature gradient exists in the whole heating zone. The highest temperature is applied in the zone where the initial material is placed. The temperature should be as low as possible to prevent the thermal stress of the materials and high enough to sublimate it. Due to the temperature gradient, the impurities and the pure material deposit spatially separately in the tube according to their specific sublimation temperature.

The materials are purified with various parameters like temperature, duration and times of purification. The influence of the parameters on conductivity is weaker compared to the evaporation condition and to water or impurities in the crucible or on the substrate.

When C_{60} is purified, the whole heating zone is first heated up to 350°C under the pressure of $4.4 \times 10^{-4}\text{Pa}$ for 1 hour, and then three heaters are adjusted to 600°C , 400°C and 250°C respectively in order to get a temperature gradient under the pressure of $1.4 \times 10^{-4}\text{Pa}$. After two hours, purified C_{60} is obtained between the 4th and 7th ring. A 70 eV electron impact mass spectrum (EI MS) of C_{60} purified twice using the above method as shown in Figure 3.12. Toluene is used as solvent in the EI MS measurement. The EI MS agrees with the MS given by NIST Mass Spec Data Center [125] except for the peaks at 91 and 92 m/z from the solvent (toluene). Peaks at 720 and 696 m/z are assigned to C_{60}^{+} and C_{58}^{+} , respectively [126, 127]. Peaks at 360 and 348 m/z are assigned to C_{60}^{++} and C_{58}^{++} , respectively [126, 127]. No peaks from impurities are observed. The conductivity of C_{60} purified twice can reach $10^{-8} \sim 10^{-7}\text{ S/cm}$ at room temperature, indicating that our material has a very high purity.

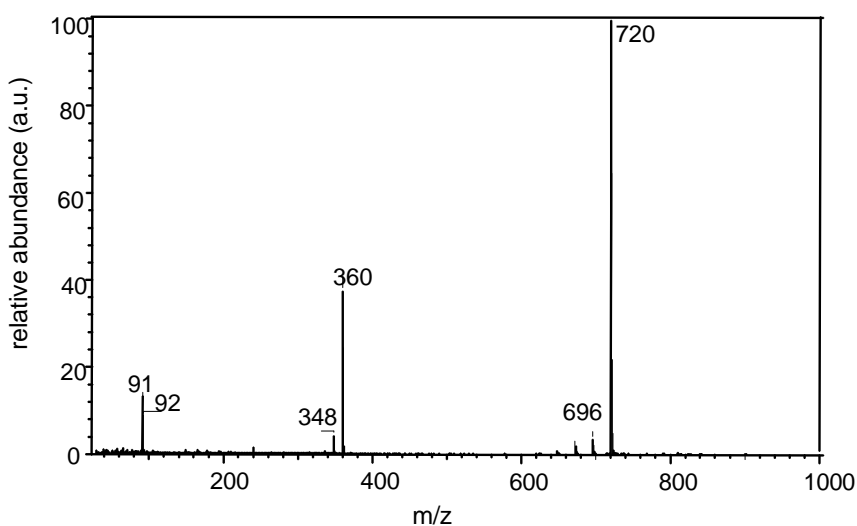


Figure 3.12: Electronic impact mass spectrum of C_{60} purified twice (electron energy 70 eV). The sample is a toluene solution of C_{60}

Using a similar method of purification, the conductivity of NTCDA purified three times is in the range of $10^{-11} \sim 10^{-10}\text{ S/cm}$. The conductivity of $F_{16}\text{ZnPc}$ purified twice is in the range of $10^{-11} \sim 10^{-10}\text{ S/cm}$, too.

3.3 Experimental methods

3.3.1 Field effect experiments

Organic field effect transistors (OFETs) adopt the architecture of the thin film transistor (TFT), which has proven its adaptability with low mobility materials, particularly in the case of amorphous hydrogenated silicon (a-Si:H). Figure 3.13 shows a typical bottom-contact OFET with the organic semiconductor deposited onto the gate insulator and the prefabricated source and drain electrodes. Three device parameters can be calculated from the I-V characteristics of such a three-terminal device: the field effect mobility, the current modulation (the ratio of the current in the accumulation mode over the current in the depletion mode, also referred to as I_{on}/I_{off} ratio) and the threshold V_T . The n-channel OFETs operate in the accumulation mode when the gate electrode is biased positively. A certain concentration of negative carriers is accumulated in the transistor channel, resulting in low channel resistance (on state). When the gate electrode is biased negatively, the channel region is depleted of carriers resulting in high channel resistance (off state). For p-channel OFETs, the electrode polarity is reversed and the field induced carriers are holes.

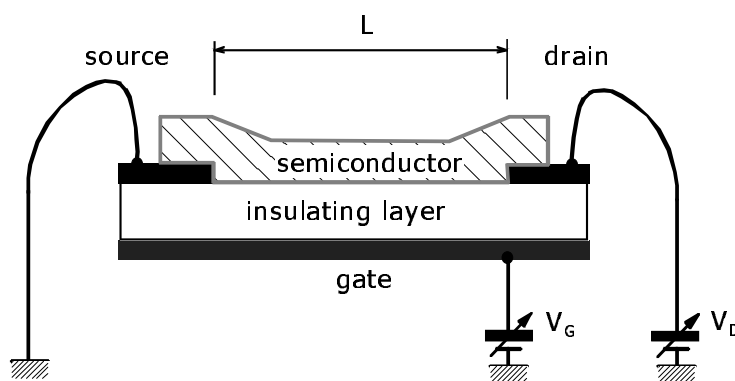


Figure 3.13: Bottom-contact OFET device configuration.

For a given gate voltage V_G , the drain current I_D first increases linearly with the drain voltage V_D (linear regime), then gradually levels off to a constant value (saturation regime). At the same time, the drain current increases when the gate voltage increases. For $V_D \ll V_G - V_T$, I_D is approximately determined by [56, 91]

$$I_D = \frac{WC_i\mu}{L} \left(V_G - V_T - \frac{V_D}{2} \right) V_D, \quad (3.1)$$

where L is the channel length, W the channel width, C_i the capacitance per unit

area of the insulating layer, V_T the threshold voltage, and μ the field effect mobility, which can be calculated in the linear regime from the transconductance

$$g_m = \left. \frac{\partial I_D}{\partial V_G} \right|_{V_D = \text{const}} = \frac{WC_i}{L} \mu V_D. \quad (3.2)$$

For $V_D > V_G - V_T$, I_D tends to saturate (saturation regime) due to the pinch-off of the accumulation layer, and is modelled by the equation

$$I_D = \frac{WC_i \mu}{2L} (V_G - V_T)^2. \quad (3.3)$$

In the saturation regime, μ can be calculated from the slope of the plot of $I_D^{1/2}$ versus V_G . In practice, mobilities derived from the linear regime and from the saturation regime of the OFET characteristics agree reasonably [91]. In our OFETs, $C_i = 37.4$ nF/cm² and $W = 312$ nm.

The apparent mobility in some OFET is gate bias dependent. This might either be an artifact that has to do with contact resistances. However, a gate voltage dependent transconductance is also observed when a manifold of traps is successively filled with increasing V_G , leading to a gradual increase of the effective mobility. Horowitz et al. [128, 129] have developed and described a procedure for the calculation of gate field dependent mobilities in OFETs over wide gate voltage ranges, meanwhile accounting for the series contact resistance that may exist in these devices. For detailed descriptions of OFET, the readers are referred to Refs. [56, 91, 130, 131, 132]. In the field effect study, a 17 W halogen lamp was used to provide diffuse illumination in the chamber during the growth of mixed layers by vacuum-deposition. The light intensity at the position of the sample as measured by a silicon photodiode was 4×10^{-3} mW/cm².

3.3.2 Thermopower experiments

The Seebeck effect and Seebeck measurements have been described by M. Pfeiffer [35] and A. Nollau [36]. The Seebeck effect combined with the conductivity provides a strong tool for the systematic investigation of doping. Here, a simple introduction is given.

Figure 3.14 shows a sample geometry for Seebeck measurements. The sample holder consists of two independently heated copper blocks with a gap of 5 mm as shown. The heating sources are resistant heaters in the blocks. A water cooling system is mounted on the backside of two heated copper blocks. The samples were glued onto the copper blocks with silver paste and clamped. The distance between the contacts is 8 mm.

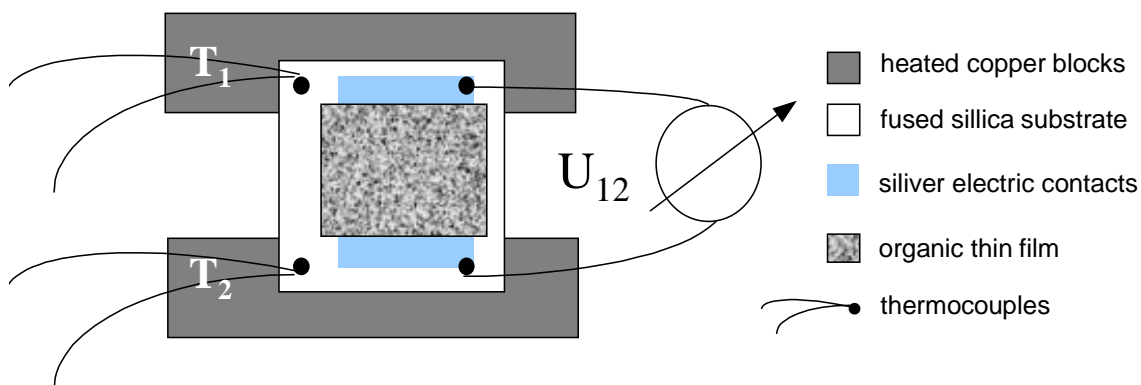


Figure 3.14: Configuration of Seebeck measurements and samples.

The sign of the Seebeck coefficient S is determined by the sign of the majority charge carriers and its absolute value measures the energetic distance between the Fermi level and the main transport energy. This is related with the charge carrier density. The temperature dependence of the Seebeck coefficient and the conductivity give an insight into the transport mechanism.

The Seebeck coefficient is defined as

$$S(T) = \lim_{\Delta T \rightarrow 0} \frac{U_{12}(T, \Delta T)}{\Delta T}, \quad (3.4)$$

where T is the absolute temperature, U_{12} the thermovoltage between the contacts 1 and 2 and ΔT the temperature difference between the contacts 1 and 2 (see Figure 3.14). For unipolar charge carrier transport at one transport level E_C , $S(T)$ is given by

$$S(T) = -\frac{E_C - E_F(T)}{eT}. \quad (3.5)$$

For electron conduction (n-type transport), the sign of S is negative. For hole conduction (p-type transport), S has a positive value.

3.3.3 FTIR spectroscopy

IR-spectroscopy [133, 134, 135] is considered a good technique for the estimation of the degree of charge transfer (Z) even on powdered samples or in solutions. There is a simple relation between the electron density of a certain bond and its force constant [172]. This results in a linear dependence of the frequency ν of some vibration modes of the donor or acceptor molecules on Z . This linear dependence is described by

$$Z = \frac{2\Delta\nu}{\nu_0(1 - \nu_1^2/\nu_0^2)}, \quad (3.6)$$

where ν_0 is the mode frequency measured for a neutral molecule, ν_1 is the frequency of the same mode of the anion and cation radical, and $\Delta\nu$ is the difference between the mode frequency for a neutral molecule and the corresponding frequency of the charge transfer complex [136].

For the electron acceptor TCNQ, the nitrile stretching frequency ω_0 linearly decreases from 2227 to 2180 cm^{-1} when the degree of charge transfer Z varies from 0 and 1 [133].

Due to its very high symmetry, C_{60} has only four infrared-active fundamental vibrational modes. These are the T_u (1-4) modes at 527, 576, 1183 and 1429 cm^{-1} . The response of these frequencies to the addition of charge and Jahn-Teller lowering of symmetry are of considerable interest. In discrete C_{60}^{n-} fulleride salts, data have been reported only for $n=1$ and the frequencies are essentially same as those in intercalated AC_{60} compounds [137, 138]. The T_u (4) mode shows a 34 cm^{-1} decrease relative to C_{60} , while the other frequency are essentially unchanged. These general characteristics must now be considered as diagnostic of the C_{60}^- ion, regardless of the environment [100].

3.4 Sample preparation and measurements

Samples are prepared in a high vacuum chamber (pressure about 2×10^{-4} Pa) equipped with a turbo molecular pump. Organic materials are evaporated from ceramic crucibles. Film thickness and growth rate are monitored by quartz microbalances (Inficon). Mixed layers are prepared by the coevaporation technique (see Fig. 3.13). The rates of the matrix and dopant sources are controlled by means of two separate quartz oscillators. The evaporation rate of the dopant has been adjusted to the desired molar doping ratio R . It can be calculated from the thickness d_x ($x=M$ or D for matrix or dopant, respectively) using

$$R = \frac{N_D}{N_M} = \frac{M_M \rho_D}{M_D \rho_M} \cdot \frac{d_D}{d_M}, \quad (3.7)$$

where M_x is the molar mass of the molecule X and ρ_x the density used to measure the film thickness.

Substrates are cleaned by ultrasonic treatment in acetone and ethanol, and rinsed in deionized water. For conductivity measurements, silver contacts (0.16 mm spacing) have been evaporated on fused silica substrates. The sample preparation was carried out in a high vacuum chamber (pressure below 4×10^{-4} Pa). After heating the substrate at 130°C for 1-2 hours, 50 nm thick organic films with various doping ratios were deposited by co-evaporation from matrix and dopant sources. In order

to check the sample homogeneity, the current through the sample was monitored during deposition with 1 V voltage applied. Electrical measurements were carried out in situ after stabilization of samples was achieved by prolonged annealing at 80°C for several hours. All data reported here are obtained after the samples have reached a steady state.

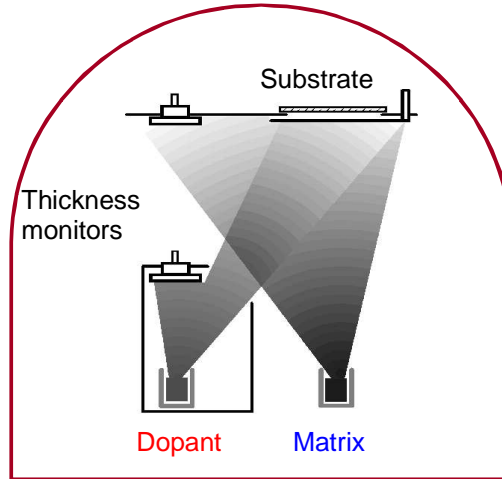


Figure 3.15: Experimental setup of coevaporation of matrix and dopant in high vacuum.

For Seebeck measurements, the temperature are measured by the thermocouples on the sample surface close to the contacts and controlled by a two-channel control unit (Eurotherm). A SMU recorded the thermovoltage and the conductivity. The measurements were completely controlled by computer. For samples with a contact distance of 8 mm and a thickness of 50 nm, the conductivity measurement is limited to 10^{-9} S/cm. Detailed Seebeck measurements are described in Ref. 35 and 36.

For field effect measurements, thin films are prepared on silicon substrates (Fraunhofer Institut für Photonische Mikrosysteme, Dresden) covered by 90 nm SiO_2 as a gate insulator. The substrates carry interdigitated gold contacts having spacing of 10 μm (see Figure 3.14). Similar substrates with 10, 20 and 40 μm contact spacing have been used occasionally to confirm the derived electrical properties (conductivity and mobility) to be independent of the contact separation. It ensures that the calculated values are bulk rather than contact dominated. The film thickness for field effect samples is 50 nm. During layer fabrication, a voltage of 0.1 V has been applied between source and drain contact in order to monitor the development of the current. In the field effect measurement, the magnitude of leakage currents was well below the observed change in source-drain current. Two source-measure-unit SMU 236 from Keithley were used for electrical characterization. They are sensitive and

reliable and therefore applied for the measurement of the field effect and for samples with low conductivity. The conductivities from two kinds of substrates (fused silica substrate and silicon substrate for field effect measurement) have a similar value. Electronic absorption spectra of solution and thin films on fused silica substrates were recorded on a UV/VIS/NIR photometer UV-3100 (Shimadzu). IR transmission spectra of thin films on KCl substrates (International Crystal Labs) were recorded on a Bruker IFS 113V spectrometer in the 400-4000 cm^{-1} range. Thin films for spectroscopy are deposited by evaporation in vacuum or by dip coating from methanol solvent with subsequent drying in air. All optical spectra of freshly vacuum deposited thin films were measured in air as soon as possible (<5 minutes) after samples were taken out from the vacuum chamber. All spectroscopic data were obtained at room temperature in air. For mixed film of C_{60} and LCV or AOB, samples for UV/VIS/NIR absorption and FTIR spectroscopic measurement were encapsulated using epoxy resin in a nitrogen-filled glove box before measurements.

Mass spectroscopic investigations have been carried out on a Finnigan MAT 95 by L. Shapoval in the Institut für Analytische Chemie, TU Dresden.

All electrochemistry was performed in a conventional three-electrode cell using cyclic voltammetry by D. Dung in the Institut für Physikalische Chemie und Elektrochemie, TU Dresden. Platinum working (area 1 cm^2) and counter electrodes (area 3.14 cm^2) were used. A saturated calomel electrode was the reference electrode. The electrolyte was 0.1 M tetrabutylammonium tetrafluoroborate Bu_4NBF_4 (Aldrich 99 %) in acetonitrile (Fischer 99,9 % for DNA analysis). In order to prevent water diffusion from the reference electrode into the working electrolyte, a salt bridge was used. The electrolyte was degassed by Ar for 15 minutes before recording scanning using a potentiostat/galvanostat EGG model 263A.

Chapter 4

Cationic dyes as dopants for n-type doping of organic electron transport materials

In this chapter, n-type doping of various organic electron transport materials for solar cell applications is studied, using various cationic dyes as dopants. Electrical properties of organic thin films doped with cationic dyes are presented. Thanks to the commercial availability of the leuco base of crystal violet, i.e. leuco crystal violet, crystal violet is used as a model compound of cationic dyes to study the nature of the doping effect. Combined FTIR, UV/VIS/NIR and mass spectroscopic measurements suggest the formation of leuco crystal violet during sublimation of crystal violet chloride. A subsequent charge transfer between dopant and matrix, accompanied by a irreversible chemical reaction, will be discussed in detail in Chapter 5. This reaction provides free electrons, which increase the n-type conductivity of organic thin films.

4.1 Electrical properties of n-type organic thin films using cationic dyes as dopants

The conductivity versus the reciprocal temperature for C_{60} doped with CV is plotted in Figure 4.1(a). A thermally activated behavior is found in the measured temperature range. Moreover, the influence of the dopant concentration is clearly visible. The highest conductivity of 8×10^{-3} S/cm at 30°C was achieved for a molar doping ratio of 27:1 (C_{60} :CV). For a doping concentration of 50:1 (C_{60} :CV), we prepared a total of three samples to assess the experimental error. Other samples are assumed to have similar error scales. Figure 4.1 (b) shows the conductivity and activation

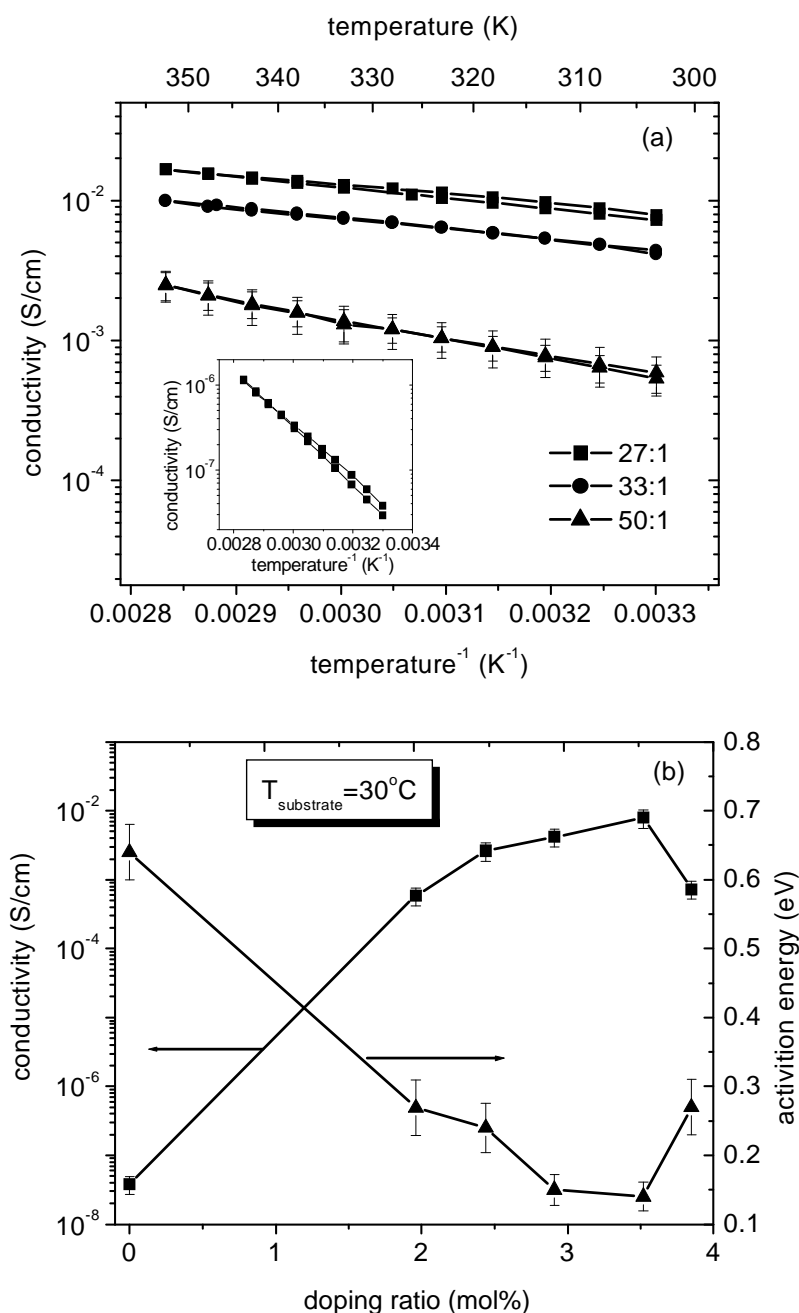


Figure 4.1: Electrical properties of C₆₀ thin films doped with CV. (a) Conductivity *vs.* reciprocal temperature for varying molar doping ratio. The data for the heating and cooling cycle are nearly coincident. The inset shows conductivity *vs.* reciprocal temperature for undoped C₆₀. (b) Conductivity and activation energy (error bars are marked) *vs.* doping ratio. The plots include error bars for one doping ratio (50:1) deduced from a series of nominally identical samples.

energy versus the molar doping ratio. With increasing dopant concentration, a systematic increase of more than 5 orders of magnitude in conductivity is observed, accompanied by a decrease in activation energy from 0.64 eV to 0.14 eV. For higher doping ratios, the conductivity decreases again, probably due to a loss of crystalline order in the matrix lattice [22]. When the samples are exposed to air, the conductivity falls quickly. The effect is reversible. This indicates compensation by oxygen in an n-type semiconductor.

In the case of NTCDA doped with pyronin B [27, 28, 29], already for the lowest doping ratio, 1:1000, the conductivity was increased more than two orders of magnitude. One would expect that for an even lower doping ratio, a doping effect is still visible. However, doping ratios below 1:1000 are not easily achieved by the coevaporation method. The doping ratio of organic layers is therefore in general much higher than for inorganic semiconductors. Unlike heavily doped inorganic semiconductors, however, our doped systems are still non-degenerate because of the weak intermolecular coupling.

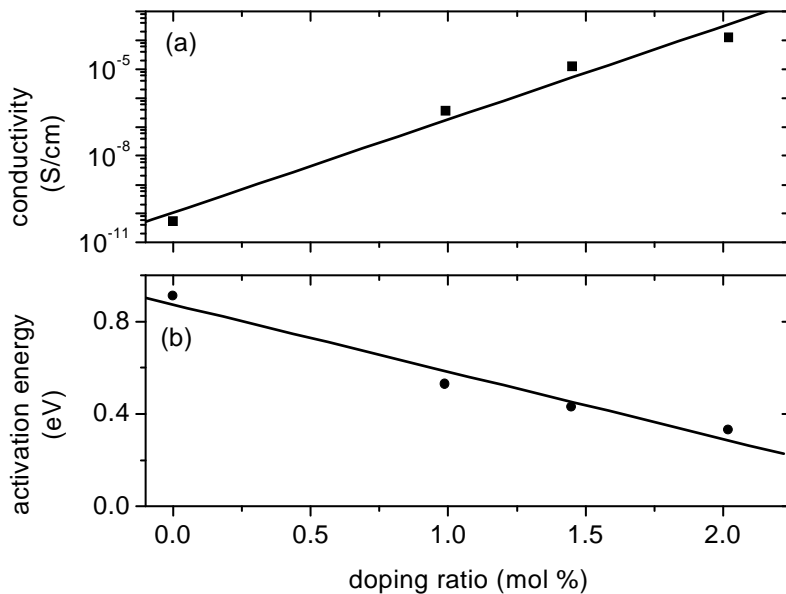


Figure 4.2: Electrical properties of $F_{16}ZnPc$ thin films doped with pyronin B. (a) Conductivity vs. doping ratio. (b) Activation energy vs. doping ratio.

In order to exclude that some chemical reaction specific to pyronin B and NTCDA gives rise to the observed changes in the electrical properties, we also measured the conductivity of $F_{16}ZnPc$ doped with pyronin B. Figure 4.2 shows conductivity and activation energy versus the molar doping ratio. In Figure 4.2 (a), the highest conductivity of 1.3×10^{-4} S/cm at 50°C is achieved for a molar doping ratio of 2.0%,

which is an increase of up to six orders of magnitude compared to undoped $F_{16}ZnPc$. In Figure 4.2 (b), with increasing dopant concentration, a systematic decrease in activation energy from 0.91 eV to 0.33 eV is observed. For very high doping ratio, the conductivity decreased again like in the case of NTCDA doped with pyronin B or C_{60} doped with CV.

Table 4.1: Conductivity and activation energy of several matrices using various cationic dyes as dopants. All conductivity data are measured at 30°C unless specified differently in the table.

Matrix	Dopant	Doping ratio (mol%)	Conductivity (S/cm)	Activation energy (eV)
C_{60}	no	0	3.80×10^{-8}	0.64
	pyronin B	2.90	1.39×10^{-3}	0.27
	CV	3.52	7.90×10^{-3}	0.14
$F_{16}ZnPc$	no	0	5.60×10^{-11} (50°C)	0.91
	pyronin B	2.06	3.70×10^{-5}	0.34
	MG	3.00	1.19×10^{-6}	0.39
NTCDA	no	0	6.20×10^{-11} (40°C)	0.54
	pyronin B	2.06	9.29×10^{-4}	0.22
	MG	2.00	1.94×10^{-4}	0.21
	CV	3.38	6.67×10^{-4}	0.29

In order to prove the doping technique to be universal, various organic electron transport materials for solar cell applications have been doped using various cationic dyes as dopants. Table 4.1 gives conductivity and activation energy results for doped and undoped thin films. An obvious increase in conductivity of doped matrices can be seen compared to undoped matrices. It indicates that cationic dyes were effective dopants for n-type doping of organic electron transport materials with moderate acceptor strength. In addition, all dopants lead to a decrease in activation energy. The results can be immediately used to improve the performance of organic solar cells employing these materials as electron transport layers [31, 32].

Up to now, we have shown that there is clear evidence for a doping effect using cationic dyes. However, the nature of this kind of dopants has not been discussed yet. In order to answer this question, several spectroscopic measurements have been carried out, as described in the next sections.

4.2 Mass spectroscopy

To study the origin of the apparent doping effect, we investigated the vapor of CV by 70 eV electron impact mass spectroscopy (EI MS). Due to the ionic nature of CV, a chemical change is expected in the sublimation process used to get neutral

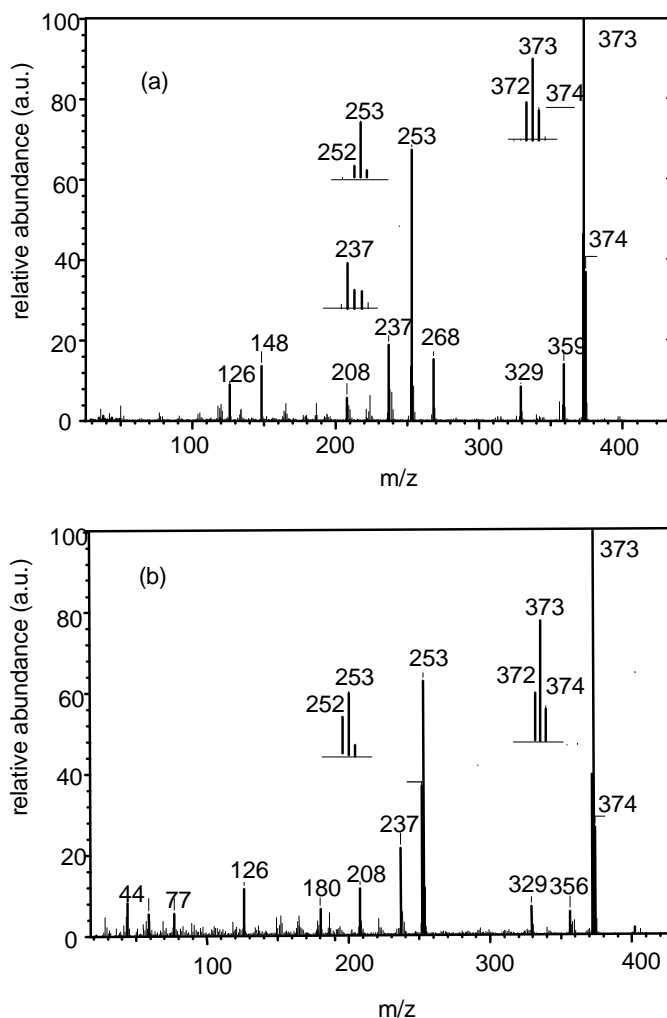
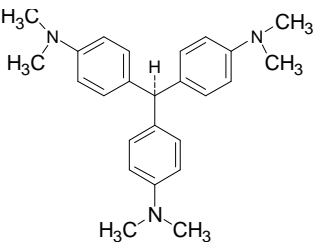
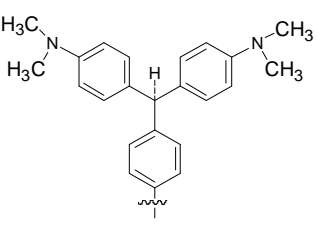
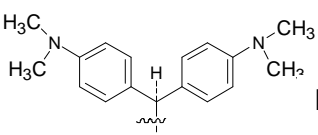


Figure 4.3: Electron impact mass spectra of (a) CV and (b) LCV (electron energy 70 eV). The temperature of the aluminum crucible used to evaporate the material was 200°C.

and volatile species. In the mass spectrum of CV (Figure 4.3 (a)), the peak with maximum abundance is at 373 m/z. It does not correspond to the molecular ion of CV [$m(M)=372$ m/z], but to the $M+1$ ion. As we know, EI MS cannot produce mass numbers higher than the molecular ion. Thus the 373 m/z peak may be due to the existence of hydrogenated CV (possibly LCV) in the gas phase. When similar 70 eV EI MS is measured for LCV, the molecular ion peak at 373 m/z can be clearly

Table 4.2: Assignment of the major peaks in mass spectra of evaporated CV and LCV (Figure 4.3). M and M_N ($N=1, 2, 3, 4$) are molar mass of the molecular ion and fragments.

Peak	Assignment
373 (M)	 <p style="text-align: right;">M (LCV)</p>
329 (M_1)	 <p style="text-align: right;">$M_1=M-44$ ($N(CH_3)_2$)</p>
253 (M_2)	 <p style="text-align: right;">$M_2=M-120$ ($(C_6H_4)N(CH_3)_2$)</p>
237 (M_3)	$M_3=M_2-15$ (CH_3)-1(H)
208 (M_4)	$M_4= M_2-44$ ($N(CH_3)_2$)-1(H)

seen in the mass spectrum (Figure 4.3 (b)). This gives a hint that LCV could be produced during the evaporation of CV. Besides the main peak at 373 m/z assigned to the molecular ion of LCV in both mass spectra, peaks at 329, 253, 237, 208 m/z can also be assigned to respective fragments (see Table 4.2). For other weaker peaks, an assignment is not possible. However, we should note that peaks at 148, 268 and 359 are only observed in EI MS of sublimated CV. We excluded the possibility that the peaks are from impurity according to Electrospray ionization mass spectroscopy

(ESI MS). Unfortunately, by now we have not been able to exactly assign them to specific fragments. We speculate that they could be related with the product being formed when one CV provides another CV with one hydrogen to form LCV.

4.3 Optical spectroscopy

4.3.1 Pure evaporated CV in solid thin film

We then carried out optical spectroscopy of a vacuum deposited thin film of CV and coatings deposited from methanol solution of pristine CV and LCV (see Figure 4.4). The electronic absorption of the 20 nm thick CV thin film prepared by vacuum deposition is shown in Figure 4.4 (b). Absorption bands are observed at 207, 270, 312 and 357 nm, which are similar to bands in the absorption spectrum of LCV coated from methanol solution as shown in Figure 4.4 (a), apart from the band at 357 nm. The slight difference between the spectra in Figure 4.4 (a) and Figure 4.4 (b) is attributed to a different morphology of the two kinds of samples. Usually,

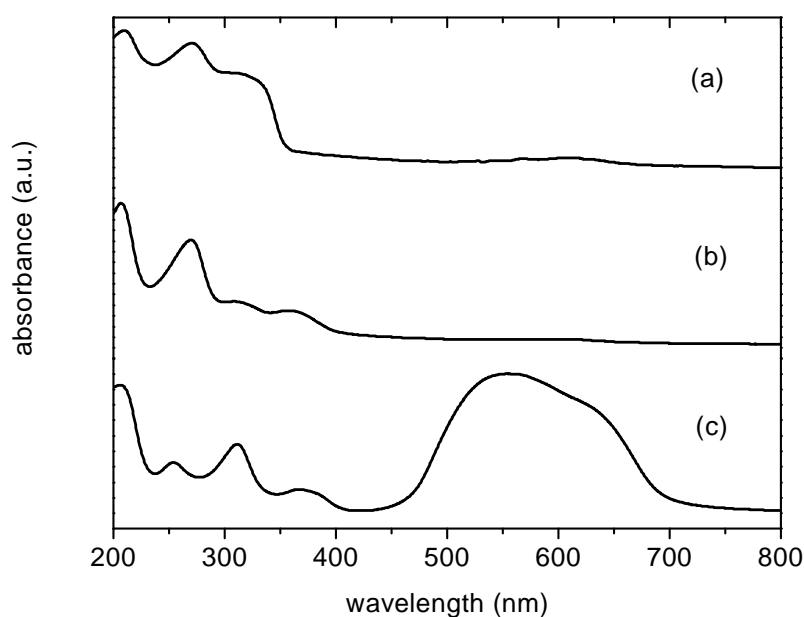


Figure 4.4: Optical absorption spectra of (a) an LCV coating prepared by evaporating the solvent of a LCV methanol solution, (b) a CV thin film prepared by vacuum deposition and (c) a CV coating prepared by evaporating the solvent of a CV methanol solution.

vacuum-deposited thin films of CV were of high-quality and uniform. However, we could not obtain a smooth film by the evaporation of solvent, but got a film with many defects. The morphology of samples influence the electronic absorption bands.

In contrast to the absorption of pristine violet CV (Figure 4.4 (c)), evaporated CV is as colorless as LCV. The main absorption band of CV in the visible spectral range around 556 nm disappears in Figure 4.4 (b). Therefore, we can assume that CV is reduced into its neutral form, namely the leuco base LCV, during sublimation. The broad absorption band of the CV coating in Figure 4.4 (c) is attributed to polymeric aggregates. The peak around 556 nm is due to reversible aggregation to a dimer [139].

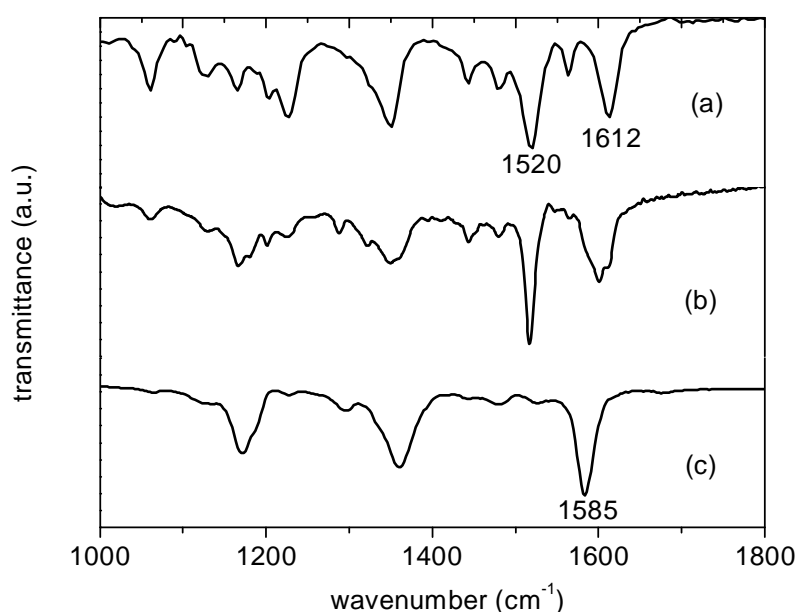


Figure 4.5: FTIR spectroscopy of (a) an LCV coating prepared from methanol solution, (b) a CV thin film prepared by vacuum vapor deposition and (c) a CV coating prepared from methanol solution.

A comparison of the FTIR transmission spectrum of an evaporated thin film of CV with the spectra of LCV and CV solution coating film is shown in Figure 4.5. The spectrum of evaporated CV in Figure 4.5 (b) exhibits peaks which are completely different from pristine CV [Figure 4.5 (c)] and similar to pristine LCV [Figure 4.5 (a)]. This is further evidence that CV was reduced into LCV during sublimation. The two dominant peaks at 1612 cm⁻¹ and 1520 cm⁻¹ in the IR spectrum of LCV correspond to a benzene ring mode (weakly coupled to an alkyl deformation) and a N-ring stretching mode, respectively [28, 140]. The N-ring stretching mode is sensitive to changes in the electron structure of the molecule. Indeed, when changing from the neutral molecular to the cation, its vibration frequency increases by 65 cm⁻¹ from 1520 cm⁻¹ in LCV to 1585 cm⁻¹ in CV as a result of the increased double-bond character.

From all spectroscopic data, we can conclude that the leuco base of crystal violet, LCV, is formed during sublimation of CV in vacuum. The same phenomenon is observed for malachite green. Therefore, we can generalize that cationic triphenylmethane dyes become reduced to their leuco base forms when transferred into the vapor phase in vacuum. We drew a similar conclusion for the xanthene dye pyronin B [27, 28, 29]. However, we have now been in the position to test our conclusion with an authentic sample of the leuco base LCV. We suggest that a CV radical (CV^\bullet) is first formed in the crucible by thermal dissociation during sublimation. Then CV^\bullet immediately transforms thermally into LCV by hydrogen abstraction from the methyl of aniline in CV. Subsequently, some dimers or oligomers could be formed in the crucible because C-H bonds of methyl are broken.

4.3.2 Mixed films of TCNQ and CV

The oxidation of evaporated pyronin B by air has been seen in optical spectra [27, 28, 29]. When evaporated CV was exposed to air for 15 hours under daylight, the colorless sample becomes violet. It means LCV formed during the sublimation is to some extent oxidized by air under daylight. The evidently formed LCV undergoes

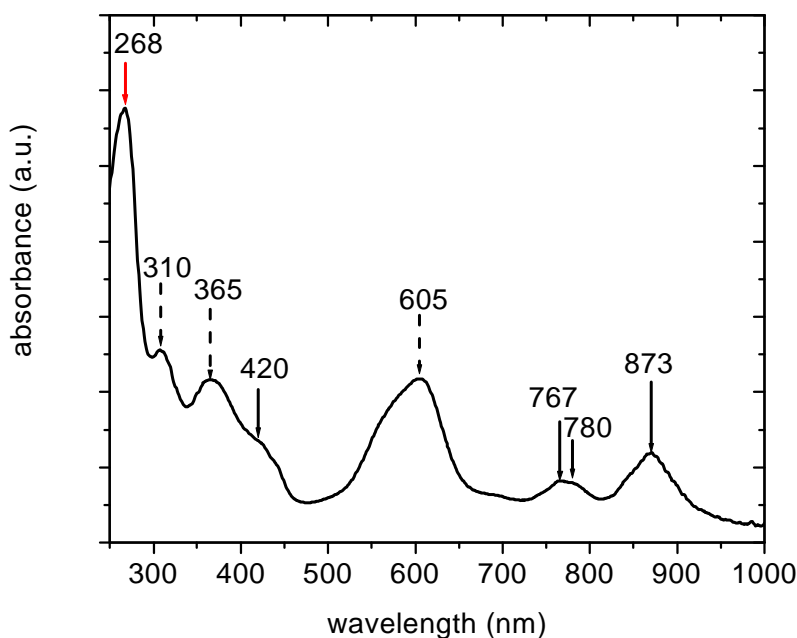


Figure 4.6: Electronic absorption spectrum of a mixed layer of TCNQ and CV (2:3). The dashed arrows mark the absorption bands of CV (310, 365, 605 nm); The solid arrows mark absorption bands of the TCNQ anion (420, 767, 780, 873 nm); The red solid arrow marks absorption band of LCV (268nm).

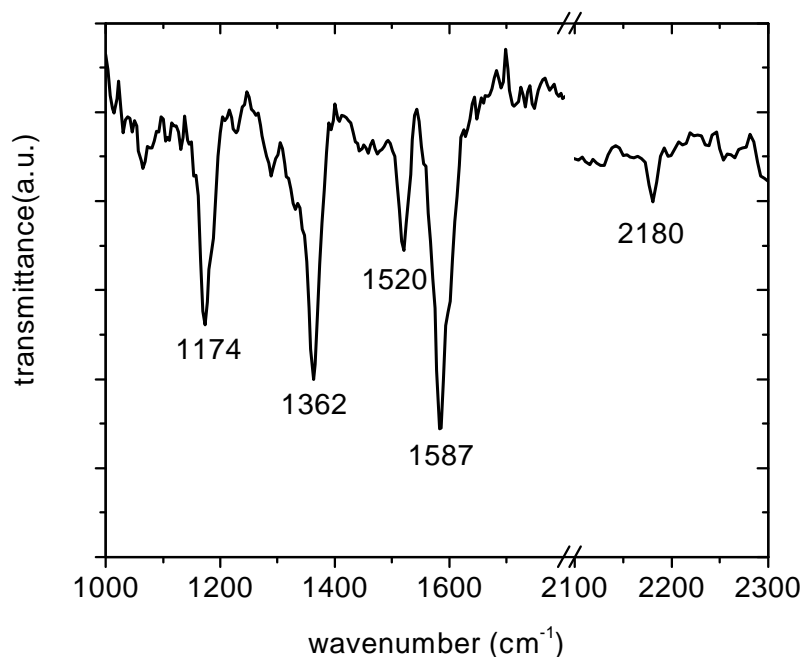


Figure 4.7: FTIR spectrum of a mixed layer of TCNQ and CV (2:3). Peaks at 1174, 1362 and 1587 cm^{-1} are assigned to CV^+ . 1520 and 2180 cm^{-1} , corresponding to LCV and TCNQ^- , respectively.

a similar oxidation process when it is doped into a matrix of the organic acceptor tetracyano quinodimethane (TCNQ). At the same time, TCNQ anions are formed. This charge transfer is responsible for the increasing electron density by doping. The properties of charge transfer complexes based on TCNQ have been widely investigated [133, 141]. In particular, optical spectra of TCNQ and its radical anion have been studied and understood very well. Optical spectra of a mixed film of TCNQ and CV prepared by coevaporation give powerful evidence for the charge transfer between evaporated CV and TCNQ. UV/VIS/NIR and FTIR spectra of 2:3 (TCNQ:CV) doped film are measured immediately after breaking the vacuum. Figure 4.6 shows the UV/VIS/NIR absorption data. Bands around 310, 365, 605 nm assigned to CV cations are present immediately after sample preparation. This means that the reduced form of CV has been oxidized by TCNQ. Concerning the bands assigned to the TCNQ anion [141], nearly all absorption bands can be observed. There are strong peaks around 873 and 767 nm, and shoulder peaks around 420 and 780 nm, respectively. No obvious absorption band of neutral TCNQ at 392 nm is observed. However, a peak at 268 nm assigned to LCV is clearly visible. It means that CV is excessive in stoichiometry for the intended 2:3 ratio of TCNQ:CV. The molecular vibration modes of TCNQ and its anion radical have been well studied

by FTIR and Raman [133, 142]. Charge transfer from an electron donor leads to shifts of several peaks in FTIR spectra, for example the nitrile stretching mode in TCNQ. Usually, the vibration frequency of this mode is a linear function of the degree of charge transfer (Z) [133]. Thus, the degree of charge transfer between evaporated CV and TCNQ can also be determined from an FTIR transmission measurement. The FTIR spectrum of the doped sample in the spectral range from 2100 cm^{-1} to 2300 cm^{-1} (the nitrile stretching vibration mode of TCNQ is sensitive) and from 1000 cm^{-1} to 1800 cm^{-1} is shown in Figure 4.7. The peak at 2180 cm^{-1} corresponds to TCNQ anion ($Z=1$). A peak at 2227 cm^{-1} corresponding to neutral TCNQ can not be found. This is further evidence that all TCNQ has been reduced into TCNQ anion. Between 1000 cm^{-1} and 1800 cm^{-1} , we can also observe both a peak at 1520 cm^{-1} corresponding to LCV and peaks at 1174 , 1362 and 1587 cm^{-1} corresponding to CV. This confirms the conclusion from the above absorption spectrum that some LCV exists in the mixture of evaporated CV and TCNQ.

4.3.3 Mixed films of NTCDA and pyronin B

We also carried out a similar investigation of NTCDA: pyronin B by coevaporation. Figure 4.8 and 4.9 show FTIR and VIS absorption spectroscopy of a doped sample (1:1), respectively. Compared to freshly vacuum-deposited films of pyronin B (Figure 4.8 (a)) and NTCDA (Figure 4.8 (c)), we find that the FTIR spectrum of a freshly mixed film of NTCDA: pyronin B (1:1) (Figure 4.8 (b)) is only a combination of leuco pyronin B and NTCDA. No pyronin B cations are observed in the optical spectra. This is expected because deep donor states are formed due to the low electron affinity of NTCDA and therefore only a small fraction of the dopants are ionized. The observed increase in conductivity [27, 28] after preparation of the doped films is probably due to the slow transition from the leuco form to the cation of pyronin B in the layer. When the mixed sample is exposed to air, leuco pyronin B in the mixed film is gradually oxidized as indicated by an increase of the peak at 550 nm in Figure 4.9 under exposure to air. When other weak acceptor-type matrices, i.e. C_{60} and $F_{16}ZnPc$, are doped with cationic dye by coevaporation in vacuum, optical spectra measured in air of fresh samples immediately after breaking vacuum do not show clearly the existence of oxidation states of reduced cationic dyes either. Optical spectra obtained are still nearly a spectral combination of leuco bases of cationic dyes and matrices. It should be noted that no illumination was used during the coevaporation and measurement of the samples and the samples had never heated after coevaporation. This shows that it is hard to achieve electron transfer from leuco bases of cationic dyes to electron transport materials with moderate acceptor

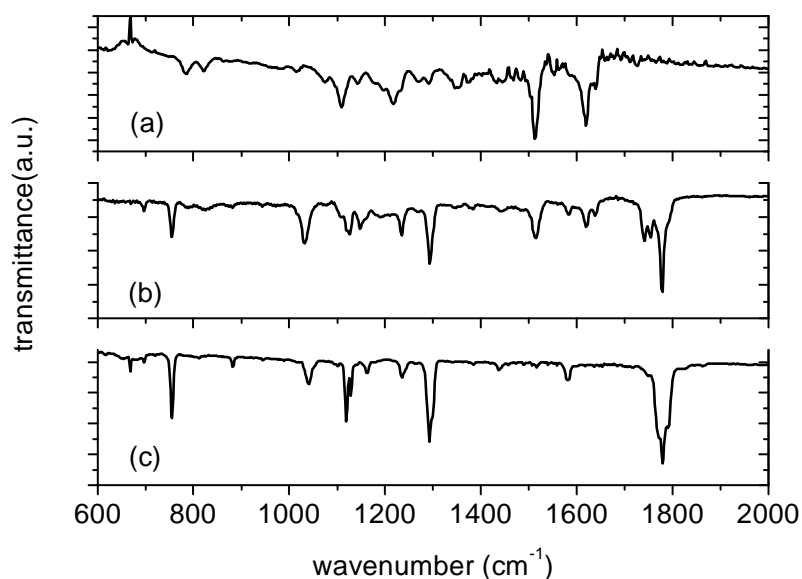


Figure 4.8: FTIR spectra of a pyronin B film (a), a mixed film of NTCDA: pyronin B 1:1 (b) and a NTCDA film (c) made by vacuum sublimation.

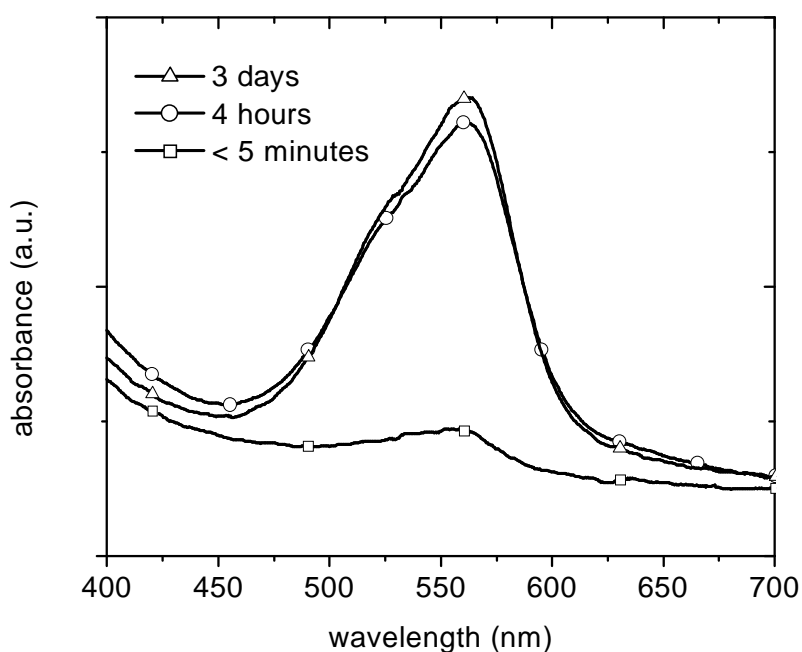


Figure 4.9: VIS absorption spectra of mixed film of NTCDA and pyronin B by coevaporation. Time delay in air: square: shortly (<5 minutes) after break of vacuum; circle: 4 hours; triangle: 3 days.

ability in their ground states. In the conductivity and field effect measurement of NTCDA doped with pyronin B, the electron density increases with the temperature

[27, 28]. This means that deep donor states are formed.

4.4 Conclusions

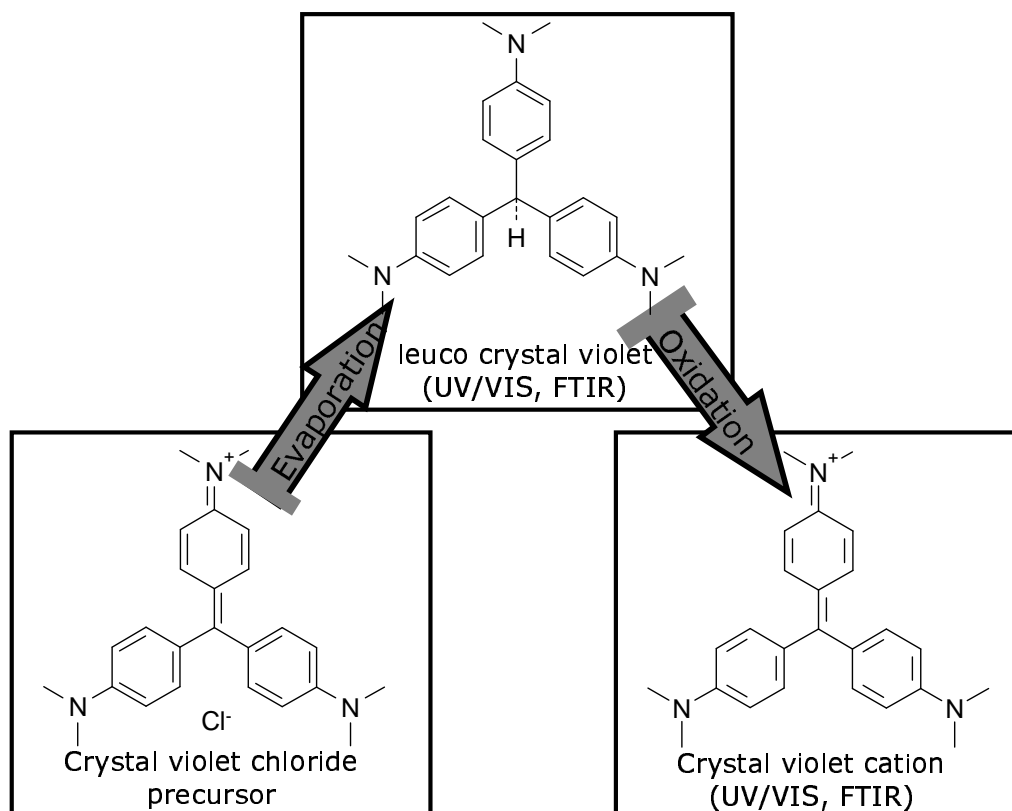


Figure 4.10: Mechanism of donor creation and electron transfer

We have presented detailed investigations on a new approach for n-type doping of organic thin films using cationic dyes as dopants. Cationic dyes can form strong donors in situ by sublimation. Spectroscopic investigations reveal that the leuco bases of cationic dyes are formed in situ during evaporation of xanthenic cationic dyes and triphenylmethane cationic dyes. A conductivity study of organic electron transport materials (with low lying LUMO) doped with the cationic dyes has been carried out. All dopants used in the study give rise to an increase of several orders of magnitude in conductivity with dopant concentration, accompanied by a decrease in activation energy compared to undoped organic thin films. This means that cationic dyes are effective dopants for n-type doping of organic electron transport materials with moderate acceptor strength. From a combined MS, UV/VIS and FTIR spectroscopy study, we identify the colorless reduced forms of the cationic

dyes as the main constituent of vacuum deposited layers. It is clearly observed that the leuco forms are transformed back to the dye cation upon oxidation in air or by a stronger acceptor, TCNQ (see Figure 4.10). Electron transfer between donors and acceptors, accompanied by a hydride transfer leads to an n-type doping effect (Detailed mechanism of charge transfer will be discussed in Chapter 5).

Chapter 5

Leuco crystal violet as a dopant for n-type doping of organic thin films of fullerene C₆₀

In this chapter, leuco crystal violet (LCV) and C₆₀ are used as models of leuco bases of cationic dyes and organic electron transport materials to study the n-type doping effect of leuco bases in organic semiconductors. Having identified LCV as the molecule created by sublimation of CV in Chapter 4, it is straightforward to use LCV itself as a dopant. We aim to prove that LCV is indeed responsible for the donor effect. Fullerene C₆₀ is generally used as an electron acceptor in active and electron transport layers of organic bulk heterojunction solar cells [31, 32, 143]. N-type doping of C₆₀ is an effective way to increase the conductivity and enhance the built-in-potential. This allows to achieve high open circuit voltages V_{oc} and short circuit currents J_{sc} and thus high efficiency [31, 32]. Alkali metals (Na, K, Rb, Cs) are typical electron donors and alkali metal-doped fullerenes have been studied in detail [103, 144]. However, little research on organic molecules as donors for n-type doping of C₆₀ thin films by co-evaporation has been reported so far. The availability of the leuco base of CV, LCV, allows us to test directly the proposed role of the leuco base as an intermediate in the course of n-type doping and to carry out effective molecular doping of C₆₀.

5.1 Electrical properties of C₆₀ doped with LCV

First, we measured the conductivity of C₆₀ doped with LCV as a dopant (Figure 5.1 (a)). The temperature dependence of the conductivity shows similar behavior

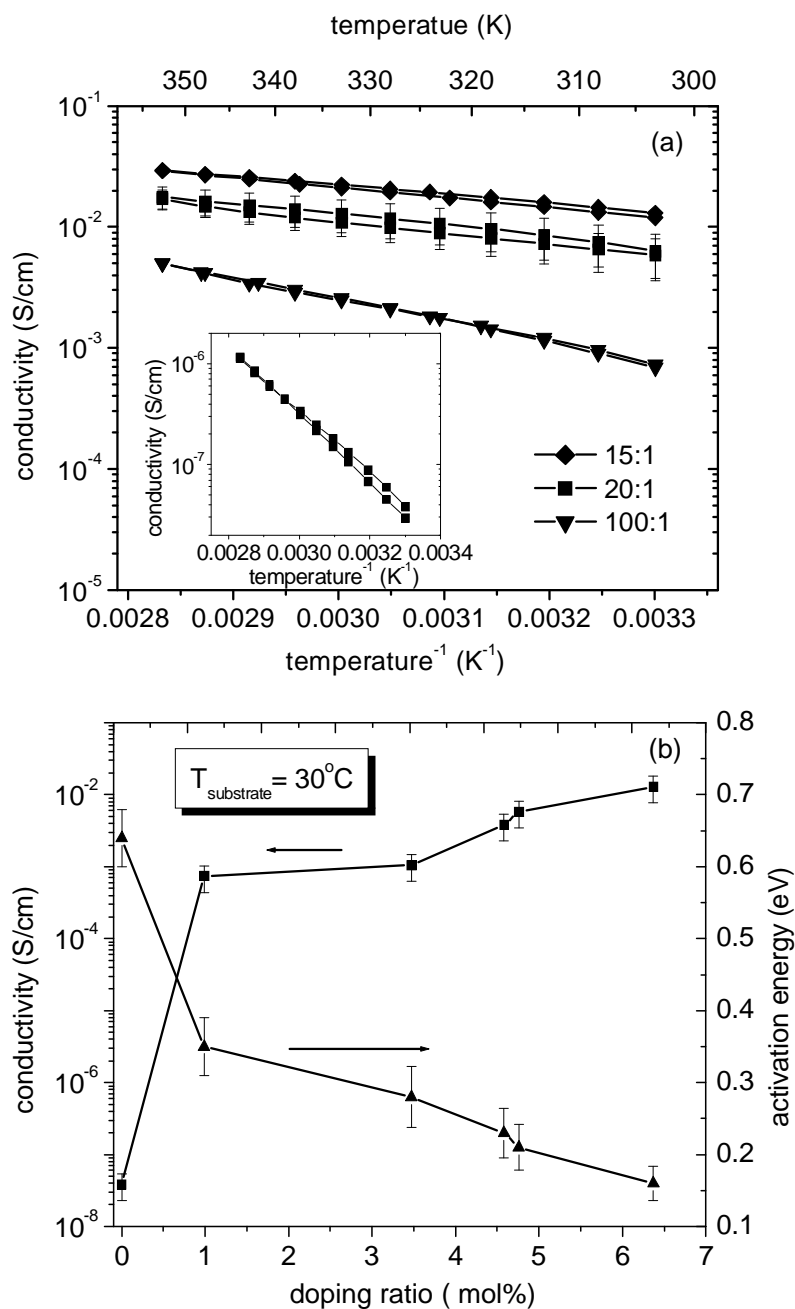


Figure 5.1: Electrical properties of C₆₀ thin films doped with LCV. (a) Conductivity vs. reciprocal temperature for varying molar doping ratio. (b) Conductivity and activation energy vs. doping ratio.

for thin films of LCV-doped C₆₀ and CV-doped C₆₀. Obviously, C₆₀ thin films can be doped with LCV as efficiently as with CV. Even slightly higher conductivity can be achieved because LCV is commercially available at a higher purity (>99%). The highest conductivity reached at 30°C is 1.3×10^{-2} S/cm for a sample with a

molar doping ratio of 15:1 (C_{60} :LCV). For the sample of 20:1, error bars are plotted in Figure 5.1(a). They are deduced from the scattering of conductivity data for a small series of samples grown under nominally identical conditions with the same doping ratio. It is obvious that there is considerable scattering, but all doped samples have conductivities being orders of magnitude above the value for undoped samples. Accordingly, all conclusions on the chemistry of the doping effect drawn in the following are based on significant and reproducible experimental facts. Figure 5.1 (b) shows the conductivity and activation energy versus the molar doping ratio. Once again, the accurate control of the electrical properties by the doping technique is observed.

5.2 Optical spectroscopy

5.2.1 Pure LCV in solid thin film

The electronic absorption of a 80 nm thick LCV thin film prepared by vacuum deposition is shown in Figure 5.2 (c). The electronic absorption spectra of a 20 nm thick CV thin film deposited in vacuum (a) and a coating of LCV prepared by solvent evaporation (b) are also shown to compare with the LCV thin film. In principle, absorption bands of a vacuum deposited thin film of CV (a) are similar to bands in absorption spectrum of LCV coated from methanol solution (b). Their

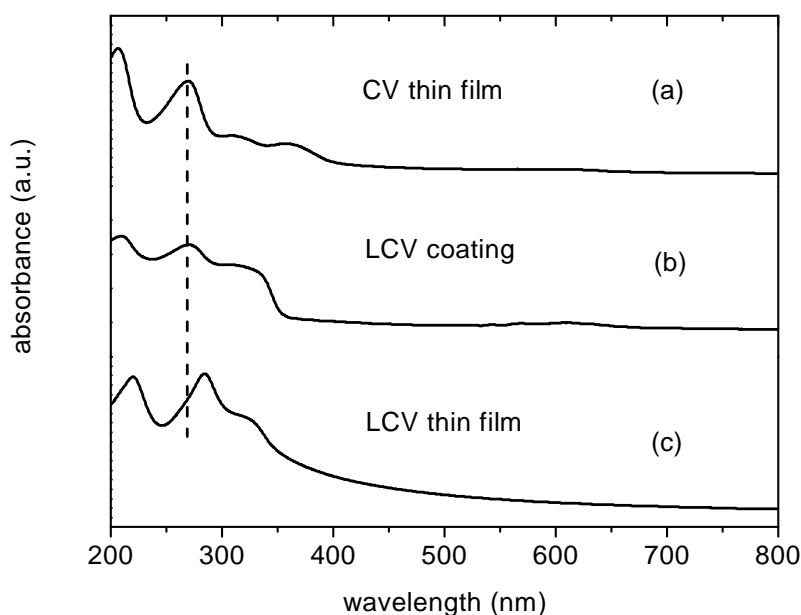


Figure 5.2: Electronic absorption spectra of vacuum deposited films of LCV (c) and CV (a), and an LCV coating (b).

maximum absorption is around 270 nm. However, the maximum absorption peak of a vacuum deposited thin film of LCV is at 283 nm. In order to exclude the effect of condensed state and morphology on the electronic absorption spectra, thin films of evaporated CV and LCV were dissolved in ethanol (see Figure 5.3 (a) and (b)) after the two thin films were exposed to air under daylight for some time. In Figure 5.3 (a), the main absorption bands of evaporated CV are at 574 nm, 355 nm and 257 nm, and a shoulder peak around 300 nm. In Figure 5.3 (b), main absorption bands of evaporated LCV are at 578 nm, 358 nm, 301 nm and 260 nm. In principle, they have similar absorption bands. It means that similar chromophore groups and basic functional groups exist in the two compounds. However, differences of relative height of some peaks are observed in Figure 5.3 (a) and (b), in particular for the peak at 358 nm. It is clear that the absorption band at 358 nm for evaporated CV is much stronger than the peak at 355 nm for evaporated LCV. This is a clue that the quantity of the chromophore group around 358 nm in the two molecules is different, which may be due to their different evaporated temperature. When we compare the above spectra with absorption spectra of pristine CV (Figure 5.3 (c)) and LCV (Figure 5.3 (d)) powder dissolved in ethanol, we can clearly see some small hypsochromic shifts of the bands in the absorption spectra of ethanol solutions of sublimated CV and LCV. In particular, the peak at 589 nm of pristine CV in ethanol is shifted to 578 nm in Figure 5.3 (b) and 574 nm in Figure 5.3 (a). Similar blue

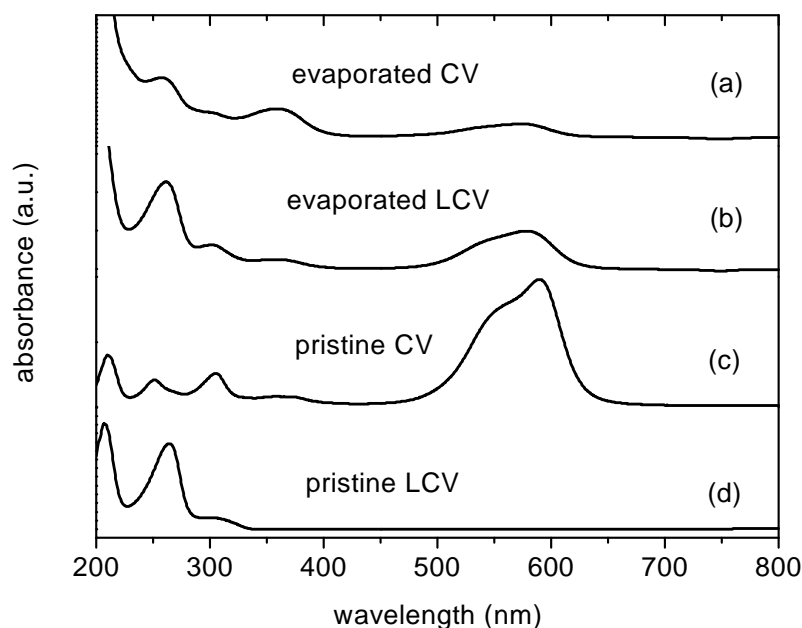


Figure 5.3: Electronic absorption spectra of evaporated CV (a) and LCV (b), and pristine CV (c) and LCV (d) powder in ethanol solution in air.

shifts also took place in the case of evaporated pyronin B and rhodamine B [29]. When the diethylamino groups of rhodamine dyes become stepwise deethylated, there are blue shifts in their absorption spectra [145, 146]. The blue shift observed in our experiment is probably caused by the removal of some methyl groups. The higher sublimation temperature of CV compared to LCV, leading to a removal of more methyl groups, may be one of the reasons why the blue shift of CV (15 nm) is stronger than for LCV (11 nm). On the other hand, the peak at 265 nm in Figure 5.3 (d) from pristine LCV in ethanol shifts to 257 nm in Figure 5.3 (a) and to 261 nm in Figure 5.3 (b). It should be noted that peaks at 574 and 578 nm in Figure 5.3 (a) and (b) result from the photo-oxidized products of evaporated CV and LCV thin films exposed to air under daylight.

5.2.2 Mixed films of TCNQ:LCV

In order to further examine the doping process of LCV in a molecular matrix, we investigated the charge transfer between LCV and electron acceptors by optical spectroscopy. When LCV is used as a dopant, it is oxidized by the matrix molecules, providing free electrons. We investigated mixed films of LCV and TCNQ, a strong organic acceptor, made by co-evaporation (doping ratio 1:1). Electronic absorption and FTIR transmission spectra of freshly mixed films were measured immediately after breaking the vacuum. The electronic absorption of the sample in the VIS/NIR

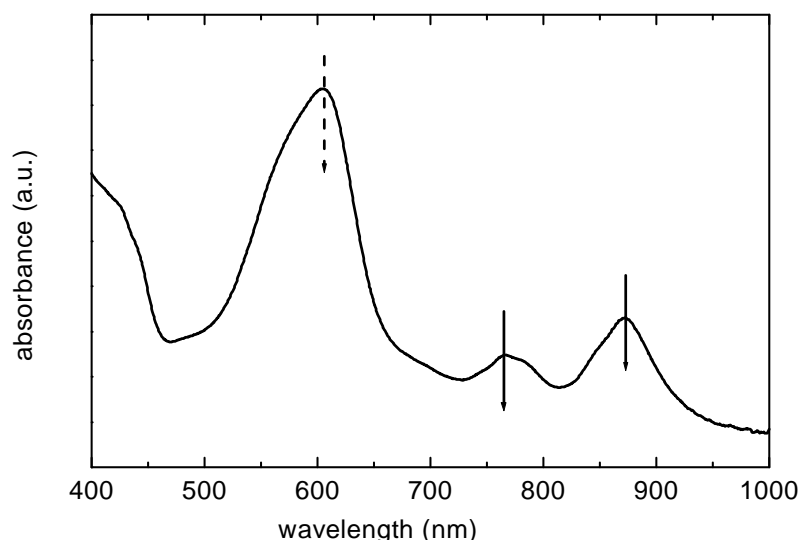


Figure 5.4: Electronic absorption spectrum of a mixed layer of TCNQ and LCV (1:1). The dashed arrow marks the absorption band of CV (606 nm); The solid arrows mark absorption bands of the TCNQ anion. Note: LCV and TCNQ have no absorption bands in the visible range.

range from 400 to 1000 nm is shown in Figure 5.4. The peak at about 606 nm corresponding to the CV cation is clearly seen, confirming an immediate oxidation of LCV in the TCNQ matrix. The peaks at 871 nm and 764 nm, and the shoulder peak at about 780 nm are assigned to the TCNQ anion [141]. The absorption bands of the TCNQ anion between 600 nm and 700 nm can not be observed because they are covered by the stronger absorption of CV. The CV cation peaks and the TCNQ anion radical peaks prove that charge transfer took place in the mixed film. As

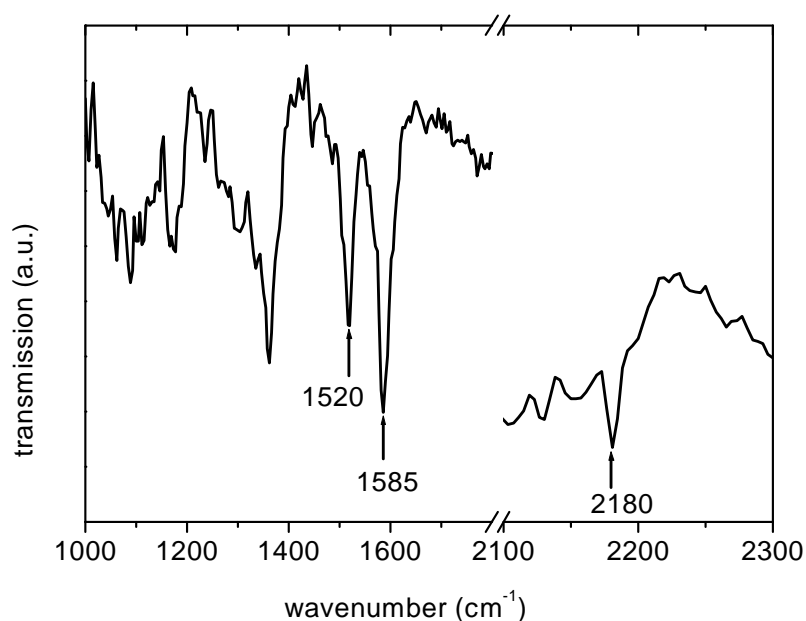


Figure 5.5: FTIR spectra of a mixed layer of TCNQ and LCV (1:1). Solid arrows mark transmission peaks at 1520, 1585 and 2180 cm^{-1} , corresponding to LCV, CV⁺ and TCNQ⁻, respectively.

described in Section 4.3.2, the degree of charge transfer between LCV and TCNQ can be determined from FTIR transmission measurements. In Figure 5.5, only a peak at 2180 cm^{-1} assigned to TCNQ⁻ is observed between 2100 cm^{-1} and 2300 cm^{-1} . There is no sign of neutral TCNQ (2227 cm^{-1}) in the spectral range of the nitrile stretching mode. Obviously, one electron is transferred to TCNQ from LCV according to Ref. [133]. Peaks at 1520 cm^{-1} corresponding to the N-ring mode in neutral LCV and at 1585 cm^{-1} corresponding to the N-ring mode in cationic CV are both visible, but the intensity of the peak at 1585 cm^{-1} is higher. This shows that most of the LCV is oxidized to CV. However, a small amount of LCV still exists in the mixture. The reason could be a slight deviation from the intended 1:1 ratio of the involved compounds. As it is obvious from above, LCV not only donates an electron to the matrix, but also releases a hydrogen. In the reactions

between LCV and TCNQ, we assume that the electron transfer may be accompanied by a hydride transfer reaction [147, 148]. In fact, an electron transfer pathway followed by proton transfer has been established for hydride transfer reactions from 4-(dimethylamino)phenyl methane derivatives, for example LCV, to 2,3-dichloro-5,6-dicyano-p-benzoquinone (DDQ) [149]. Thus, the oxidation of LCV by TCNQ is achieved by hydride abstraction. When TCNQ gets hydrogen atoms, TCNQ can be reduced to p-phenylenedimalononitrile (TCNQH₂) [150]. In this mechanism, the overall reaction stoichiometry is assumed as



5.2.3 Mixed films of C₆₀:LCV

Now, the question arises if similar charge transfer reactions can also be observed in mixed layers of LCV and C₆₀, with C₆₀ having a much lower electron affinity than TCNQ. Konarev et al. [151] have demonstrated intermolecular charge transfer (CT) from LCV to the C₆₀ molecule in molecular complexes (LCV · C₆₀ · C₆H₅Cl) on photo excitation by white light (light induced ESR (LESR) spectroscopy), but no CT took place in the ground state.

Therefore, we studied the effect of illumination by a halogen lamp during the layer growth on the conductivity of LCV-doped C₆₀ layers. We found that the sample reached its steady state conductivity soon after evaporation and prolonged heating for stabilization was no longer necessary. Obviously, an irreversible charge transfer between C₆₀ and LCV can be induced by light. Then, optical spectroscopic measurements were carried out to study the charge transfer between C₆₀ and leuco bases of cationic dyes. It is known that the C₆₀ radical anion is sensitive to oxygen to form C₆₀ [152, 153]. In order to check the presence of a low concentration of C₆₀ anions in mixed films, samples must be protected against air.

Figure 5.6 (b) shows the FTIR transmission spectrum of a mixed film of C₆₀ and LCV (molar ratio 5:1) encapsulated in a glove box under nitrogen atmosphere. The FTIR spectra of pure vacuum-deposited C₆₀ thin film (a) and a pure LCV coating from methanol solution (b) are also shown in Figure 5.6 as references. A 17 W halogen lamp was used to provide a diffuse illumination in the chamber during the growth of mixed layers by vacuum-deposition. The light intensity at the position of the sample as measured by a silicon photodiode was 4×10^{-3} mW/cm². The mixed film was illuminated by a 1064 nm laser with the intensity of 500 mW/cm² before its FTIR transmission spectrum was measured. In Figure 5.6 (b), two out of four F_{1u} modes of the C₆₀ molecule, which are IR active at 1429 cm⁻¹ [F_{1u} (4)] and 1183

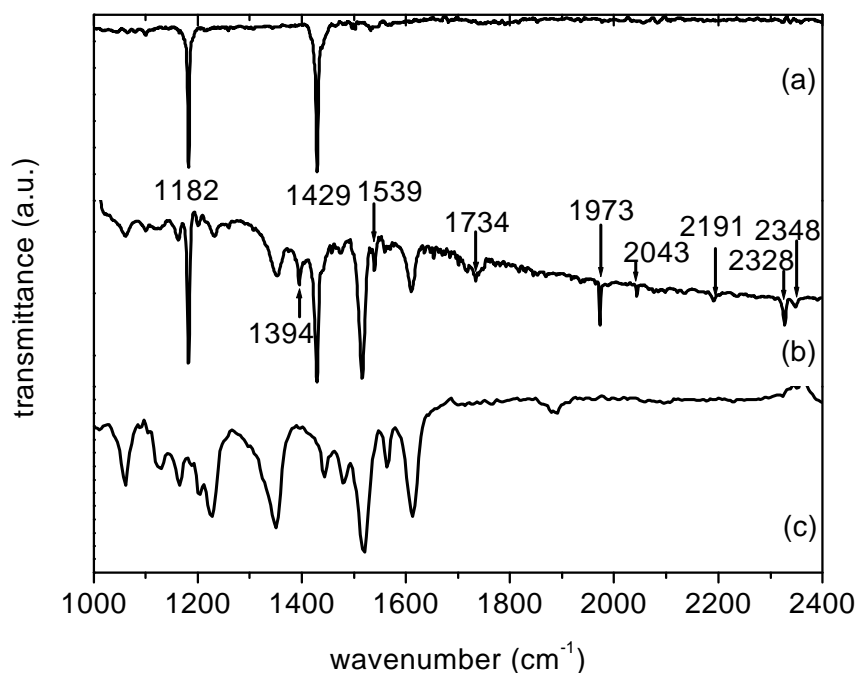


Figure 5.6: FTIR spectra of (a) pure vacuum-deposited C₆₀ thin film, (b) a mixed layer of C₆₀:LCV (5:1) prepared by coevaporation and (c) a pure LCV coating. A 17 W halogen lamp was used to provide diffuse illumination in the chamber during the growth of mixed layers by vacuum-deposition. The light intensity at the position of the sample as measured by a silicon photodiode was 4×10^{-3} mW/cm². The C₆₀:LCV (5:1) sample was encapsulated in a nitrogen atmosphere and illuminated by laser (1064 nm) with light intensity of 500 mW/cm² before the FTIR measurement.

cm⁻¹ [F_{1u} (3)] [112], are clearly observed in the spectral range from 1000 to 2400 cm⁻¹. A weak peak around 1394 cm⁻¹ marked by an arrow can be observed and is assigned to the C₆₀ anion [154, 155]. Charge transfer to C₆₀ leads to linear frequency changes versus the degree of charge transfer for two [F_{1u} (2) and F_{1u} (4)] IR active modes of C₆₀ at 576 and 1429 cm⁻¹, respectively [136]. The IR measurements of C₆₀ doped by alkali metals, and anion radical salts of C₆₀ show that the frequency changes for the F_{1u} (4) mode are maximal. Its frequency shifts from 1429 cm⁻¹ for neutral C₆₀ to 1390-1394 cm⁻¹ for the radical anion C₆₀⁻ [155]. Accordingly, we can conclude that at least a fraction of the C₆₀ molecules obtain one electron from LCV in the mixed thin films to form C₆₀⁻. When the FTIR transmission of the 1:1 sample is measured after exposure to air for a short time (2 - 3 minutes, see spectrum marked by stars and dotted line in Figure 5.7), the peak at 1394 cm⁻¹ is nearly absent. The spectrum marked by circles and solid line before the sample was exposed to air is also shown here as a guide for the eyes. We consider this finding

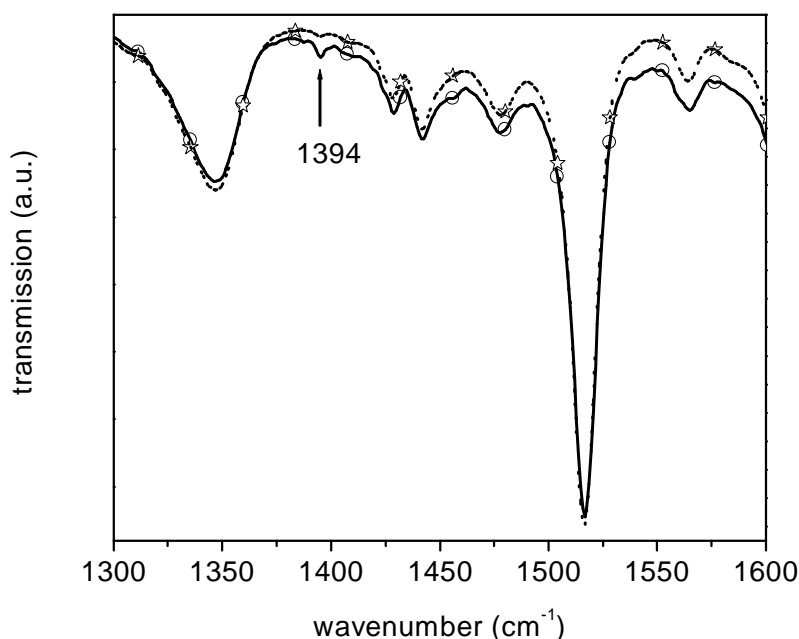


Figure 5.7: FTIR spectra of a mixed film of C_{60} and LCV (1:1) exposed to air for a short time (2-3 minutes) and protected against air. The spectrum is marked by stars and dotted line after exposure to air and marked by circles and solid line before exposure to air.

as a further evidence for the formation of C_{60} anions in mixed films because C_{60} anion is sensitive to air. A similar phenomenon is also observed in a further sample of codeposited C_{60} and LCV with the molar ratio 3:1.

Two dominant peaks of LCV around 1517 and 1612 cm^{-1} are obviously visible in Figure 5.6. The peak at about 1585 cm^{-1} assigned to the CV cation cannot be found in the mixed layer of C_{60} and LCV. The broad peak at 1612 cm^{-1} and the peak at 1565 cm^{-1} could mask a very weak peak at 1585 cm^{-1} . Unfortunately, we can not use UV/VIS/NIR absorption spectroscopy (see the inset in Figure 5.8) to identify the existence of CV cation (606 nm) because the absorption of C_{60} between 400 nm and 800 nm masks the faint absorption from a low concentration of CV cations. However, Figure 5.8 provides direct information on the presence of C_{60} anion. Figure 5.8 shows the NIR absorption spectrum of a 3:1 (C_{60} :LCV) mixed film illuminated during evaporation and encapsulated under nitrogen atmosphere after the sample had been illuminated for 22 hours in a vacuum desiccator. The peak around 1055 nm is attributed to the C_{60} anion [152, 155, 156, 157].

Having identified C_{60} anions in the mixed layers of C_{60} and LCV, we come back to a more detailed discussion of the FTIR spectrum of the mixed layer shown in Figure 5.6 (b). Besides the peak at 1394 cm^{-1} , we also can find other new peaks at 1539 ,

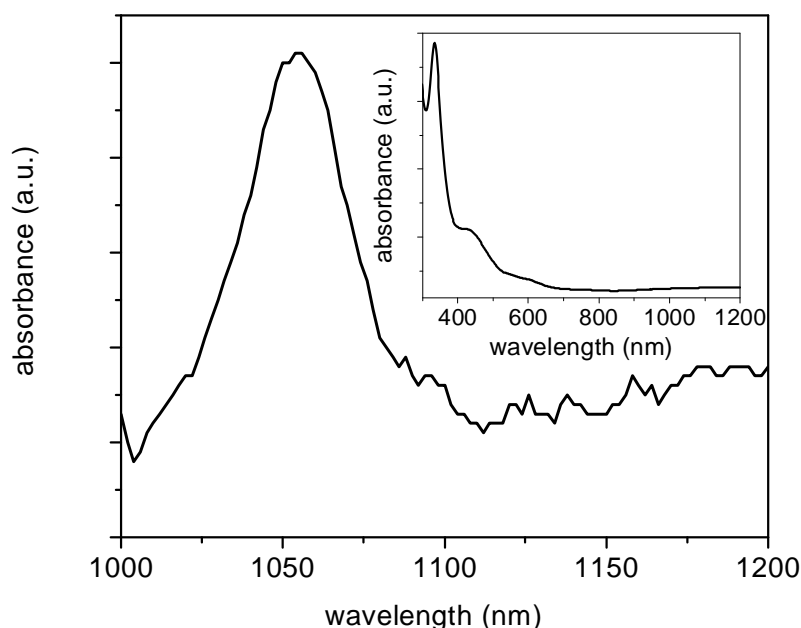


Figure 5.8: NIR electronic absorption spectrum of a mixed film of C₆₀ and LCV (3:1). The inset shows an UV/VIS/NIR (300 - 1200 nm) electronic absorption spectrum of the sample. The sample was grown under the same condition as the sample of Figure 5.6. The sample was encapsulated in a nitrogen atmosphere and then illuminated by a 17 W halogen lamp (light intensity of 15 mW/cm²) for 22 hours in a vacuum desiccator before measurements.

1734, 1973, 2043, 2191, 2328, and 2348 cm⁻¹. These peaks are mainly associated with bands of the broken icosahedral, I_h symmetry of the fullerenes. Molecular dopants lower the molecular symmetry of fullerenes, and lead to the activation of many silent modes and the appearance of a great number of higher order combination modes in the crystal in the IR spectrum. The peak at 1539 cm⁻¹ is associated with the *h_u* mode of C₆₀ [158, 159, 160]. Peaks at 1973, 2043, 2191, 2328 and 2348 cm⁻¹ have been observed in the infrared transmission of silent and higher order vibrations in C₆₀ crystals [159, 160]. As to the peak at 1734 cm⁻¹, we assume that it comes from the multiphonon contribution from *h_g* mode of C₆₀⁻ according to Ref.[161]. As pointed out by Wang et al. [161], the IR absorption of C₆₀ anions shows a multiphonon structure. The Jahn-Teller active *h_g* modes are predicted to be observable in the IR spectrum of C₆₀⁻. The peak at 1734 cm⁻¹ only has 1.7% error compared with 1764 cm⁻¹ calculated by Wang et al. [161]. Normally, such an error between experiment and calculation is considered acceptable. Assignments of these peaks related with fullerene C₆₀ and C₆₀ anions are shown in Table 5.1.

In the IR spectra of C₆₀H₃₆ reported by other authors [162, 163], a peak around

Table 5.1: All peaks related with the C_{60} and C_{60}^- anion in Figure 5.6 and their assignments.

Peak	Assignment	Ref.
1183	F_{1u} (3)	[131], [132], [135], [136]
1429	F_{1u} (4)	[131], [132], [135], [136]
1539	F_{1g} (2) + H_u (2)	[135], [136]
1973	F_{2u} (4) + H_g (4)	[135]
2043	F_{2g} (3) + H_u (4)	[136]
2191	G_g (3) + H_u (6)	[135]
2328	G_g (5) + G_u (4)	[135], [136]
2348	G_u (3) + H_g (7)	[135], [136]
1394	F_{1u} (4)	[131], [132]
1734	Jahn-Teller active H_g	[137]

1735 cm^{-1} has been observed. In order to confirm the existence of hydrogenated C_{60} , the FTIR spectrum of the 5:1 sample from Figure 5.6 in the region of the C-H stretching vibrations (2750 - 3000 cm^{-1}) is plotted in Figure 5.9 (a). The FTIR spectrum of a pure LCV coating is plotted in Figure 5.9 (b) as a reference. In Figure 5.9 (a), peaks at 2794 and 2876 cm^{-1} can be assigned to C-H stretching vibrations of LCV, and peaks at 2829, 2850 and 2911 cm^{-1} are in agreement with C-H stretching vibration of $C_{60}H_{36}$ reported in literature [162, 163, 164]. It is known that fullerenes have unusual hydrogen-sorbing properties [165]. C_{60} in the mixture with LCV under illumination is able to accept H^+ or H_2 with high reaction activity from LCV to $C_{60}H_X$. From the FTIR data, it is possible that hydrofullerenes $C_{60}H_X$ and $CV^+C_{60}^-$ are products of a photoinduced redox reaction between C_{60} and LCV. If $C_{60}H_2$ is one of the products in the above reaction, it is also an electron acceptor with four electron transfer steps ($E_{1/2} = -1.02, -1.46, -2.07, -2.58$ V vs. Fc/Fc^+) [166]. Since all reductions of $C_{60}H_2$ are shifted to more negative potentials than those of C_{60} ($E_{1/2} = -0.98, -1.37, -1.87, -2.35, -2.85$ and -3.26 V vs. Fc/Fc^+ [106]) and only four electron-transfer processes, it is a weaker acceptor than C_{60} . A small quantity of $C_{60}H_2$ as an antitrap for electrons has minor influence on the electrical properties of C_{60} thin films doped with LCV.

$CV^+C_{60}^-$ has been synthesized as a reddish brown crystalline product [156, 167]. Kitagawa et al. [168] demonstrated the presence of CV^+ and C_{60}^- in 1:1 ratio and that the formation of a carbon-carbon covalent bond was prevented by the high

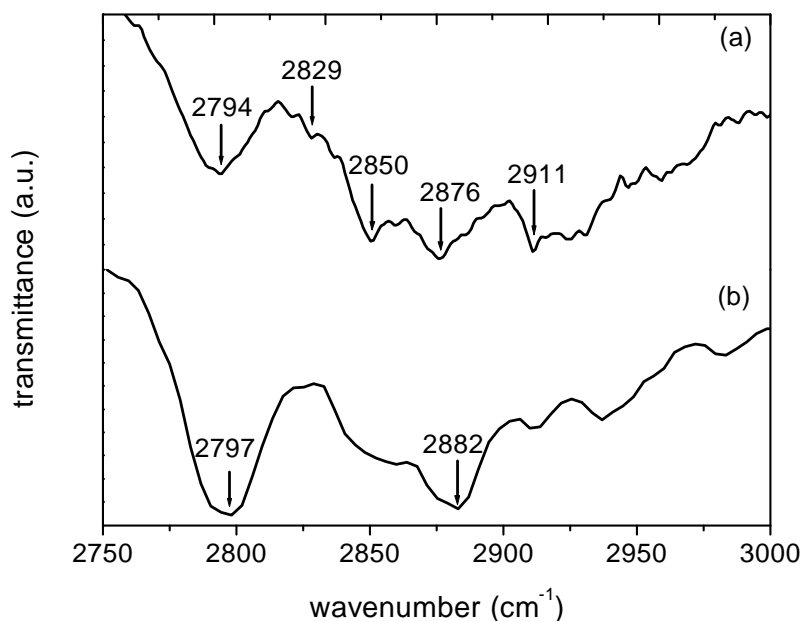


Figure 5.9: FTIR spectra of sample 5:1 illuminated by laser with the intensity of 500 mW/cm² and pure LCV coating in the region of the C-H stretching vibrations (2750-3000 cm⁻¹).

stability of the CV cation as well as repulsion between the aromatic rings of CV⁺ and the C₆₀ cage. In our case, when LCV donates one electron and one proton to the acceptor C₆₀, C₆₀ anions and CV cations thus coexist in the mixed films of C₆₀ and LCV. Unfortunately, we could not find any direct evidence for the formation of CV by hydride abstraction from LCV after charge transfer. However, we conclude from the fact that the doping effect requires some heating or illumination, that there is hardly a charge transfer between LCV and C₆₀ in the ground state. We are rather dealing with a charge transfer that requires activation by heat or light followed by a decomposition of the LCV⁺ radical, probably to CV⁺, that makes the charge transfer irreversible.

5.3 Electrochemistry of LCV and CV

Electrochemistry is a convenient method to study reactions involving electron transfer. To understand the redox process of LCV, electrochemical properties of LCV (a) and CV (b) are studied using cyclic voltammetry, as shown in Figure 5.10. In Figure 5.10 (a), LCV has a strong irreversible oxidation peak around 0.79 V vs. SCE and a pair of weak reversible redox peaks toward negative direction. Because of trace water, a peak is observed at -0.43 V vs. SCE. The important information is that the

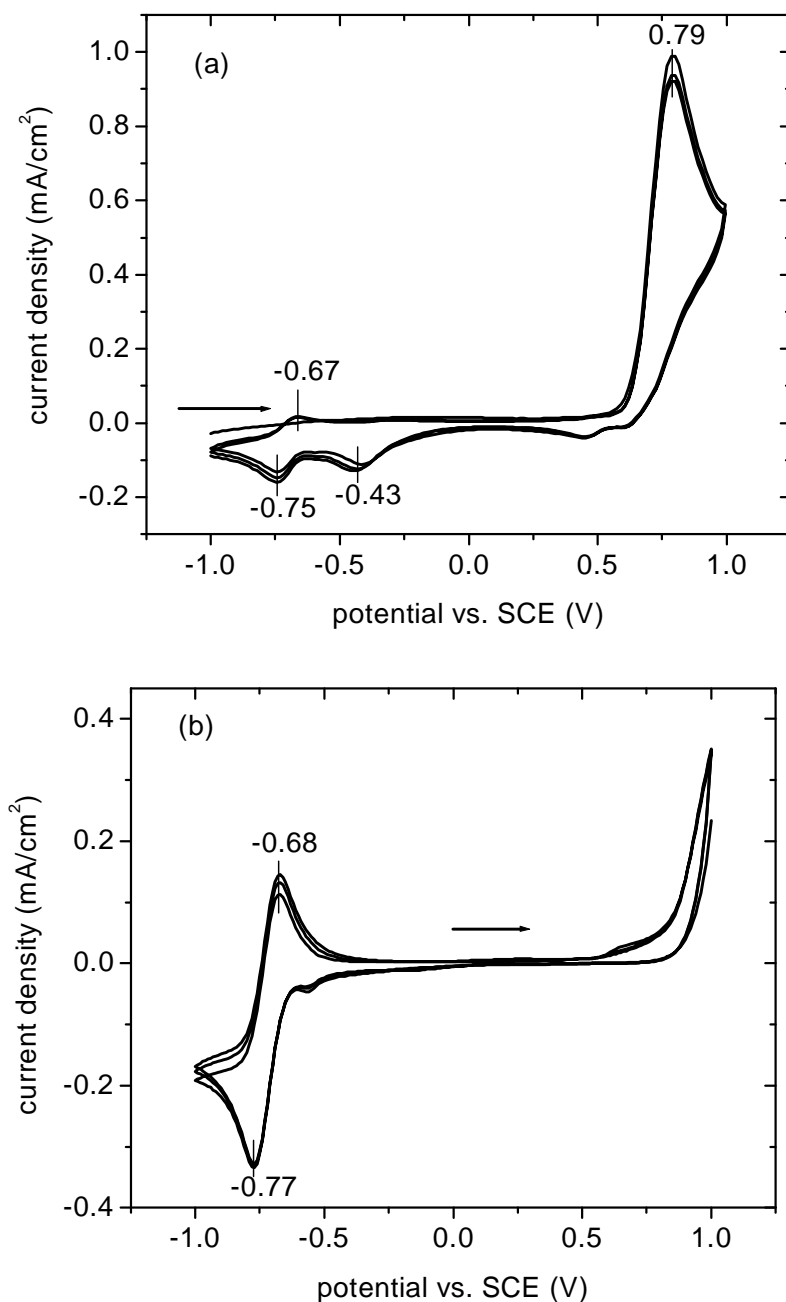


Figure 5.10: Cyclic voltammograms of (a) LCV, scan rate 100 mV/s and (b) CV, scan rate 20 mV/s in acetonitrile containing 0.1M Bu₄NBF₄ under Argon atmosphere. A saturated calomel electrode (SCE) is used as the reference electrode.

positions of the redox peaks are similar to the reversible redox peaks of CV shown in Figure 5.10 (b). The results suggest that the LCV cation radical is unstable and quickly becomes a stable CV cation by a hydride transfer in its oxidation process. We also found that the color of the solution immediately changed from colorless to

violet when the scan reached about 0.8 V vs. SCE. Then, the color of the solution was violet and did not return the colorless during the experiments. So, CV is the oxidized state of LCV. In the same way, CV⁺ should also be the product of LCV when it is photo-oxidized by C₆₀.

5.4 Mechanism of photoinduced electron transfer from LCV to C₆₀

The process of light-induced electron transfer between LCV and C₆₀ is illustrated in Scheme 5.2. When LCV is excited by light, an electron is lifted from the HOMO to the LUMO. Subsequently, this electron leaps to the lower-lying LUMO of the adjacent C₆₀ (Scheme 5.2(a)) to reach an energetically more favorable state. In this way, two radical ions, LCV⁺ and C₆₀⁻, are formed (Scheme 5.2(b)). Now, the radical electron in the LUMO of C₆₀ could return to the HOMO of LCV which would not correspond to a permanent doping process. However, at this stage there is obviously a competing, non-reversible reaction channel, namely a hydride transfer reaction of LCV⁺ to C₆₀. By this hydride transfer, the unstable LCV radical cation with a half-filled HOMO is transformed into the stable, non-radical CV cation with fully occupied HOMO (Scheme 5.2(c)), i.e. back transfer of the electron on C₆₀ is no longer possible and we have a permanent doping effect with an enhanced equilibrium electron density on C₆₀. Such transfer reactions have been observed before when LCV meets stronger oxidants such as DDQ or TCNQ. Here, LCV can be oxidized directly to a CV cation by the hydride transfer accompanied by electron transfer [147, 148, 149]. For weaker acceptors like C₆₀, the combined hydride and electron transfer reaction obviously has to be supported by external activation (light or heating). When C₆₀ accept hydrogen atoms or radicals, it can be reduced to hydrofullerene. To clearly explain the photoinduced charge transfer between C₆₀ and LCV, we divide the process into two parts as shown in Scheme 5.2. In fact, hydride transfer and electron transfer could take place at the same time.

5.5 Conclusions

We have shown that fullerene C₆₀ can be effectively doped with LCV by the co-evaporation technique. An increase of six orders of magnitude in conductivity of doped C₆₀ has been achieved, compared to undoped C₆₀. LCV gives a similar doping effect in C₆₀ to CV. Electron transfer from LCV to the matrices gives rise to n-type doping. For TCNQ:LCV blend layers, TCNQ anions and CV cations are clearly

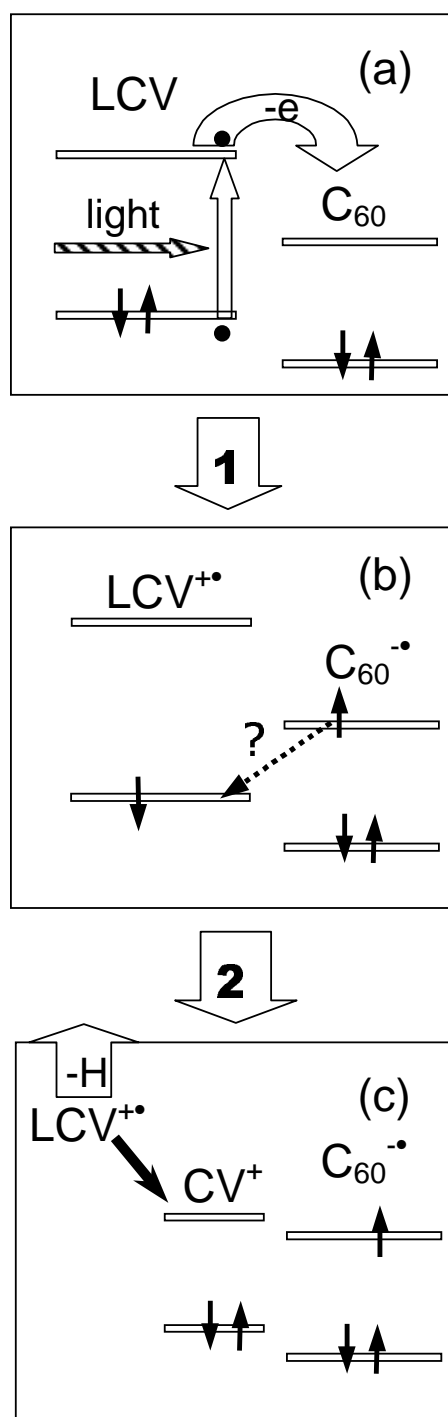


Figure 5.11: Photoinduced charge transfer from LCV to C₆₀. Note: The solid circle at the LUMO or the HOMO marked in (a) is only a substitute of active electron imagined to describe electron transfer process visually. The arrows are real electrons occupying the LUMO and the HOMO of molecules.

observed in UV/VIS/NIR absorption and FTIR spectra. One electron transfer from LCV to TCNQ takes place. For C₆₀ doped with LCV, C₆₀⁻ is present in NIR absorption and FTIR spectra. For weaker acceptors like C₆₀, the combined hydride and electron transfer reaction obviously has to be supported by outer activation (light or heating). When C₆₀ accept hydrogen atoms or radicals, it can be reduced to hydrofullerene. An irreversible electron transfer reaction leads to a stable n-doping effect in organic thin film of C₆₀ doped with LCV.

Chapter 6

Acridine orange base as a dopant for n-type doping of organic thin films of fullerene C₆₀

The cationic dye acridine orange has a lower reduction potential than pyronin B [122]. Accordingly, one expects that it could provide a more powerful dopant than pyronin B. In this chapter, acridine orange (AO, Figure 3.3) and acridine orange base (AOB, Figure 3.10) are used as dopants for n-doping of thin films of C₆₀. Conductivity, field effect and Seebeck measurements are carried out to characterize the doping effect and type of conductance. Combined FTIR and NIR spectra suggest charge transfer between AOB and C₆₀, leading to an increase in n-type conductivity of C₆₀ thin films.

6.1 Electrical properties of thin films of C₆₀ doped with acridine orange base

6.1.1 Conductivity

When acridine orange (AO) is used as a dopant for n-type doping of C₆₀ thin films, slightly higher conductivities are obtained than in the case of CV or LCV as dopants in C₆₀. The conductivity versus the reciprocal temperature for C₆₀ doped with AO is plotted in Figure 6.1(a). A thermally activated behavior can be found in the measured temperature range like for the thin films doped with xanthene and triphenylmethane dyes in our study. Moreover, the influence of the dopant concentration is also clearly visible. The highest conductivity of 6.5×10^{-2} S/cm at 30°C was achieved for a molar doping ratio of 11:1 (C₆₀:AO). For samples with slightly higher doping ratio, no obvious decrease in conductivity is observed in our experiments.

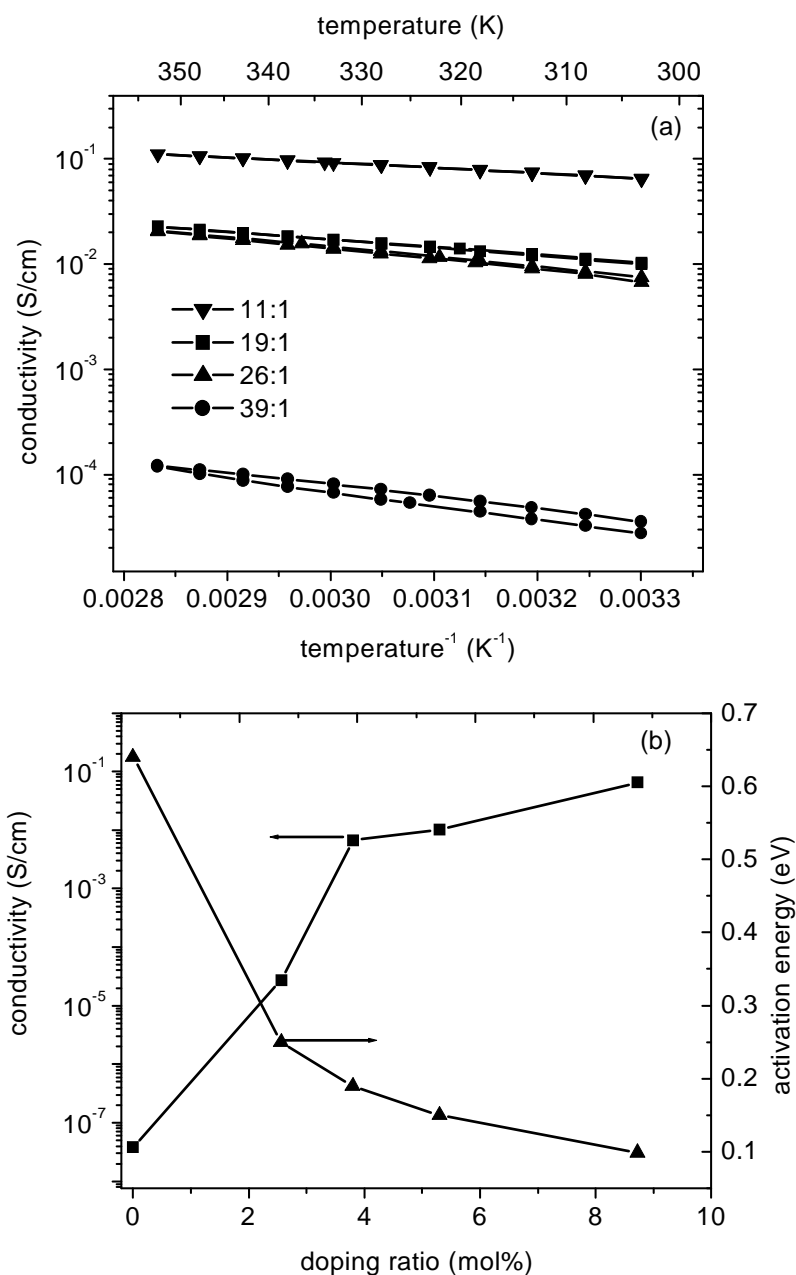


Figure 6.1: Electrical properties of C₆₀ thin films doped with AO. (a) Conductivity vs. reciprocal temperature for varying molar doping ratio. (b) Conductivity and activation energy vs. doping ratio.

However, because high dopant concentrations damage the crystalline order of the matrix, we speculate that conductivities could fall for samples with too high doping ratios. Figure 6.1 (b) shows the conductivity and activation energy versus the molar doping ratio. With increasing dopant concentration, a systematic increase of more

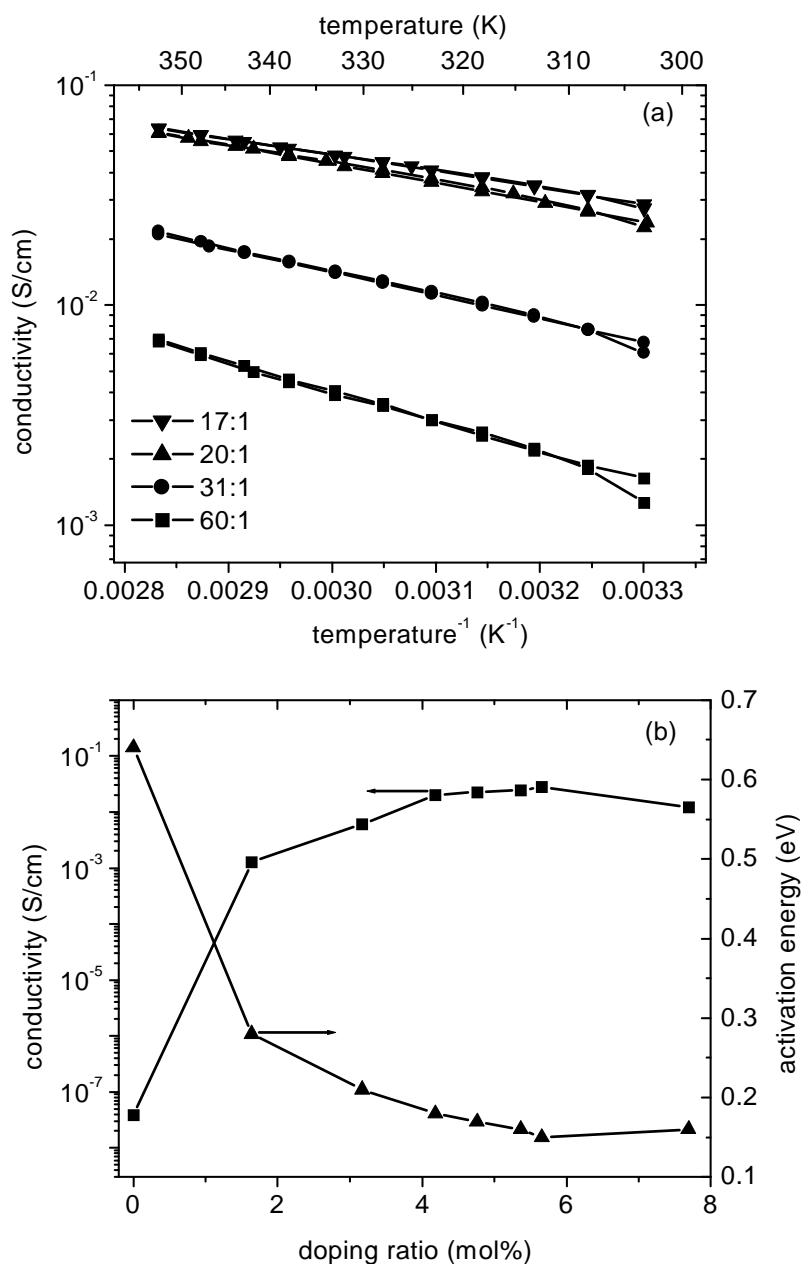


Figure 6.2: Electrical properties of C_{60} thin films doped with AOB. (a) Conductivity vs. reciprocal temperature for varying molar doping ratio. (b) Conductivity and activation energy vs. doping ratio.

than 6 orders of magnitude in conductivity is observed, accompanied by a decrease in activation energy from 0.64 eV to 0.1 eV compared to undoped C_{60} . When the samples are exposed to air, the conductivity falls quickly.

For comparison, we then tried acridine orange base (AOB) as a n-type dopant in C_{60} . A doping effect similar to AO is achieved as shown in Figure 6.2. The highest

conductivity at 30°C reaches 3×10^{-2} S/cm for a sample with a molar doping ratio of 17:1 (C₆₀:AOB) and an activation energy of 0.15 eV. In the case of LCV as a dopant in C₆₀ described in Chapter 5, we have shown that the maximum conductivity (1.3×10^{-2} S/cm) is achieved in a sample with doping ratio 15:1 (C₆₀:LCV), having an activation energy of 0.16 eV. Seemingly, AOB and LCV have nearly the same doping effect for C₆₀ as the matrix after samples reached their steady states.

However, we also found some differences between the two dopants. When AOB is used as a dopant, the conductivity of doped C₆₀ films prepared in the dark increases gradually during coevaporation and reaches nearly 10^{-5} S/cm immediately after coevaporation for the sample with doping ratio about 5 mol%. After a few cycles of heating and cooling, samples reach their steady states. However, when LCV is doped into C₆₀ in the absence of light, the conductivity is very low after coevaporation. Steady states of samples can not be reached until prolonged annealing for long time is completed. It seems that a redox reaction between AOB and C₆₀ takes place more easily compared to LCV, though their final doping effect is similar after annealing.

For all samples shown in Figure 6.1 and Figure 6.2, no diffuse illumination in the chamber is provided during the growth of mixed layers by vacuum-deposition. Only ambient daylight enters the chamber through the view window. In order to study the effect of light and heating on conductivity, we carried out the following experiments. Figure 6.3 records changes in conductivities of three samples with similar doping ratio (5.6 mol%) under different experimental conditions. When a diffuse illumination is provided by a 17 W halogen lamp through the window of the chamber during coevaporation and measurement, the conductivity of the sample (squares in Figure 6.3) at 30°C reaches 4.9×10^{-2} S/cm and an activation energy 0.11 eV just after evaporation. The data for the heating and cooling cycle from 30°C to 70 °C are nearly coincident. After 3 cycles of heating and cooling and 13 hours illumination by 17 W halogen lamp outside the window of chamber, no further changes are observed in conductivity and activation energy. But when the sample is prepared and measured in the dark (circles in Figure 6.3), the conductivity at 60°C is in the range of 10^{-6} S/cm just after evaporation (solid circles). After 6 cycles of heating and cooling from 30°C to 80°C, the sample basically reaches its steady state (hollow circles). The final conductivity is 8.5×10^{-4} S/cm at 30°C and the activation energy 0.21 eV. When weaker light is provided by the hot cathode pressure gauge turned on in the vacuum chamber during evaporation and measurement (stars in Figure 6.3), the conductivity is 8.7×10^{-3} S/cm at 35°C just after evaporation (solid stars). Its steady state is reached after 3 cycles of heating and cooling (hollow stars). The final conductivity is similar to the sample illuminated by much stronger light from 17 W

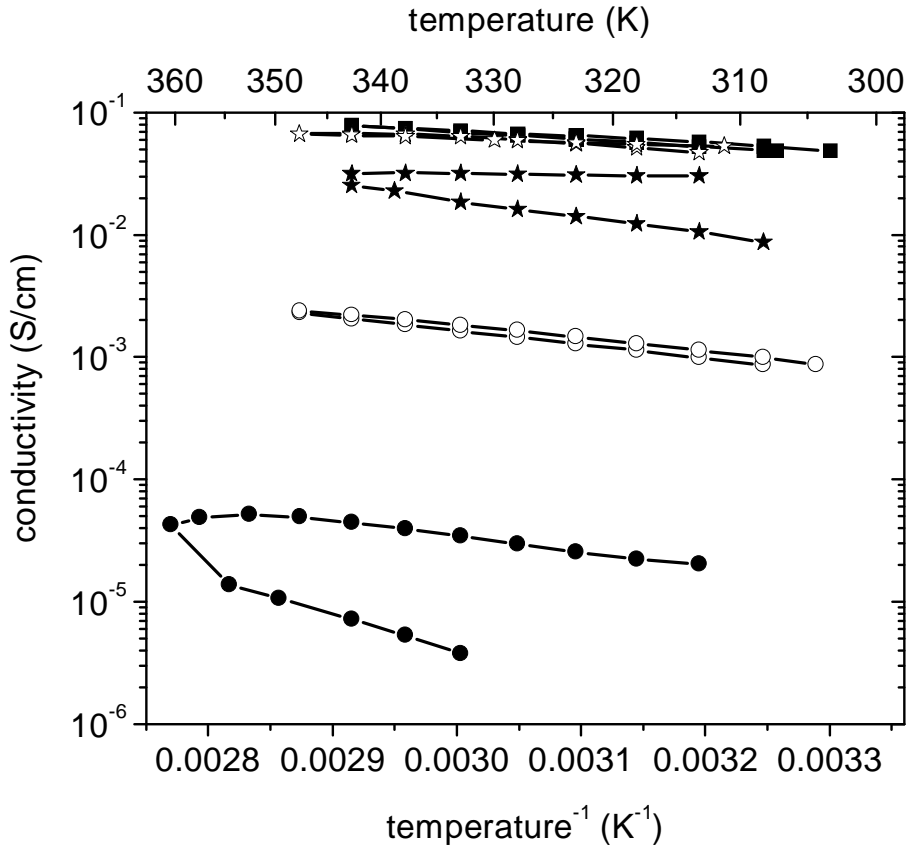


Figure 6.3: Light and heating effect on conductivity of C₆₀ thin films doped with AOB. Sample 100:6.00 (C₆₀:AOB) in the completely dark condition during evaporation and measurement is marked by circles (solid circles for the first annealing, hollow circles for the sixth annealing of the sample with $E_{act}=0.21$ eV). Sample 100:5.83 (C₆₀:AOB) under weak light from the pressure sensor during evaporation and measurement is marked by stars, solid stars for the first annealing and hollow stars for the third annealing of the sample with $E_{act}=0.08$ eV. Sample 100:5.84 (C₆₀:AOB) under the stronger light from 17W halogen and light from pressure sensor during evaporation and measurement is marked by squares, solid squares for the first annealing with $E_{act}=0.11$ eV. Further heating and cooling circle of the sample can not increase conductivity and decrease activation energy.

halogen lamp. From the above phenomena, we can conclude beyond doubt that external light and heating can increase conductivity. However, light is more effective, i. e. the final conductivity induced by annealing is lower than the conductivity that can be reached by light treatment.

In order to prove AOB as a dopant to be universal, other organic acceptor materials such as F₁₆ZnPc, NTCDA and TCNQ have also been doped. Table 6.1 gives conductivity and activation energy results for doped thin film. An obvious increase

in conductivity of doped matrices can be seen compared to undoped matrices (see Table 4.1). It indicates that AOB is an effective dopant for n-type doping of the organic electron transport materials. In addition, all dopants lead to a decrease in activation energy. We should note that the maximum conductivities of doped C₆₀ thin films in our experiments are obtained here. For other matrices in Table 6.1, the doping ratio has not been varied in order to find the maximum conductivity.

Table 6.1: Conductivity and activation energy of several matrices using AOB as a dopant. All conductivity data are measured at 30° C unless specified differently in the table. Samples marked by * were illuminated by 17 W halogen lamp through the window of chamber during coevapoaration and measurement. The light intensity at the position of the sample as measured by a silicon photodiode was 4×10^{-3} mW/cm².

Sample	Doping ratio (mol%)	Conductivity (S/cm)	Activation energy (eV)
C ₆₀ :AO	8.02	6.5×10^{-2}	0.099
C ₆₀ :AOB	7.15	3.3×10^{-2}	0.14
C ₆₀ :AOB*	6.3	0.149	0.11
F ₁₆ ZnPc:AOB	7.36	2.3×10^{-5}	0.28
NTCDA:AOB*	3.1	3.9×10^{-5}	0.295
TCNQ:AOB* (28.7°C)	2.97	7.7×10^{-6}	

6.1.2 Field effect study of C₆₀ thin films doped with AOB

We have performed field effect measurements to prove the conduction type, measure the field effect mobility and calculate the charge carrier density according to $\sigma = en_e\mu_{FE}$. In our field effect study, we calculate field effect mobility using equations (3.1) and (3.2) in the linear regime. V_D is varied between 0 and 0.1 V in 0.02 V steps. Samples with different doping ratios have been investigated in the temperature range from 30°C to 70°C.

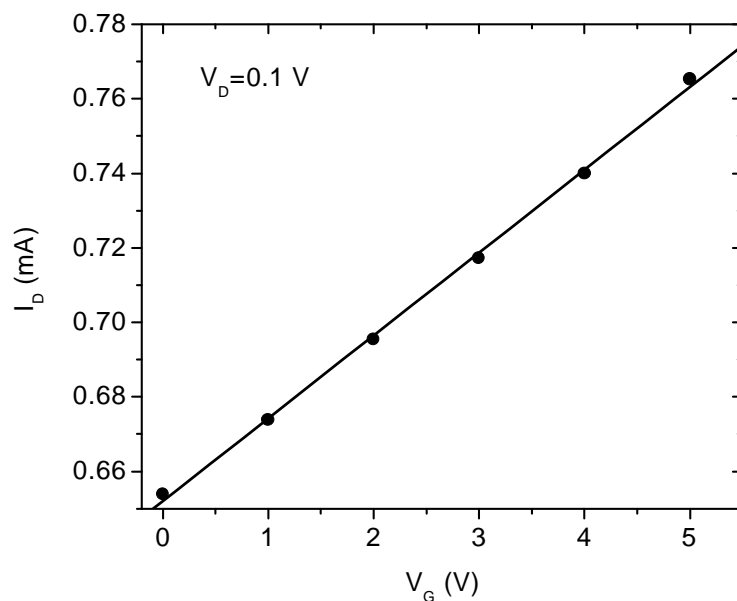


Figure 6.4: Plot of a drain current I_D vs. gate voltage V_G at drain voltage $V_D=0.1$ V for sample 56:1 (C_{60} :AOB) at 30°C

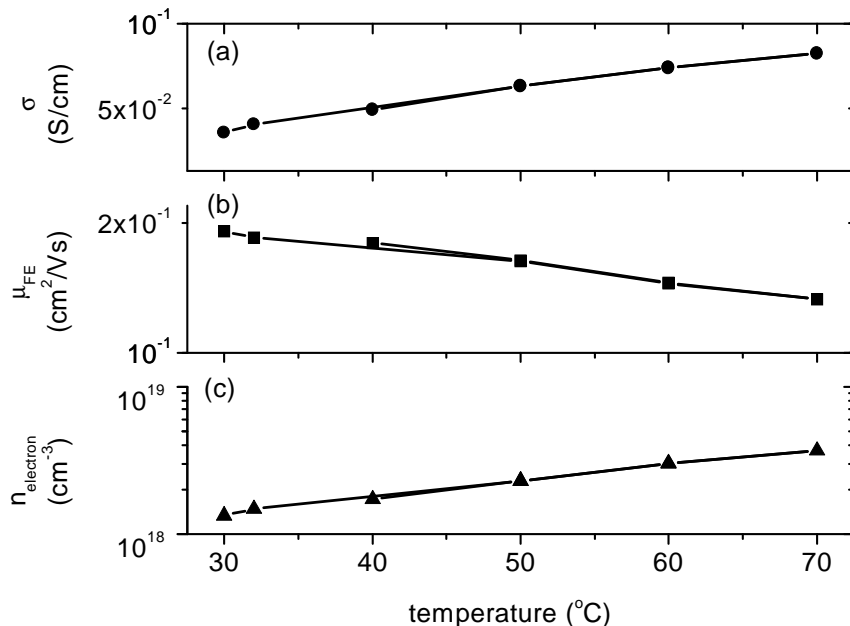


Figure 6.5: Temperature dependence of (a) measured conductivity, (b) measured mobility and (c) calculated electron density for C_{60} :AOB (56:1) in the temperature range from 30°C to 70°C in the field effect study.

Figure 6.4 shows a typical dependence of drain current I_D on gate voltage V_G at $V_D = 0.1$ V for the sample 56:1 (C_{60} :AOB) at 30°C . A similar behavior has also been ob-

served in other samples with various doping ratios at various temperatures applying different V_D . The positive sign of the field effect confirms n-type conduction.

Figure 6.5 gives the results of measured conductivity, measured field effect mobility and calculated electron density for the sample with doping ratio 1:56 in the field effect measurements. Here, the conductivity is derived from $I_D - V_D$ characteristics at $V_G = 0$ shown in Figure 6.5 (a). Exploiting the beneficial effect of illumination on the development of conductivity, the samples have been prepared under illumination with the 17 W halogen lamp as explained before. Thus, the conductivity exceeds the values from Figure 6.2, but agrees well with the data obtained before with illumination. Photoinduced charge transfer leads to an one order of magnitude increase in conductivity. In the range of temperatures studied, the conductivity maintains a temperature dependence with an activation energy of 0.14 eV. In Figure 6.5 (c), the electron density is also thermally activated with an activation energy of 0.24 eV. The electron density is $1.3 \times 10^{18} \text{ cm}^{-3}$ at 30°C. This value is about 4.3% of the dopant density of about $3 \times 10^{19} \text{ cm}^{-3}$ (estimated from the doping ratio). The electron density reaches about 12.3% of the dopant density at 70°C. This means that a deep donor state is formed when AOB is doped into C₆₀. In Figure 6.5 (b), the mobility at 30°C is about $0.19 \text{ cm}^2/\text{Vs}$. A decrease of mobility is observed with increasing temperature in the measured temperature range (30°C - 70°C). It seems to disobey a simple thermally activated hopping mechanism in which the mobility should increase with temperature.

In order to further confirm the universality of this phenomenon, we varied the doping ratio in the field effect measurements. Indeed, in other samples with various doping ratio, we also found similar phenomena. In Figure 6.6, the temperature dependence of conductivity, mobility and electron density for C₆₀:AOB (4.65:1) in the field effect study is plotted. We conclude that this trend that the mobility decreases with increasing temperature from 30°C to 70°C is universal for doped C₆₀ thin films with AOB in our experimental system.

In order to exclude the influence of experimental setup, field effect substrates or other unknown elements on the conclusion, we carried out a field effect study of NTCDA doped with AOB under nominally identical conditions. An increase of conductivity, mobility and electron density with temperature can be clearly seen as shown in Figure 6.7. We can thus conclude that the fact that mobility of C₆₀ thin films doped with AOB decreases with increasing temperature from 30°C to 70°C is significant under the given experimental conditions. This kind of temperature dependence of field effect mobility seems to be a characteristic property of C₆₀ polycrystalline films. Interestingly, a similar finding is reported by Kumashiro et al. [95]. They also

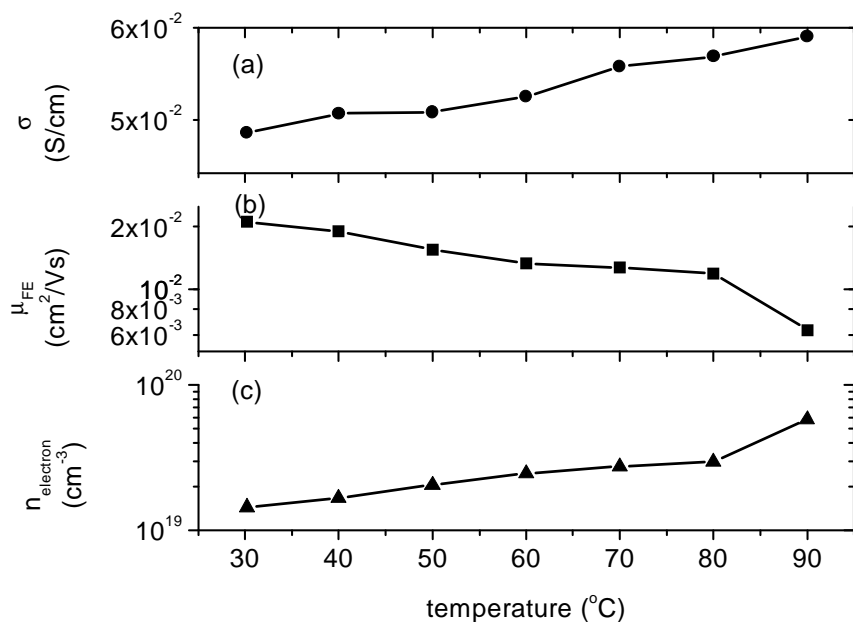


Figure 6.6: Temperature dependence of (a) measured conductivity, (b) measured mobility and (c) calculated electron density for C₆₀:AOB (4.7:1) in the temperature range from 30°C to 70°C in the field effect study.

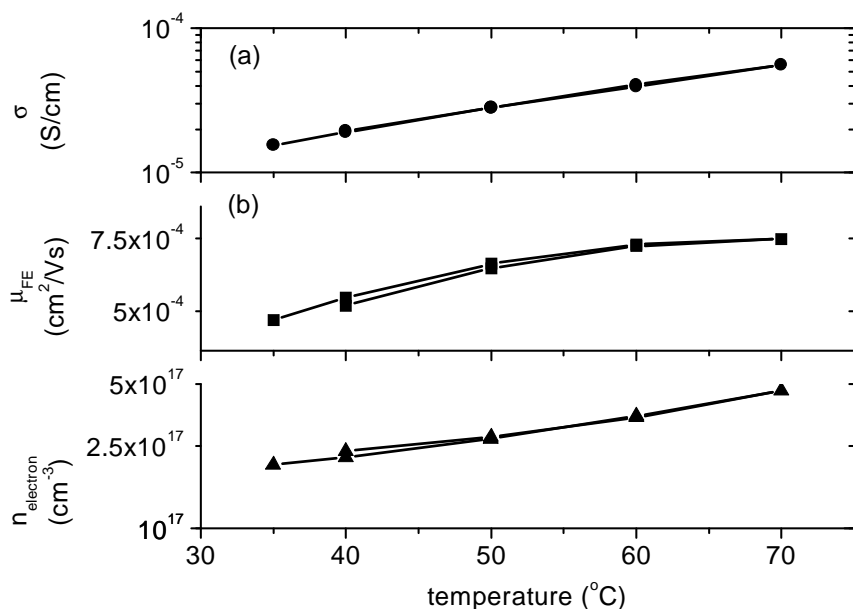


Figure 6.7: Temperature dependence of (a) measured conductivity, (b) measured mobility and (c) calculated electron density for NTCDA:AOB (57:1) in the temperature range from 30°C to 70°C in the field effect study.

observed an unusual temperature evolution of electron mobility for C₆₀ and Aza-

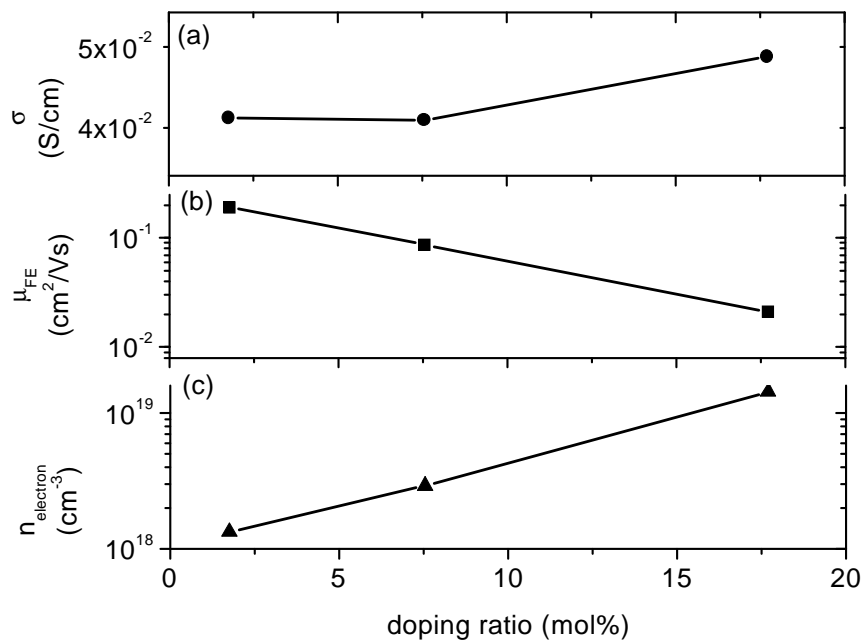


Figure 6.8: Electrical properties of a series of C₆₀ thin films doped with AOB in the field effect measurement at 30°C: (a) measured conductivity. (b) measured mobility. (c) calculated electron density. For undoped C₆₀, conductivity is 2.5×10^{-7} S/cm, mobility 5.0×10^{-4} cm²/Vs, electron density 3.2×10^{15} cm⁻³.

fullerene (C₅₉N)₂ in thin film field effect transistors. In their experiments, they found that the mobilities monotonously increased with temperature in the low temperature range and then reached a plateau and finally decreased again. It seems that the field effect mobility of C₆₀ thin films doped with AOB between 30°C and 70°C is in the decreasing region of mobility for the whole temperature range. However, there are a number of open questions on this topic, and detailed studies are required to answer them. Further work is suggested in the outlook part of this thesis.

We also carried out a field effect study of an undoped C₆₀ thin film to compare with doped thin films. In the field effect measurement of undoped C₆₀, the conductivity is 2.5×10^{-7} S/cm, the mobility 5.0×10^{-4} cm²/Vs, and the electron density 3.2×10^{15} cm⁻³ at 30°C. The conductivity and the mobility are one order of magnitude higher than the values reported by Hoshimono et al. [169]. In their field effect measurements, the electron density (4×10^{15} cm⁻³) is similar to our result.

Figure 6.8 shows the conductivity, mobility and electron density versus the molar doping ratio at 30°C in the field effect study. With increasing dopant concentration, a systematic increase in the measured conductivity and calculated electron density is observed, as shown in Figure 6.8 (a) and (c). When the doping ratio increases from 1.75 mol% to 17.7 mol%, the conductivity varies between 0.04 S/cm and 0.05

S/cm. The electron density increases from $1.3 \times 10^{18} \text{ cm}^{-3}$ to $1.4 \times 10^{19} \text{ cm}^{-3}$, which correspond to 4.3% and 4.2% of the dopant density, respectively. This means that when the dopant density increases 10 times, the free electron density also increases about 10 times. The ratio of free electron density to dopant density is a few percent when AOB is doped into C₆₀ in the field effect measurement. In Figure 6.8 (b), we can see that the mobilities decrease with increasing doping ratio because molecular dopants can disrupt the molecular stacking order, resulting in a significant reduction in charge carrier mobility. For the sample with molar doping ratio 1:56 (1.77 mol%), the field effect mobility approaches $0.2 \text{ cm}^2/\text{Vs}$.

6.1.3 Thermopower study of C₆₀ thin films doped with AOB [170]

The measurement of thermopower is a powerful tool to characterize the doping behavior of organic semiconductors [22, 79]. The energetic difference between the Fermi level and the transport state can be obtained from the Seebeck coefficient. The difference is correlated to the density of charge carriers and the efficiency of doping. With the density of the charge carriers and the conductivity, the mobility can be calculated from $\sigma = en\mu$.

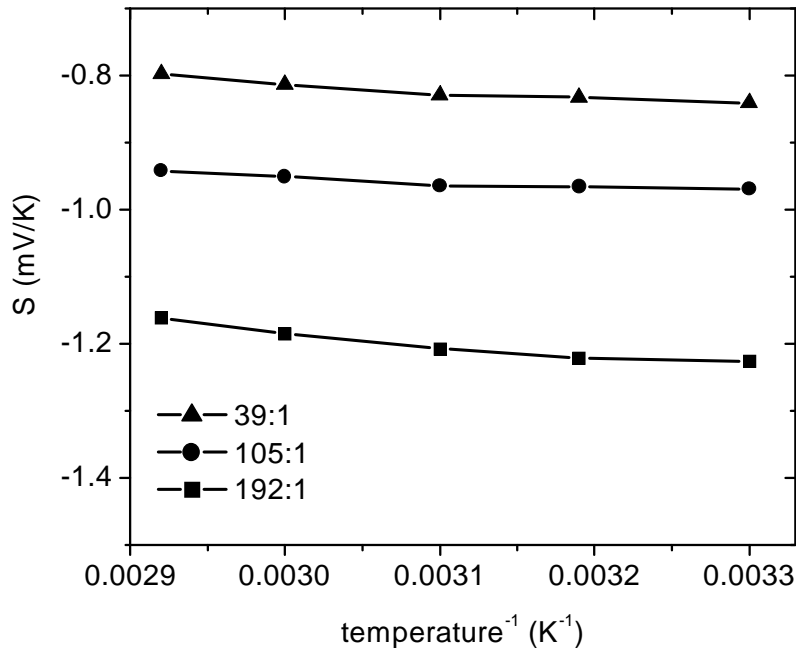


Figure 6.9: Seebeck coefficient versus reciprocal temperature for varying doping ratio.

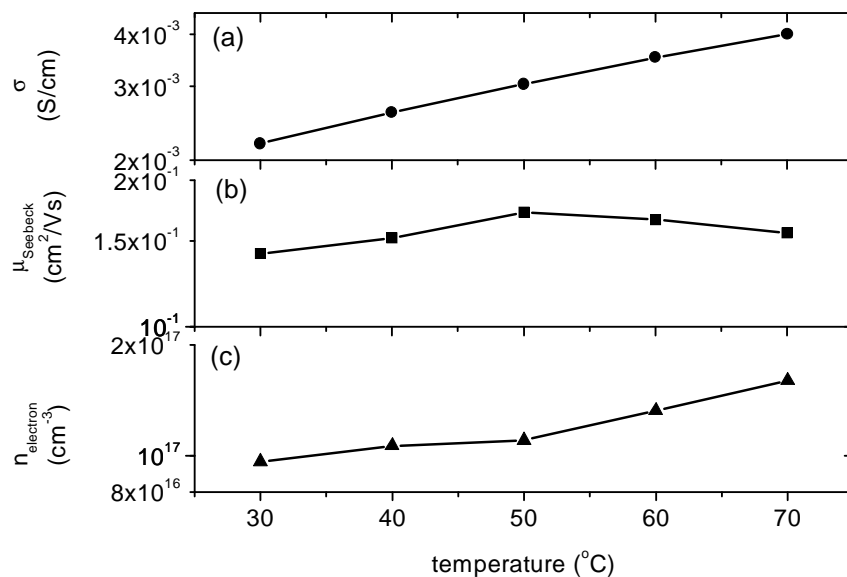


Figure 6.10: Temperature dependence of (a) measured conductivity, (b) calculated mobility and (c) calculated electron density for C₆₀:AOB (39:1) in the temperature range from 30°C to 70°C in the Seebeck study.

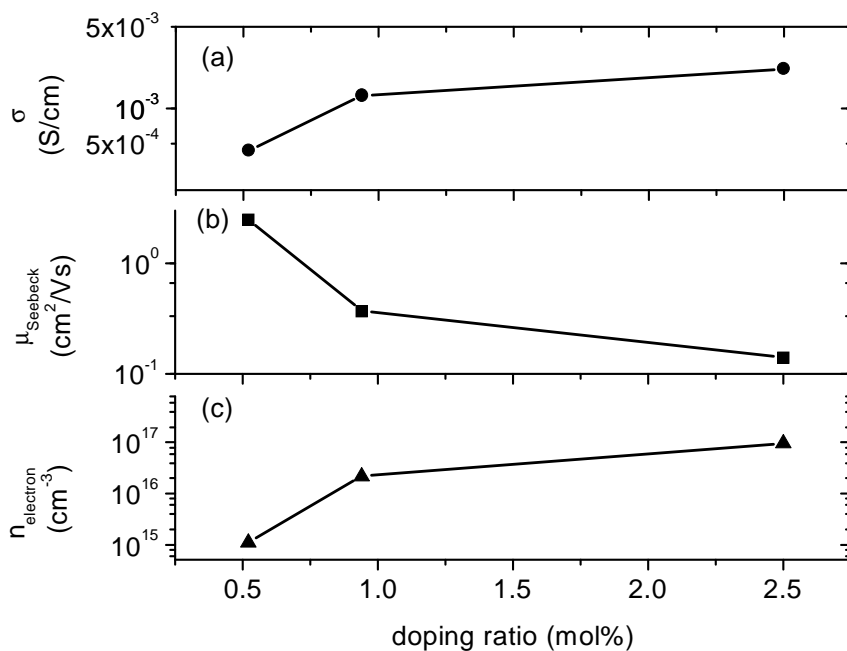


Figure 6.11: Electrical properties of a series of C₆₀ thin films doped with AOB in Seebeck measurement: (a) measured conductivity. (b) mobility calculated from calculated electron density and measured conductivity. (c) electron density calculated from the measured Seebeck coefficient.

In order to obtain more insight into the electronic properties of doped films, further study the doping effect and confirm the field effect mobility, we carried out Seebeck measurements [170].

Figure 6.9 shows the Seebeck coefficient S of the samples. Its sign is always negative, indicating electron conduction for all samples. The absolute value of S decreases with increasing concentration of AOB. The difference of the coefficient between the samples with doping ratios of 0.5 and 2.5 mol% is 0.4 mV/K, i.e., the difference between transport level and Fermi level becomes smaller with increasing doping. Each sample shows a nearly linear dependence of S on the reciprocal temperature. The coefficient of the undoped sample is difficult to determine, because the conductivity is too small to give a precise Seebeck coefficient.

The electron density at different temperature for the sample with 2.5 mol% AOB is deduced according to

$$n(T) = N_{\mu} \exp\left(\frac{e}{k_B} S\right) \propto \exp\left(-\frac{E_n}{k_B T}\right), \quad (6.1)$$

where N_{μ} is density of states, which is not known. We assume that every C₆₀ molecule contributes only one state even though its LUMO is three-fold degenerate. This assumption should be justified because it was found in cyclic voltammetry that the spacing between the first and the second reduction peak for C₆₀ is around 0.4 V [100] and thus well above $k_B T/e$ at room temperature. Accordingly, a possible multiple occupation of the C₆₀ LUMO with electrons should not play a significant role for the carrier statistics. The density of C₆₀ molecules is taken as $1.67 \times 10^{21} \text{ cm}^{-3}$, calculated from molar molecular mass (720 g/mol) and density of a thin film about 2 g/cm³. E_n is the activation energy of the electron density and k_B the Boltzmann constant. The electron density plotted in Figure 6.10 is thermally activated. The activation energy E_n of the electron density is 0.11 eV. The fact that E_n does not vanish may have two reasons. Either we are dealing with deep donor levels lying below the Fermi level. In this case, both the number of ionized dopants and the carrier density are thermally activated. On the other hand, a thermally activated electron density can also be observed with shallow donor levels if there is an additional shallow trapping level for electrons. Note that Equation 6.1 refers to the density of mobile electrons and not to the total density of free and trapped electrons because the Seebeck coefficient is related to heat transport per carrier; trapped and immobile electrons thus do not contribute. However, we can exclude the interpretation via traps since we have shown above that also the total density of free and trapped electrons deduced from field effect measurements shows a thermally activated behavior. The electron density is in the order of 10^{17} cm^{-3} which is slightly

less than the value deduced from the field effect measurements. This is reasonable because the samples for Seebeck measurements have been prepared in the dark. In Figure 6.10 (a), we also find that the conductivities are lower by more than one order of magnitude than the conductivities from the field effect measurements for photo-activated samples.

The mobilities calculated from Equation 6.2 are also shown in Figure 6.10. The mobilities are around 0.15 cm²/Vs in the measured temperature range. A temperature dependence of mobility can not be observed.

$$\sigma(T) = en(T)\mu(T) = \sigma_0 \exp\left(-\frac{E_\sigma}{k_B T}\right) \quad (6.2)$$

Conductivity, mobility and electron density versus doping ratio from the Seebeck measurement are plotted in Figure 6.11. The conductivity and electron density increase with increasing doping ratio. The mobility decreases with doping ratio because the C₆₀ crystal becomes more and more disturbed. The findings are in agreement with the results from the field effect study.

For comparison, the mobility derived from the Seebeck measurements and field effect measurements are presented in Figure 12. For a doping ratio of 2.5 mol%, the Seebeck mobility is very close to the value deduced from field-effect.

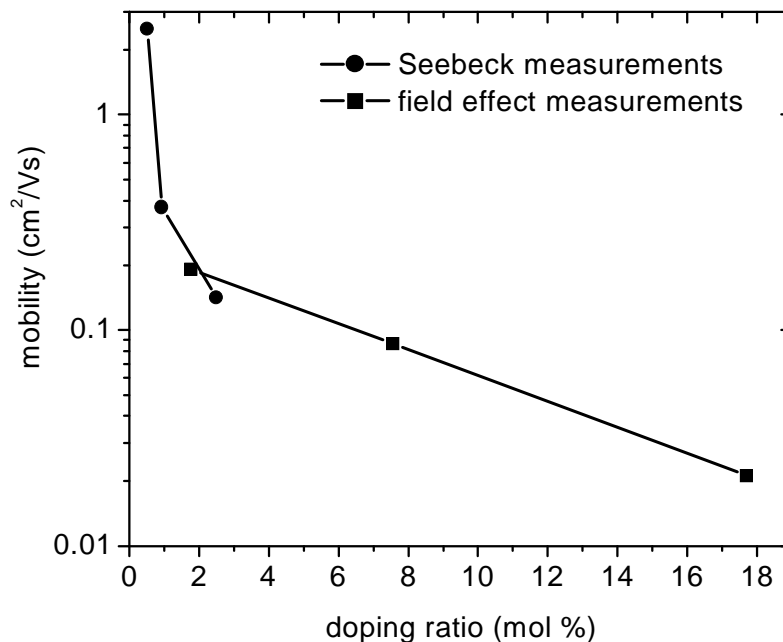


Figure 6.12: Seebeck mobility and field effect mobility vs. molar doping ratio AOB/C₆₀

6.2 Mass spectroscopy

Commercial AO purchased from Acros company (Geel, Belgium) is a complex with ZnCl_2 ($\text{C}_{17}\text{H}_{19}\text{N}_3 \cdot \text{HCl} \cdot 0.5\text{ZnCl}_2$). The empirical formula of AOB is $\text{C}_{17}\text{H}_{19}\text{N}_3$. AO can be expressed as $\text{AOB} \cdot \text{HCl} \cdot 0.5\text{ZnCl}_2$. One can expect AOB as a product after thermal dissociation of AO. When AO is sublimated from a ceramic source in high vacuum, AOB may be the main compound deposited on the substrates. To confirm this, we studied both materials by 70 eV electron impact mass spectroscopy (EI

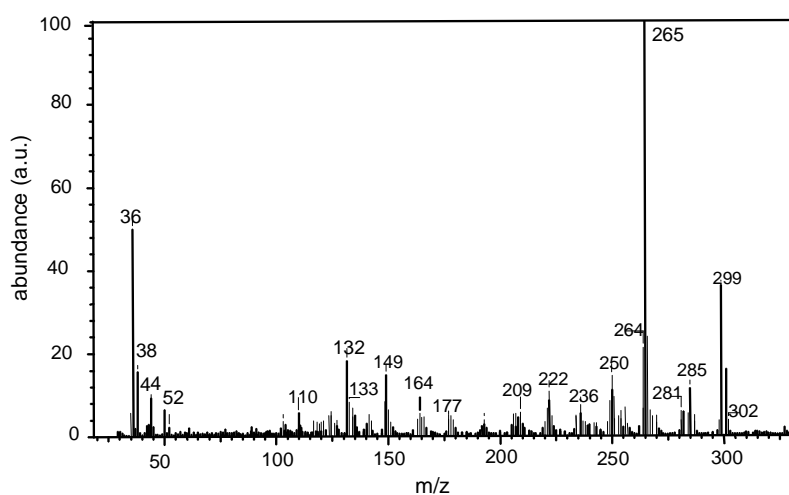


Figure 6.13: Electron impact mass spectra of AO (electron energy 70 eV). The temperature of the aluminum crucible used to evaporate the material was 200°C .

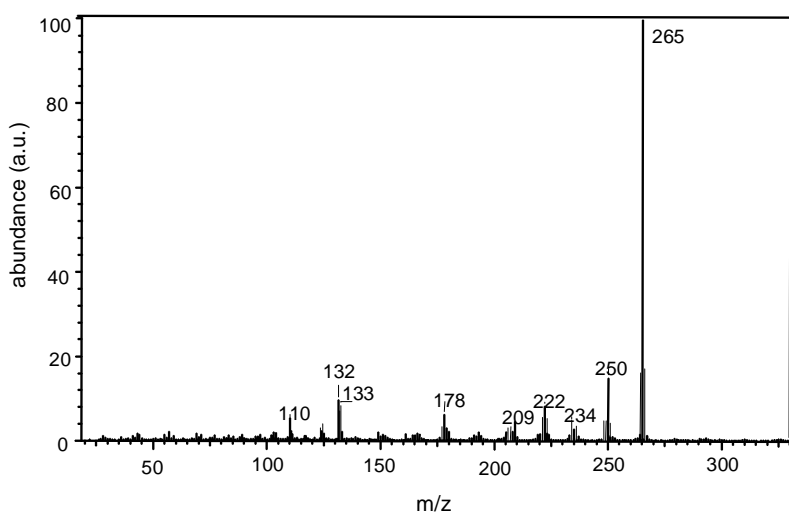


Figure 6.14: Electron impact mass spectra of AOB (electron energy 70 eV). The temperature of the aluminum crucible used to evaporate the material was 200°C .

MS) shown in Figure 6.13 and Figure 6.14. In the mass spectrum of AO (Figure 6.13), it is too difficult to assign most peaks because of low purity and complicated components of AO material (dye content >55%). However, the main peaks at 265 and 36 m/z can be easily assigned to AOB and HCl. In Figure 6.14, the molecular ion peak of AOB (m(M)=265 m/z) can be observed very clearly, too. From the mass spectra of AO and AOB in gas phase, we can conclude that AOB is a compound deposited on substrates when AO or AOB is sublimed in high vacuum. Similar doping effects of AO and AOB in electron transport materials give further evidence for this conclusion.

6.3 Optical spectroscopy of mixed films of C₆₀:AOB

6.3.1 NIR absorption spectrum of C₆₀:AOB

Figure 6.15 shows the NIR absorption spectrum of a mixed film of C₆₀ and AOB (ratio 1:1) illuminated during evaporation and encapsulated under nitrogen atmosphere after the sample had been illuminated for 22 hours in a vacuum des-

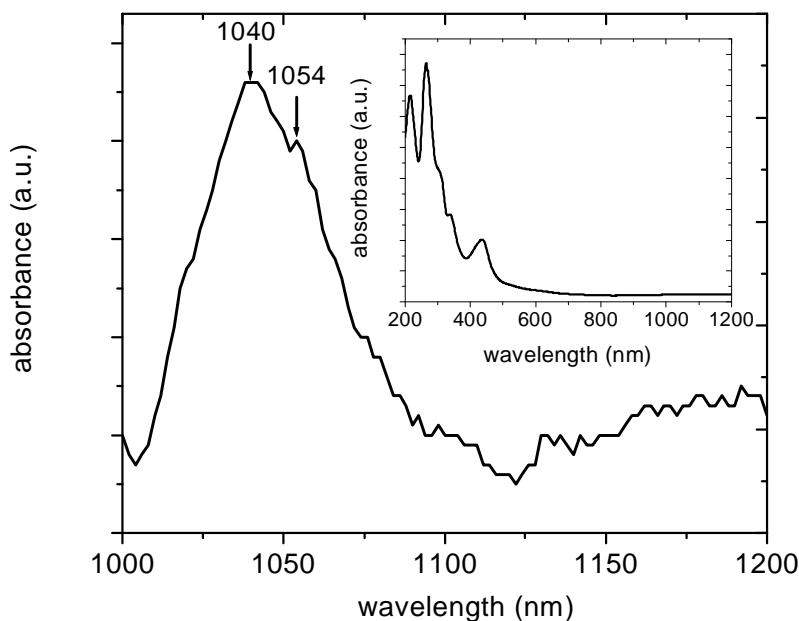


Figure 6.15: NIR electronic absorption spectrum of a mixed film of C₆₀ and AOB (1:1). The inset shows an UV/VIS/NIR (200 - 1200 nm) electronic absorption spectrum of the sample. The sample was grown under diffuse illumination under the same conditions as the sample of Figure 5.6. The sample was encapsulated in a nitrogen atmosphere and then illuminated by a 17 W halogen lamp (light intensity of 15 mW/cm²) for 22 hours in a vacuum desiccator before measurements.

icator. The peaks around 1044 and 1055 nm are attributed to the C₆₀ anion [100, 152, 155, 156, 157]. This indicates a charge transfer between C₆₀ and AOB in the mixed film.

6.3.2 FTIR spectroscopy of mixed thin film of C₆₀:AOB

In order to prove that charge transfer between C₆₀ and AOB gives rise to the obvious doping effect, we carried out FTIR spectroscopic measurements. Figure 6.16 shows a comparison of the IR transmission spectrum of an evaporated mixed film of C₆₀ and AOB with the spectra of AO and AOB solution coating films. In Figure 6.16 (b), a weak peak around 1395 cm⁻¹ marked by an arrow can be seen and is assigned to the C₆₀ anion [154, 155] while the peaks at 1182 and 1429 cm⁻¹ correspond to neutral C₆₀.

As we know, C₆₀ has two IR active modes at 1182 and 1429 cm⁻¹ in the spectral range from 1100 to 2400 cm⁻¹. Besides the peak at 1395 cm⁻¹, we can also find other new peaks at 1539, 1734, 1973, 2043, 2191, 2328 and 2348 cm⁻¹ which have appeared in the spectra of the mixed film of C₆₀ and LCV as shown in Figure 5.6 as well. Assignments of various peaks are listed in Table 5.1. Peaks at 1539, 1974, 2043, 2191, 2327 and 2347 cm⁻¹ are associated with the activation of silent modes and higher order combination modes in C₆₀ thin film because AOB as a dopant lowers the symmetry of the fullerene. Peak at 1735 cm⁻¹ is involved with Jahn-Teller active h_g modes of C₆₀⁻. Electron-phonon coupling, via the so-called Jahn-Teller (JT) effect, is believed to play an important part in determining the observed spectral properties of the fullerenes, and possibly in other icosahedral systems. Two of the most widely studied systems are t_{1u} ⊗ h_g and h_u ⊗ h_g, in which a fivefold vibration h_g is coupled to an electronic triplet (t_{1u}) and pentuplet (h_u), respectively. Molecular energy spectra indicate that these are the JT couplings seen in the ground states of C₆₀⁻ and C₆₀⁺, respectively [171].

In the spectrum of a mixed film of C₆₀:AOB (5:1) (see Figure 6.16 (b)), a new peak at 1353 cm⁻¹ is found. It corresponds to a peak at 1352 cm⁻¹ in the FTIR spectrum of AO (c) while the more pronounced peak at 1335 cm⁻¹ corresponds to the peak at 1337 cm⁻¹ in the FTIR spectrum of AOB (a). Comparing the IR spectra of AO and AOB coating films, we can find that the main difference between AO and AOB is the position of the two peaks. When AOB is positively charged as in AO, the IR peak shifts from 1337 cm⁻¹ to 1352 cm⁻¹. When $\nu_0 = 1352$ cm⁻¹, $\nu_1 = 1337$ cm⁻¹ and $\Delta\nu = (1353 - 1335)$ cm⁻¹ = 18 cm⁻¹ are introduced in Equation 3.6, the degree of charge transfer (Z) equal to 0.99 is obtained. It means that AOB as a reducing agent is oxidized into a cationic form similar to AO.

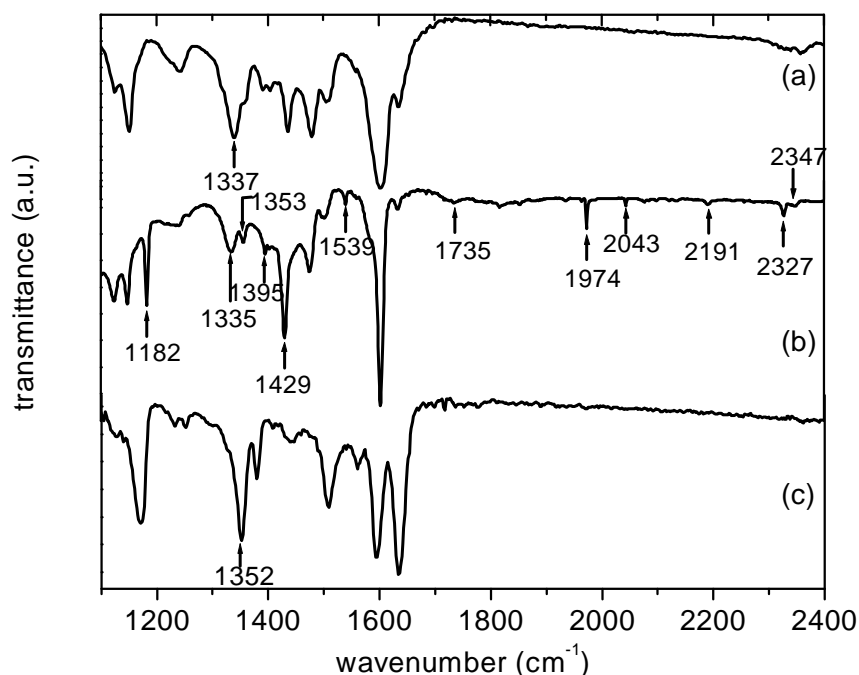


Figure 6.16: FTIR spectra of (a) AOB coating, (b) mixed layer of C₆₀:AOB (5:1) prepared by coevaporation and (c) AO coating. For the sample 5:1 (b) encapsulated in a nitrogen atmosphere before measurements, a 17 W halogen lamp was used to provide diffuse illumination in the chamber during the growth of mixed layers by vacuum-deposition. The light intensity at the position of the sample as measured by a silicon photodiode was 4×10^{-3} mW/cm².

From the above discussion, we drive that a charge transfer between C₆₀ and AOB results in an increase of free electron density in the thin film, leading to an increase in n-type conductivity. However, it should be noted that there are different charge transfer mechanisms when LCV and AOB are used as n-type dopants in the C₆₀, respectively. In the case of the LCV, hydride transfer makes photoinduced electron transfer irreversible. The electron transfer accompanied by hydride transfer from LCV to C₆₀ needs be activated by external light or heating. However, from conductivity results, it seems that the irreversible redox reaction between C₆₀ and AOB that induces the doping effect takes place more easily than for LCV and C₆₀.

6.4 Electrochemistry of AO and AOB

To learn the redox process between AOB and C₆₀, we study the electrochemical properties of AOB and AO using cyclic voltammetry (CV) as shown in Figure 6.17. All redox processes in the measurements are nearly irreversible. Two oxidation peaks

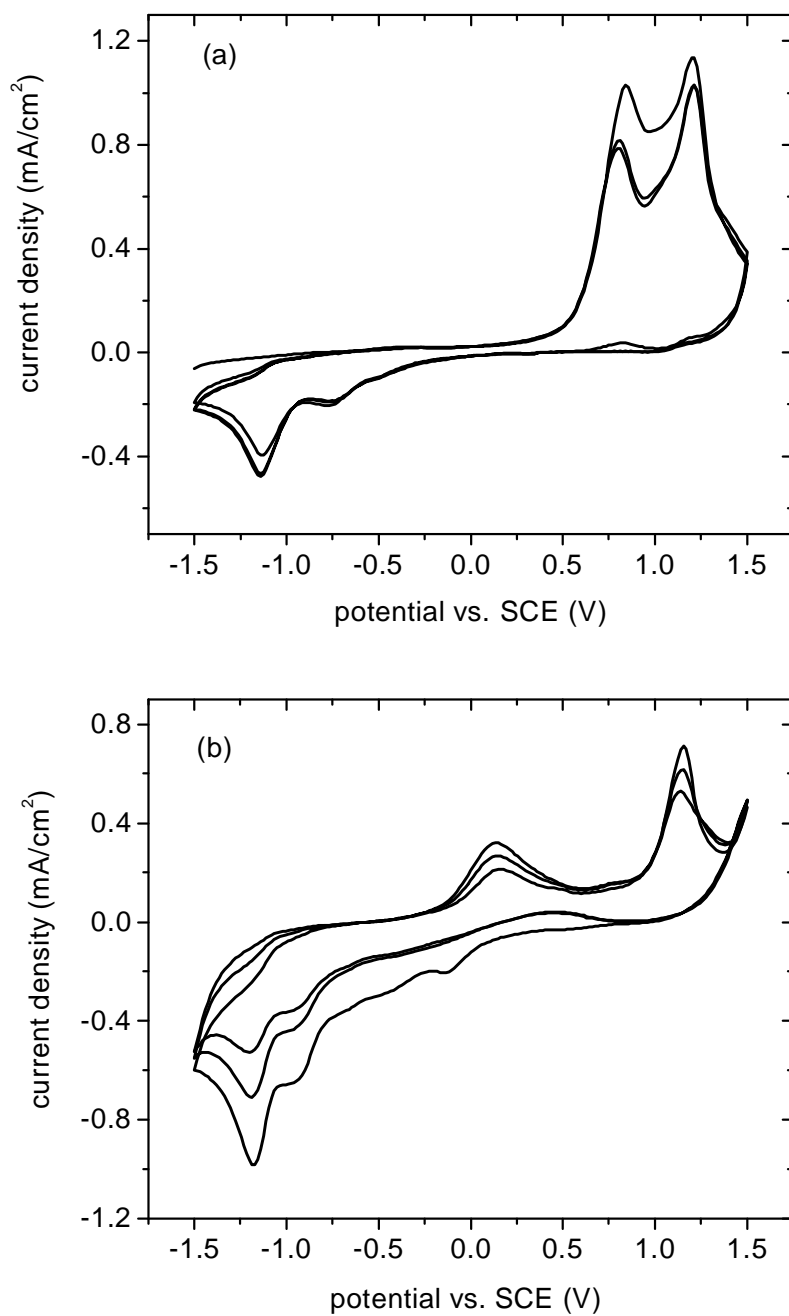


Figure 6.17: Cyclic voltammograms of (a) AOB, scan rate 100 mV/s and (b) AO, scan rate 200 mV/s in acetonitrile containing 0.1M Bu_4NBF_4 under Argon atmosphere. A saturated calomel electrode (SCE) is used as the reference electrode.

of AOB at 0.8 and 1.2 V vs. SCE, and two reduction peaks at -1.14 and -0.77 V vs. SCE can be observed in Figure 6.17 (a). The second oxidation peak at 1.2 V vs. SCE of AOB is similar to the oxidation peak at 1.16 V vs. SCE of AO (see Figure

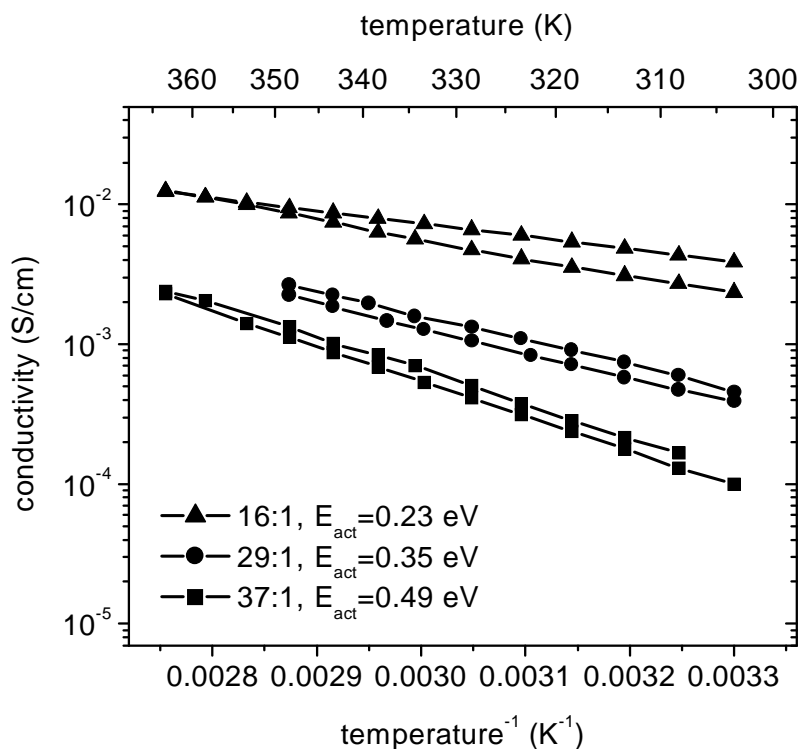


Figure 6.18: Conductivity vs. reciprocal temperature for C₆₀ thin films doped with BEDT-TTF. The activation energy of three samples is 0.23, 0.35, 0.49 eV respectively.

6.17 (b)). It means that AO is formed after AOB is oxidized and then AO with one positive charge can be further oxidized. At the same time, AO has reduction peak (-1.19 V vs. SCE) similar to the peak at -1.14 V vs. SCE observed in Figure 6.17 (a) for AOB. CV data of AOB and AO show that AOB is oxidized into AO in the acetonitrile containing 0.1M Bu₄NBF₄ under Argon atmosphere. Therefore, we can conclude: First, AOB itself is not a strong electron donor. Second, oxidation of AOB is irreversible. These findings indicate that a single charge transfer between C₆₀ and AOB can not explain this system at all.

To check this idea, we carried out a conductivity study of C₆₀ doped with BEDT-TTF, which is a stronger electron donor with the oxidation potential of 0.48 V vs. SCE. Figure 6.18 shows the doping effect of BEDT-TTF in C₆₀. Both a thermally activated behavior and an influence of the dopant concentration can be observed, like for all doped organic thin films in our study. The conductivity of 3×10^{-3} S/cm at 30°C was achieved for a molar doping ratio of 16:1 (C₆₀:BEDT-TTF), which is at least one order of magnitude lower than C₆₀:AOB with similar doping ratio. Important is that we found that the samples reached their steady states soon after

coevaporation and later annealing did not obviously increase the conductivity. It is clear that a single charge transfer between C_{60} and BEDT-TTF took place, like for ZnPc thin films doped with F_4TCNQ .

However, in the case of AOB with high oxidation potential, which leads to much better doping effect in C_{60} thin films treated by illumination, we can assume that an irreversible redox reaction between AOB and C_{60} takes place in codeposited films which can be accelerated by heating or illumination: When AOB is excited by illumination, the electron on its LUMO is transferred to C_{60} leading to an AOB radical cation. From cyclic voltammetric studies, we know that this AOB radical cation is not stable, but has a strong tendency to bind an additional hydrogen to the nitrogen in the core of the molecule leading to AO. When mixed into C_{60} , additional hydrogen atoms are not available. We therefore speculate that a chemical bond may be formed between the AOB radical cation and C_{60} . The resulting AOB- C_{60} -dyads may act as the dopant, i.e. the doped layer comprises as many free electrons on C_{60} as positively charged AOB- C_{60} dyads to ensure charge neutrality.

6.5 Conclusions

We have shown that fullerene C_{60} can be effectively doped with acridine orange and acridine orange base by the coevaporation technique. An increase of six orders of magnitude in conductivity of doped C_{60} has been achieved compared to undoped C_{60} . AO and AOB give similar doping effect in C_{60} . Electron impact mass spectroscopy proves that AOB is the main product after AO is thermally dissociated in vacuum. In the conductivity measurements, the highest conductivity of 6.5×10^{-2} S/cm at 30°C is achieved for a molar doping ratio of 11:1 (C_{60} :AO) with an activation energy of 0.1 eV. When C_{60} is doped with AOB, the conductivity at 30°C reaches 3×10^{-2} S/cm for a sample with 6 mol% AOB and with an activation energy of 0.15 eV. It is found that the dark conductivity of C_{60} doped thin films can be enhanced by a light-induced activation of the dopant precursor AOB. In the field effect and Seebeck measurements, n-type conductance is confirmed. An obvious doping effect of AOB as an n-type dopant in C_{60} is observed in conductivity, field effect and Seebeck measurements. AOB doping leads to the formation of deep donor states in the C_{60} thin film. A field effect mobility of $0.19 \text{ cm}^2/\text{Vs}$ is achieved in the sample with ~ 2 mol% AOB. NIR and FTIR spectra demonstrate electron transfer from the dopants to the matrices. For C_{60} doped with AOB, C_{60}^- is present in NIR absorption and FTIR spectra. On the other hand, a peak corresponding to acridine orange (AO^+) is also observed in the FTIR spectrum of C_{60} :AOB, where AO corresponds

to AOB with one additional hydrogen attached. Electrochemical data of AOB and AO in acetonitrile suggest that the AOB radical cation is not stable, but is rapidly transformed into a compound with similar properties to AO. We speculate that, in the codeposited layers, this compound is a dyad of AOB⁺-C₆₀⁻ connected by a C-N chemical bond.

Chapter 7

Summary and outlook

7.1 Summary

In this thesis, we discuss n-type doping of organic semiconductor thin films using organic small molecules as dopants by coevaporation. Novel dopants (cationic dyes and their bases) for n-type doping of electron transport materials with low-lying LUMO were investigated. Our results show that cationic dyes and their bases are efficient n-type dopants for electron transport materials such as C_{60} , $F_{16}ZnPc$, NTCDA and others.

Firstly, we presented detailed investigations on a new approach for n-type doping of organic thin films using cationic dyes as dopants. Cationic dyes can form strong donors in situ by sublimation. Spectroscopic investigations reveal that the leuco bases of cationic dyes are formed in situ during evaporation of xanthene cationic dyes and triphenylmethane cationic dyes. A conductivity study of organic electron transport materials (with low lying LUMO) doped with the cationic dyes has been carried out. All dopants used in the study give rise to an increase of several orders of magnitude in conductivity with dopant concentration, accompanied by a decrease in activation energy. This means that cationic dyes are effective dopants for n-type doping of organic electron transport materials with moderate acceptor strength. From a combined MS, UV/VIS/NIR and FTIR spectroscopy study, we identify the colorless reduced forms of the cationic dyes as the main constituent of vacuum deposited layers. The leuco forms are transformed back to the dye cation upon oxidation in air or by a stronger acceptor, TCNQ. Irreversible charge transfer reaction between electron donor and acceptor leads to obvious n-type doping effect. Deep donor states are formed in weak acceptor-type matrices.

Furthermore, we showed that fullerene C_{60} can be effectively doped with LCV by the coevaporation technique. An increase of six orders of magnitude in conductivity of

doped C_{60} has been achieved, compared to undoped C_{60} . LCV gives similar doping effect in C_{60} to CV. Electron transfer following hydride transfer from LCV to the matrices gives rise to n-type doping. For TCNQ:LCV blend layers, TCNQ anions and CV cations are clearly observed in UV/VIS/NIR absorption and FTIR spectra. A one-electron transfer from LCV to TCNQ can be found. When C_{60} is doped with LCV, $C_{60}^{\cdot-}$ is present in NIR absorption and FTIR spectra. For weaker acceptors like C_{60} , it is obvious that a combined hydride and electron transfer reaction has to be supported by outer activation (light or heating). When C_{60} accepts hydrogen atoms or radicals, it can be reduced to hydrofullerene. An irreversible electron transfer reaction leads to a stable n-doping effect in organic thin films of C_{60} doped with LCV.

Finally, doping of fullerene C_{60} thin films with acridine orange (AO) and acridine orange base (AOB) by the coevaporation technique are reported. AO and AOB give rise to obvious doping effect in C_{60} . EI MS shows that AOB is a main product after AO is thermally dissociated in vacuum. It is found that the dark conductivity of C_{60} doped thin films can be enhanced by a light-induced activation of dopant precursor AOB: A conductivity up to 6×10^{-2} S/cm at 30°C is achieved when a diffusive illumination is provided in the vacuum chamber during the evaporation. The field effect and Seebeck measurements confirm the n-type conduction of C_{60} thin films and show that deep donor states are formed in AOB-doped C_{60} films. A field effect mobility of $0.19 \text{ cm}^2/\text{Vs}$ is achieved for a doping level of 2 mol%. NIR and FTIR spectra demonstrate electron transfer from the dopant to the matrix: For C_{60} doped with AOB, C_{60}^- is present in NIR absorption and FTIR spectra. On the other hand, a peak corresponding to acridine orange (AO^+) is also observed in the FTIR spectrum of C_{60} :AOB. Electrochemical data of AOB and AO in acetonitrile suggest that the AOB radical cation is not stable but is rapidly transformed into a compound with similar properties to AO. We assume that, in the codeposited layers, this compound is a dyad of AOB^+ and C_{60}^- connected by a C-N chemical bond.

7.2 Outlook

For a deeper understanding of the n-doping mechanism, in particular in terms of physics, it is obvious that some further experimental and theoretical considerations are necessary. Currently, we work on some field effect and Seebeck measurements of C_{60} doped thin films. To achieve an unambiguous description of doping mechanism, detailed field effect and Seebeck measurements have to be carried out. These tasks include more extensive field effect and Seebeck measurements of doped C_{60} thin

films using LCV and AOB with various doping ratios at different temperature, an improvement in technology to enhance the reproducibility of data and reduce the experimental errors. In our previous work, we found that the n-doping in our study is strongly influenced by various environment factors, i.e. illumination, vacuum or temperature, and some unknown factors. Thus a stable, nominally identical and optimized condition in the vacuum chamber is required.

In addition, we observed an unusual temperature-dependence of the mobility of doped C_{60} thin films in field effect and Seebeck studies as shown in Chapter 6. Such a temperature dependence may occur when the films are sufficiently crystalline. In order to confirm that there is still good crystallinity in doped C_{60} thin films, X-ray diffraction experiments are necessary.

The occurrence of the maximum and the positive temperature dependence at lower temperatures is most likely a trap-related phenomenon. A study of low temperature field effect mobility and Seebeck measurements is required to investigate transport behavior of charge carriers in doped and undoped C_{60} thin films by vacuum deposition.

Fullerenes consist of hexagonal and pentagonal rings which form a practically spherical surface of the molecule making C_{60} different from other planar π -acceptors. The shape of the t_{1u} (LUMO) molecular orbital of C_{60} is also close to spherical. Therefore, a close approach of the donor and C_{60} molecules, and parallel arrangements of their molecular orbitals for an effective overlapping, are mainly defined by steric compatibility between the shape of donor and the fullerene molecules [136, 173, 174]. Steric compatibility between dopant and matrix is an important factor influencing the doping effect. If the steric complementarity of the shapes of donor molecule to matrix is good, there is a close approach between donor and acceptor and an effective overlapping of molecular orbitals can be achieved more easily. Normally, dopants disrupt the molecular stacking order, resulting in a significant reduction in charge carrier mobility. A good steric compatibility between dopant and matrix can effectively decrease a loss of crystalline order in the matrix lattice. In order to confirm this assumption, the doping of same matrix using various dopants with different steric hindrances should be tried. At the same time, the morphology of thin films prepared by coevaporation should also be investigated by microscopic techniques, for example, atomic force microscopy (AFM) or transmission electron microscopy (TEM) and so on.

We have observed the existence of the C_{60} anion radical in the FTIR spectra of a few samples. In fact, a quantitative analysis is possible if more detailed experiments are carried out. In addition, Raman is also a very useful tool to characterize CT and

quantitatively describe C_{60} anion radical. Neutral C_{60} has 10 allowed Raman modes [112]. It was discovered that the A_g pentagonal pinch mode at 1467 cm^{-1} is a good indicator of charge state, which decreases monotonically by ca. 6 cm^{-1} for each added negative charge [99]. Because Raman and IR are complementary each other in molecular vibration, there is considerable opportunity for further experiments using Raman spectroscopy as infrared spectroscopy.

References

- [1] S. R. Forrest, *Nature* **428**, 911 (2004).
- [2] M. Pfeiffer, K. Leo, X. Zhou, J. S. Huang, M. Hofmann, A. Werner, J. Blochwitz-Nimoth, *Org. Elec.* **4**, 89 (2003).
- [3] S. R. Forrest, *Chem. Rev.* **97**, 1793 (1997).
- [4] K. M. Vaeth, *Inform. Display* **19**, 12 (2003).
- [5] D. J. Gundlach, Y. Y. Lin, T. N. Jackson, *IEEE Electron. Dev. Lett.* **18**, 87 (1997).
- [6] M. Shtein, J. Mapel, J. B. Benziger, S. R. Forrest, *Appl. Phys. Lett.* **81**, 268 (2002).
- [7] P. Peumans, S. R. Forrest, *Appl. Phys. Lett.* **79**, 126 (2001).
- [8] M. Granstrom, K. Petritsch, A. C. Arias, A. Lux, M. R. Andersson, R. H. Friend, *Nature* **395**, 257 (1998).
- [9] P. Peumans, S. Uchida, S. R. Forrest, *Nature* **425**, 158 (2003).
- [10] S. E. Shaheen, C. J. Brabec, N. S. Sariciftci, F. Padinger, T. Fromherz, J. C. Hummelen, *Appl. Phys. Lett.* **78**, 841 (2001).
- [11] C. W. Tang, *Appl. Phys. Lett.* **48**, 183 (1986).
- [12] C. W. Tang, A. V. Slyke, *Appl. Phys. Lett.* **51**, 913 (1987).
- [13] B. Maennig, M. Pfeiffer, A. Nollau, X. Zhou, P. Simon, K. Leo, *Phys. Rev. B* **64**, 195208 (2001).
- [14] J. Blochwitz, T. Fritz, M. Pfeiffer, K. Leo, D. M. Alloway, P. A. Lee, N. R. Armstrong, *Org. Elec.* **2**, 97 (2001).
- [15] W. Gao, A. Kahn, *Appl. Phys. Lett.* **79**, 4040 (2001).
- [16] J. Huang, M. Pfeiffer, A. Werner, J. Blochwitz, Sh. Liu, K. Leo, *Appl. Phys. Lett.* **80**, 139 (2002).
- [17] M. Pfeiffer, S. R. Forrest, K. Leo, M. E. Thompson, *Adv. Mater.* **14**, 1633 (2002).
- [18] X. Zhou, M. Pfeiffer, J. S. Huang, J. Blochwitz-Nimoth, D. S. Qin, A. Werner, J. Drechsel, B. Maennig, K. Leo, *Appl. Phys. Lett.* **81**, 922 (2002).
- [19] M. Pfeiffer, S. R. Forrest, X. Zhou, K. Leo, *Org. Elec.* **4**, 21 (2003).
- [20] J. Kido, T. Matsumoto, *Appl. Phys. Lett.* **73**, 2866 (1998).
- [21] G. Parthasarathy, C. Shen, A. Kahn, S. R. Forrest, *J. Appl. Phys.* **89**, 4986 (2001).
- [22] A. Nollau, M. Pfeiffer, T. Fritz, K. Leo, *J. Appl. Phys.* **87**, 4340 (2000).
- [23] H. X. Li, D. Q. Zhang, B. Zhang, Y. Yao, W. Xu, D. B. Zhu, Z. Wang, *J. Mater. Chem.* **10**, 2063 (2000).

- [24] S. F. Nelsen, *J. Am. Chem. Soc.* **89**, 5925 (1967).
- [25] J. D. Anderson, E. M. McDonald, P. A. Lee, M. L. Anderson, E. L. Ritchie, H. K. Hall, T. Hopkins, E. A. Mash, J. Wang, A. Padias, S. Thayumanavan, S. Barlow, S. R. Marder, G. E. Jabbour, S. Shaheen, B. Kippelen, N. Peyghambarian, R. M. Wightman, N. R. Armstrong, *J. Am. Chem. Soc.* **120**, 9646 (1998).
- [26] B. A. Gregg, S. Chen, H. M. Branz, *Appl. Phys. Lett.* **84**, 1707 (2004).
- [27] A. Werner, *N-type doping of organic thin films using a novel class of dopants*, PhD thesis, Technische Universität Dresden (2003).
- [28] A. Werner, F. Li, K. Harada, M. Pfeiffer, T. Fritz, K. Leo, *Appl. Phys. Lett.* **82**, 4495 (2003).
- [29] A. Werner, F. Li, K. Harada, M. Pfeiffer, T. Fritz, K. Leo, *Adv. Func. Mater.* **14**, 255 (2004).
- [30] F. Li, A. Werner, K. Harada, B. Maennig, J. Drechsel, K. Leo, M. Pfeiffer, *Proceedings of The International Society for Optical Engineering (SPIE)*, Bellingham, **5464**, 364 (2004).
- [31] D. Gebeyehu, B. Maennig, J. Drechsel, K. Leo, M. Pfeiffer, *Sol. En. Mat. Sol. Cells* **79**, 81 (2003).
- [32] B. Maennig, J. Drechsel, D. Gebeyehu, P. Simon, F. Kozlowski, A. Werner, F. Li, S. Grundmann, S. Sonntag, M. Koch, K. Leo, M. Pfeiffer, H. Hoppe, D. Meissner, N. S. Sariciftci, I. Riedel, V. Dyakonov, J. Parisi, *Appl. Phys. A* **79**, 1 (2004).
- [33] K. Harada, PhD thesis, in preparation, Institut für Angewandte Photophysik, Technische Universität Dresden.
- [34] E. A. Silinsh, *Organic molecular crystals, their electronic states*, *Solid-State Sciences* 16, Springer, Heidelberg (1980).
- [35] M. Pfeiffer, *Controlled doping of organic vacuum deposited dye layers: basics and applications*, PhD thesis, Technische Universität Dresden (1999).
- [36] A. Nollau, *Investigation of the doping process in organic molecular thin films*, PhD thesis, Technische Universität Dresden (2002).
- [37] N. Karl, *Synth. Met.* **133-134**, 649 (2003).
- [38] R. G. Kepler, *Phys. Rev.* **119**, 1226 (1960).
- [39] N. Karl, In: R. Farchioni, G. Grosso (Eds.), *Organic electronic materials*, Springer, Berlin, pp. 283-326 (2001).
- [40] J. Mort, G. Pfister, In: J. Mort, G. Pfister (Eds.), *Electronic properties of polymers*, Wiley, New York, pp. 215-265 (1982).
- [41] K. Arlauskas, V. Gaidelis, K. Genevicius, G. Juska, *Synth. Met.* **109**, 101 (2001).
- [42] G. Juska, K. Arlauskas, R. Sterbacka, H. Stubb, *Synth. Met.* **109**, 173 (2000).

-
- [43] A. M. van de Graats, J. M. Warman, M. P. de Haas, D. Adam, J. Simerer, D. Haarer, P. Schuhmacher, *Adv. Mater.* **8**, 823 (1996).
- [44] G. H. Gelnick, J. M. Warman, *J. Phys. Chem.* **100**, 20035 (1996).
- [45] R. J. Hoofman, L. D. Sibbeles, M. P. de Haas, A. Hummel, D. Bloor, *J. Chem. Phys.* **109**, 1885 (1998).
- [46] M. Pope, C. E. Swenberg, *Electronic Processes in Organic Crystals and Polymers*, Oxford University Press, New York (1999).
- [47] P. H. Nguyen, G. Paasch, W. Brütting, W. Riess, *Phys. Rev. B* **49**, 5172 (1994).
- [48] W. Brütting, P. H. Nguyen, W. Riess, G. Paasch, *Phys. Rev. B* **51**, 9533 (1995).
- [49] G. Horowitz, R. Hajlaoui, H. Bouchriha, R. Bourguiga, M. Hajlaoui, *Adv. Mater.* **10**, 923 (1998).
- [50] G. Horowitz, R. Hajlaoui, D. Fichou, A. El Kassmi, *J. Appl. Phys.* **85**, 3202 (1999).
- [51] N. Karl, K. Kraft, J. Marktanner, *Synth. Met.* **109**, 181 (2000).
- [52] W. Warta, R. Stehle, N. Karl, *Appl. Phys. A* **36**, 163 (1985).
- [53] N. Karl, J. Marktanner, R. Stehle, W. Warta, *Synth. Met.* **42**, 2473 (1991).
- [54] D. M. Burland, U. Konzelmann, *J. Chem. Phys.* **67**, 319 (1977).
- [55] D. M. Burland, *Phys. Rev. Lett.* **33**, 833 (1974).
- [56] C. D. Dimitrakopoulos, P. R. L. Malenfant, *Adv. Mater.* **14**, 99 (2002).
- [57] H. Bässler, *Phys. Status Solidi B* **175**, 15 (1993).
- [58] S. D. Baranovskii, T. Faber, F. Hensel, G. Leising, *J. Phys.: Condens. Matter* **9**, 2699 (1997).
- [59] S. D. Baranovskii, I. P. Zvyagin, H. Cordes, S. Yamasaki, P. Thomas, *J. Non-Cryst. Solids* **299**, 416 (2002).
- [60] H. Böttger, V. V. Bryskin, *Hopping conduction in solids*, Akademie Verlag, Berlin (1985).
- [61] D. H. Dunlap, P. E. Parris, V. M. Kenkre, *Phys. Rev. Lett.* **77**, 542 (1996).
- [62] S. N. Novikov, D. H. Dunlap, V. M. Kenkre, P. E. Parris, A. V. Vannikov, *Phys. Rev. Lett.* **81**, 4472 (1998).
- [63] S. D. Baranovskii, I. P. Zvyagin, H. Cordes, S. Yamasaki, P. Thomas, *Phys. Status Solidi B* **230**, 281 (2002).
- [64] H. Cordes, S. D. Baranovskii, J. Greif, *Phys. Status Solidi B* **230**, 243 (2002).
- [65] D. Monroe, *Phys. Rev. Lett.* **54**, 146 (1985).
- [66] R. Schmechel, *Phys. Rev. B* **66**, 235206 (2002).

- [67] R. Schmechel, *J. Appl. Phys.* **93**, 4653 (2003).
- [68] M. C. J. M. Vissenberg, M. Matters, *Phys. Rev. B* **57**, 12964 (1998).
- [69] A. Ahmad, R. A. Collins, *Phys. Status Solidi A* **123**, 201 (1991).
- [70] S. Saito, A. Oshiyama, *Phys. Rev. Lett.* **66**, 2637 (1991).
- [71] V. I. Arkhipov, P. Heremans, E. V. Emelianova, G. J. Adriaenssens, H. Bässler, *J. Non-Cryst. Solids* **338-340**, 603 (2004).
- [72] V. I. Arkhipov, P. Heremans, E. V. Emelianova, G. J. Adriaenssens, H. Bässler, *Appl. Phys. Lett.* **82**, 3245 (2003).
- [73] A. Miller, E. Abraham, *Phys. Rev.* **120**, 745 (1960).
- [74] Y. Shen, K. Diest, M. H. Wong, B. R. Hsieh, D. H. Dunlap, G. G. Malliaras, *Phys. Rev. B* **68**, 081204 (2003).
- [75] P. M. Borsenberger, J. J. Fitzgerald, *J. Phys. Chem.* **97**, 4815 (1993).
- [76] V. Ambegaokar, B. I. Halperin, J. S. Langer, *Phys. Rev. B* **4**, 2612 (1971).
- [77] B. A. Gregg, *J. Phys. Chem. B* **108**, 17285 (2004).
- [78] B. A. Gregg, S. Chen, R. A. Cormier, *Chem. Mater.* **16**, 4586 (2004).
- [79] M. Pfeiffer, A. Beyer, T. Fritz, K. Leo, *Appl. Phys. Lett.* **73**, 3202 (1998).
- [80] M. Pfeiffer, A. Beyer, B. Plönnigs, A. Nollau, T. Fritz, K. Leo, D. Schlettwein, S. Hiller, D. Wöhrle, *Sol. En. Mat. Sol. Cells* **63**, 83 (2000).
- [81] B. A. Gregg, R. A. Cormier, *J. Am. Chem. Soc.* **123**, 7959 (2001).
- [82] C. P. Jarrett, R. H. Friend, A. R. Brown, D. M. de Leeuw, *J. Appl. Phys.* **77**, 6289 (1995).
- [83] A. J. Heeger, *J. Phys. Chem. B* **105**, 8475 (2001).
- [84] D. M. de Leeuw, *Synth. Met.* **57**, 3597 (1993).
- [85] J. A. Reedijk, H. C. F. Martens, H. B. Brom, M. A. Michels, *Phys. Rev. Lett.* **83**, 3904 (1999).
- [86] F. Zuo, M. Angelopoulos, A. G. MacDiarmid, A. J. Epstein, *Phys. Rev. B* **39**, 3570 (1989).
- [87] G. L. Pearson, J. Bardeen, *Phys. Rev.* **75**, 865 (1949).
- [88] P. P. Debye, E. M. Conwell, *Phys. Rev.* **93**, 693 (1954).
- [89] G. F. Neumark, *Phys. Rev. B* **5**, 408 (1972).
- [90] G. W. Castellan, F. Seitz, In: *Semiconducting Materials*, H. K. Henisch(Ed.), Butterworth, London (1951).

- [91] G. Horowitz, *Adv. Mater.* **10**, 365 (1998).
- [92] S. F. Nelson, Y. Y. Lin, D. J. Gundlach, T. N. Jackson, *Appl. Phys. Lett.* **72**, 1854 (1998).
- [93] Y. Y. Lin, D. J. Gundlach, S. Nelson, T. N. Jackson, *IEEE Electron Device Lett.* **18**, 606 (1997).
- [94] C. Dimitrakopoulos, S. Purushothaman, J. Kymissis, A. Callegari, J. M. Shaw, *Science* **283**, 822 (1999).
- [95] R. Kumashiro, K. Tanigaki, H. Ohashi, N. Tagmatarchis, H. Kato, H. Shinohara, T. Akasaka, K. Kato, S. Aoyagi, S. Kimura, M. Takata, *Appl. Phys. Lett.* **84**, 2154 (2004).
- [96] P. A. Heiney, J. E. Fischer, A. R. McGhie, W. J. Romanow, A. M. Denenstein, J. P. Mc-Cauley Jr., A. B. Smith, D. E. Cox, *Phys. Rev. Lett.* **66**, 2911 (1991).
- [97] R. Tycko, G. Dabbagh, R. M. Fleming, R. C. Haddon, A. V. Makhija, S. M. Zahurak, *Phys. Rev. Lett.* **67**, 1886 (1991).
- [98] W. I. F. David, R. M. Ibberson, T. J. S. Dennis, J. P. Hare, K. Prassides, *Europhys. Lett.* **18**, 219 (1992).
- [99] R. C. Haddon, *Acc. Chem. Res.* **25**, 127 (1992).
- [100] C. A. Reed, R. D. Bolskar, *Chem. Rev.* **100**, 1075 (2000).
- [101] R. W. Lof, M. A. van Veenendaal, B. Koopmans, H. T. Jonkman, G. A. Sawatzky, *Phys. Rev. Lett.* **68**, 3924 (1992).
- [102] R. Hesper, *The influence of surfaces and interfaces on the properties of C₆₀ compounds*, PhD thesis, University of Groningen (2000).
- [103] M. S. Dresselhaus, G. Dresselhaus, P. C. Ecklund, *Science of Fullerenes and Carbon Nanotubes*, Academic Press, San Diego (1996).
- [104] M. P. Gelfand, *Superconductivity Review* **1**, 103 (1994).
- [105] W. A. MacFarlane, *Studies of the Metallic Alkali Fullerenes*, PhD thesis, University of British Columbia (1997).
- [106] L. Echegoyen, L. Echegoyen, *Acc. Chem. Res.* **31**, 593 (1998).
- [107] A. J. Bard, L. R. Faulkner, *Electrochemical methods: fundamentals and applications*, John Wiley & Sons, New York; Weinheim (2001).
- [108] N. Sato, Y. Saito, H. Shinohara, *Chem. Phys.* **162**, 433 (1992).
- [109] C. J. Brabec, N. S. Sariciftci, J. C. Hummelen, *Adv. Funct. Mater.* **11**, 15 (2001).
- [110] R. C. Haddon, A. S. Perel, R. C. Morris, T. T. M. Palstra, A. F. Hebard, R. M. Fleming, *Appl. Phys. Lett.* **67**, 121 (1995)

- [111] S. Kobayashi, T. Takenobu, S. Mori, A. Fujiwara, Y. Iwasa, *Appl. Phys. Lett.* **82**, 4581 (2003).
- [112] W. Kratschmer, L. D. Lamb, K. Fostiropoulos, D. R. Huffman, *Nature* **347**, 354 (1990).
- [113] Z. Bao, A. J. Lovinger, J. Brown, *J. Am. Chem. Soc.* **120**, 207 (1998).
- [114] D. Schlettwein, K. Hesse, N. E. Gruhn, P. A. Lee, K. W. Nebesny, N. R. Armstrong, *J. Phys. Chem. B* **105**, 4791 (2001).
- [115] S. Hiller, D. Schlettwein, N. R. Armstrong, D. Wöhrle, *J. Mater. Chem.* **8**, 945 (1998).
- [116] J. G. Laquindanum, H. E. Katz, A. Dodabalapur, A. J. Lovinger, *J. Am. Chem. Soc.* **118**, 11331 (1996).
- [117] S. F. Nelsen, *J. Am. Chem. Soc.* **89**, 5925 (1967).
- [118] L. Born, G. Heywang, *Z. Krist.* **190**, 147 (1990).
- [119] G. Saito, S. Hirate, K. Nishimura, H. Yamochi, *J. Mater. Chem.* **11**, 723 (2001).
- [120] J. Simon, J. J. André, *Molecular Semiconductors*, Springer, Berlin (1985).
- [121] T. Kitagawa, Y. Lee, K. Takeuchi, *Chem. Comm.* **16**, 1529 (1999).
- [122] M. S. Chan, J. R. Bolton, *Solar Energy*, **24**, 561 (1980).
- [123] S. Yamamoto, T. Sakurai, L. Yingjin, Y. Sueishi, *Phys. Chem. Chem. Phys.* **1**, 833 (1999).
- [124] N. Karl, K. H. Kraft, J. Marktanner, M. Münch, F. Schatz, R. Stehle, H. M. Uhde, *J. Vac. Sci. Technol. A* **17**, 2318 (1999).
- [125] NIST Mass Spec Data Center, "Mass Spectra" in NIST Chemistry WebBook, NIST Standard Reference Database Number 69, P. J. Linstrom and W. G. Mallard (Eds.) (2003), National Institute of Standards and Technology, Gaithersburg, MD, 20899 (<http://webbook.nist.gov>).
- [126] R. K. Yoo, B. Ruscic, J. Berkowitz, *J. Chem. Phys.* **96**, 911 (1992).
- [127] D. R. Luffer, K. H. Schramm, *Rapid Commun. Mass Spectrom.* **4**, 552 (1990).
- [128] G. Horowitz, M. E. Hajlaoui, *Adv. Mater.* **12**, 1046 (2000).
- [129] G. Horowitz, M. E. Hajlaoui, R. Hajlaoui, *J. Appl. Phys.* **87**, 4456 (2000).
- [130] R. Tecklenburg, G. Paasch, S. Scheinert, *Adv. Mater. Opt. Electron.* **8**, 285 (1998).
- [131] G. Horowitz, R. Hajlaoui, H. Bouchriha, R. Bourguiga, M. Hajlaoui, *Adv. Mater.* **10**, 923 (1998).
- [132] H. E. Katz, Z. Bao, *J. Phys. Chem. B* **104**, 671 (2000).

- [133] J. S. Chappell, A. N. Bloch, W. A. Bryden, M. Maxfield, T. O. Poehler, D. O. Cowan, *J. Am. Chem. Soc.* **103**, 2442 (1981).
- [134] J. P. Farges, A. Brau, P. Dupuis, *Solid State Commun.* **54**, 531 (1985).
- [135] W. Pukacki, M. Pawlak, A. Graja, M. Lequan, R. M. Lequan, *Inorg. Chem.* **26**, 1328 (1987).
- [136] D. V. Konarev, V. N. Semkin, A. Graja, R. N. Lyubovskaya, *J. Mol. Struct.* **450**, 11 (1998).
- [137] T. Pichler, R. Winkler, H. Kuzmany, *Phys. Rev. B* **49**, 15879 (1994).
- [138] S. Serizawa, I. Gabrielova, T. Fujimoto, T. Shido, M. Ichikawa, *Chem. Commun.* 799 (1994).
- [139] H. Zollinger, *Color Chemistry*, 2nd revised edition, VCH, Weinheim (1991).
- [140] A. M. Bouwer, R. J. Wilbrandt, *Phys. Chem.* **100**, 9678 (1996).
- [141] L. R. Melby, R. J. Harder, W. R. Hertler, *J. Am. Chem. Soc.* **84**, 3374 (1962).
- [142] S. Matsuzaki, R. Kuwata, K. Toyoda, *Solid State Comm.* **33**, 403 (1980).
- [143] S. E. Shaheen, C. J. Brabec, N. S. Sariciftci, F. Padinger, T. Fromherz, J. C. Hummelen, *Appl. Phys. Lett.* **78**, 841 (2001).
- [144] K. M. Kadish, R. S. Ruoff, *Fullerenes: Chemistry, Physics, and Technology*, Wiley-Interscience, New York; Weinheim (2000).
- [145] T. Watanabe, T. Takizawa, K. Honda, *J. Phys. Chem.* **81**, 1845 (1977).
- [146] H. Weininger, J. Schmidt, A. Penzkofer, *Chem. Phys.* **130**, 379 (1989).
- [147] E. S. Lewis, J. M. Perry, R. H. Grinstead, *J. Am. Chem. Soc.* **92**, 899 (1970).
- [148] Y. M. A. Naguib, S. G. Cohen, C. Steel, *J. Am. Chem. Soc.* **108**, 128 (1986).
- [149] S. Yamamoto, T. Sakurai, Y. J. Liu, Y. Sueishi, *Phys. Chem. Chem. Phys.* **1**, 833 (1999).
- [150] S. A. Donald, R. H. Walter, *J. Am. Chem. Soc.* **84**, 3370 (1962).
- [151] D. V. Konarev, A. Yu. Kovalevsky, A. L. Litvinov, N. V. Drichko, B. P. Tarasov, P. Coppens, R. N. Lyubovskaya, *J. Solid State Chem.* **168**, 474 (2002).
- [152] X. Wei, Z. Suo, G. Yin, Z. Xu, *Fullerene Sci. Technol.* **7**, 781 (1999).
- [153] J. Stinchcombe, A. Pénicaud, P. Bhyrappa, P. D. W. Boyd, C. A. Reed, *J. Am. Chem. Soc.* **115**, 5212 (1993).
- [154] P. Giannozzi, W. Andreoni, *Phys. Rev. Lett.* **76**, 4915 (1996).
- [155] V. N. Semkin, N. G. Spitsina, S. Krol, A. Graja, *Chem. Phys. Lett.* **256**, 616 (1996).

- [156] T. Kitagawa, Y. Lee, K. Takeuchi, *Chem. Commun.* 1529 (1999).
- [157] A. C. Bhasikuttan, L. V. Shastri, A. V. Sapre, *J. Photochem. Photobiol. A: Chem.* **143**, 17 (2001).
- [158] G. Cardini, R. Bini, P. R. Salvi, V. Schettino, M. L. Klein, R. M. Strongin, L. Brard, A. B. Smith, III, *J. Phys. Chem.* **98**, 9966 (1994).
- [159] M. C. Martin, X. Du, J. Kwon, L. Mihaly, *Phys. Rev. B* **50**, 173 (1994).
- [160] K. A. Wang, A. M. Rao, P. C. Eklund, *Phys. Rev. B* **48**, 11375 (1993).
- [161] W. Z. Wang, A. R. Bishop, L. Yu, *Phys. Rev. B* **50**, 5016 (1994).
- [162] R. Bini, J. Ebenhoch, M. Fanti, P. W. Fowler, S. Leach, G. Orlandi, C. Ruchardt, J. P. B. Sandall, F. Zerbetto, *Chem. Phys.* **232**, 75 (1998).
- [163] R. V. Bensasson, T. J. Hill, E. J. Land, S. Leach, D. J. McGarvey, T. G. Truscott, J. Ebenhoch, M. Gerst, C. Ruechardt, *Chem. Phys.* **215**, 111 (1997).
- [164] M. I. Attalla, A. M. Vassallo, B. N. Tattam, J. V. Hanna, *J. Phys. Chem.* **97**, 6329 (1993).
- [165] D. V. Schur, B. P. Tarasov, Y. M. Shul'ga, S. Yu. Zaginaichenko, Z. A. Matysina, A. P. Pomytkin, *Carbon* **41**, 1331 (2003).
- [166] P. Boulas, F. D'Souza, C. C. Henderson, P. A. Cahill, M. T. Jones, K. M. Kadish, *J. Phys. Chem.* **97**, 13435 (1993).
- [167] H. Moriyamaa, M. Abea, S. Hanazatoa, H. Motokia, T. Watanabeb, H. Kobayashic, *Synth. Met.* **103**, 2374 (1999).
- [168] T. Kitagawa, K. Takeuchi, *Bull. Chem. Soc. Jpn.* **74**, 785 (2001).
- [169] K. Hoshimono, S. Fujimori, S. Fujita, S. Fujita, *Jpn. J. Appl. Phys.* **32**, L1070 (1993).
- [170] N. Hayashi, Results obtained as part of his work in Institut für Angewandte Photophysik, Technische Universität Dresden from September to November in 2003.
- [171] J. L. Dunn, M. R. Eccles, Y. Liu, C. A. Bates, *Phys. Rev. B* **65**, 115107-1 (2002).
- [172] V. E. Kampar, I. Ya, R. B. Gudele, S. P. Kampare, S. P. Valtere, S. P. Neiland, O. Ya. Stepen, *Zh. Obshei Khimii* **51**, 2353 (1981).
- [173] L. Fomina, A. Reyes, S. Fomina, *Inter. J. Quan. Chem.* **89**, 477 (2002).
- [174] D. V. Konarev, R. N. Lyubovskaya, N. V. Drichko, E. I. Yudanova, Y. M. Shulga, A. L. Litvinov, V. N. Semkinb, B. P. Tarasov, *J. Mater. Chem.* **10**, 803 (2000).

List of symbols and abbreviations

Alq ₃	tris (8-hydroxy-quinolinato)-aluminium
AO	acridine orange
AOB	acridine orange base
BEDT-TTF	bis (ethylenedithio)-tetrathiafulvalene
C ₆₀	buckminster fullerene
C _i	the capacitance per unit area
CV	Crystal violet
DDQ	2,3-dichloro-5,6-dicyano-p-benzoquinone
DMSO	dimethyl sulfoxide
DOS	density of states
<i>E</i>	applied electric field
EA	electron affinity
EA _{M,M}	solid state electron affinity of the matrix molecule
<i>E_C</i>	the conduction band edge
<i>E_D</i>	level of the dopant or trap
<i>E_F</i>	Fermi level
EI MS	electron impact mass spectroscopy
ESI MS	Electrospray ionization mass spectroscopy
ESR	electron spin resonance spectroscopy
<i>E_V</i>	valence band edge
ΔE	energetic difference between the initial and final state
F ₄ -TCNQ	tetrafluoro-tetracyanochinodimethan
F ₁₆ ZnPc	Perfluorinated 1,2,3,4,8,9,10,11,15,16,17,18,22,23,24,25-hexadecafluorophthalocyaninatozinc(II)
Fc/Fc+	ferrocene/ferrocenium
FET	field effect transistor
FTIR	Fourier transform infrared
<i>g_m</i>	transconductance
HOMO	highest occupied molecular orbital
<i>I_D</i>	drain current
IP	ionization potential
IP _{D,M}	ionization potential of the donor in the matrix M
IR	infrared
<i>j</i>	current density
<i>k_B</i>	Boltzmann constant
LCV	leuco crystal violet
LESR	light induced ESR spectroscopy
LMG	leuco malachite green
LUMO	lowest unoccupied molecular orbital
MePTCDI	N,N'-dimethyl-perylene-3,4,9,10-tetracarboxylic diimide
MG	malachite green

MS	mass spectroscopy
MW	molecular weight
μ	field effect mobility
n_e	electron density
$\langle \nu \rangle$	electric field-induced directional velocity component
NHE	normal hydrogen electrode
NMR	Nuclear magnetic resonance spectroscopy
NTCDA	1,4,5,8-naphthalene-tetracarboxylic-dianhydride
Π	Peltier coefficient
OFETs	organic field effect transistors
OLEDs	organic light-emitting devices
S	Seebeck coefficient
SCE	saturated calomel electrode
SCLC	space-charge-limited-current
σ	conductivity
TCNQ	7,7,8,8-tetracyanoquinodimethane
TCNQH ₂	p-phenylenedimalononitrile
TFTs	thin-film transistors
TMS	tetramethylsilane
TOF	time-of-flight
UV/VIS/NIR	ultra violet/visible/near infrared
V_D	drain voltage
V_G	gate voltage
V_T	threshold voltage

Acknowledgements

This thesis contains the contribution of a large number of individuals.

Firstly, I would like to thank Prof. Karl Leo for his supervision of this interesting and challenging work and for all his help and encouragement. It is he who provided me with the opportunity to come to the Institut für Angewandte Photophysik and carry out research in the field of organic electronics. It is he who has created a comfortable, free and open scientific atmosphere in which I gained a lot of new knowledge, in particular in physics. Due to his effort, I could perform my research without any financial limitation. I also appreciate very much his quick and competent reading and correction of the manuscript.

I am especially grateful to Dr. Ansgar Werner and Dr. Martin Pfeiffer.

Dr. Ansgar Werner gave me countless support and help, from the first day I came to Germany to the last days on the correction of this thesis. He kindly and patiently taught me a lot of experimental techniques in the B30 and UFO1 tools. When I encountered trouble in my work, whether in science or in technology, he always gave me selfless help. His wonderful ideas could often enlighten me to overcome those difficulties and find better ways.

As a group leader, Dr. Martin Pfeiffer gave me a lot of encouragement and guidance. He corrected the manuscript very carefully and contributed many great ideas to improve it. His advice and comments are always of vital importance to my work in the past three years. Thanks to his contribution, the free and stimulating research atmosphere in the organic optoelectronics group ensures that all the research activities are smoothly running and that all are happy.

It is Dr. Ansgar Werner and Dr. Martin Pfeiffer's deep understanding and mastering of doping that made my PhD work go on at the right direction all the time. It is both of them who opened the door for me to the organic semiconductor world. With the help of them, I found my research interesting and broadened my career field. They taught me a lot in terms of physics, in particular physics of semiconductors, but also writing and presentation skills.

I am also indebted to the following people for their support and assistance in developing this thesis. My thanks go to:

Kentaro Harada for a lot of help in many respects. He taught me how to measure field effect mobility.

Dr. Xianjie Liu (IFW, Dresden) for the measurements of many FTIR and Raman spectra and suggestions.

Dr. Naoki Hayashi (Department of Chemistry, Graduate School of Science, Nagoya University, Japan) for his contribution of the data of Seebeck study.

Dang Xuan Dung (Institut für Physikalische Chemie und Elektrochemie, TU Dresden) for the electrochemical measurements of some materials.

Dr. Yuzhou Wang (Institut für Organische Chemie, TU Dresden) for helpful discussion in organic chemistry.

Larysa Shapoval (Institut für Analytische Chemie, TU Dresden) for mass spectroscopy.

Maik Koch for the purification of materials and help in equipments.

Christian Uhrich for his design of computer-controlled measurements of field effect mobility.

Christian Kolberg for his support in technology for B30 and UFO1.

Dr. Gufeng He for help with the computer.

Dr. Youxuan Zheng for the measurements of cyclic voltammograms.

Dr. Bert Maennig and Jens Drechsel who taught me the conductivity measurements in UFO1.

I thank Dr. Jingsong Huang for his help, encouragement and friendship during my first days in Dresden.

I also express my gratitude to Qiang Huang, Dr. Xiang Zhou, Dr. Wenge Guo, Dr. Dashan Qin, Dr. Jan Blochwitz-Nimoth, Fryderyk Kozlowski, Robert Gehlhaar, Annette Petrich, Dr. Andreas Schwab and Eva Schmidt for good cooperation, friendship and help in many respects.

Again, my thanks to all of you and anybody I missed who deserves to be mentioned here!

Diese Arbeit wurde unter der Betreuung von Prof. Dr. Karl Leo am *Institut für Angewandte Physik (IAP)*, Teilinstitut **IAPP** des *Technische Universität Dresden (TU Dresden)* angefertigt.

Versicherung

Hiermit versichere ich, dass ich die vorliegende Arbeit ohne die unzulässige Hilfe Dritter und ohne Benutzung anderer als der angegebenen Hilfsmittel angefertigt habe; die aus fremden Quellen direkt oder indirekt übernommenen Gedanken sind als solche kenntlich gemacht. Die Arbeit wurde bisher weder im Inland noch im Ausland in gleicher oder ähnlicher Form einer anderen Prüfungsbehörde vorgelegt.

Dresden, 2005

Fenghong Li